Improvements in Fabrication and Materials for Solid Oxide Fuel Cells

by

Mohammad Taghi Amiri

A thesis submitted in partial fulfillment of the requirements for the degree of

Doctor of Philosophy

in

Materials Engineering

Department of Chemical and Materials Engineering

University of Alberta

Abstract

Solid oxide fuel cells have numerous advantages, including higher efficiencies, fuel diversity, and lack of need for expensive catalysts compared to other fuel cells. Yet the lower performance and lack of durability in the long term still hinder its practical usage. By lowering the operating temperature, the system's longevity can increase dramatically. The downside is that maintaining the acceptable performance requires either the development of new materials for cell components or improving the structural and functional characteristics of electrodes. This study pursues both approaches.

First, a new proton conductor electrolyte based on $Ba_{0.5}Sr_{0.5}Ce_{0.6}Zr_{0.2}Gd_{0.1}Y_{0.1}O_{3-\delta}$ has been used in a SOFC. Compared to other studies, higher power output was achieved. The chemical compatibility in moisture and carbon dioxide was also studied in detail.

Second, the combination of microwave irradiation in conjunction with salt infiltration was used for rapid catalyst synthesis inside the porous YSZ layer. Compared to the traditional sintering method with an electric resistance furnace, this approach increased the cell's performance. It was concluded the enhancement of this technique came from the enhanced morphology of the resulting particles.

Next, using direct microwave heating on a cermet support to enable direct microwave sintering without the use of any susceptor was conducted. This method was used on poor microwaved coupled materials, which would be extremely difficult and expensive

to sinter using traditional methods. This study shows the successful integration of this method for YSZ.

The chemical compatibility of components was investigated by powder X-ray diffraction and Rietveld refinement. Electrochemical examinations under air/hydrogen were conducted. Specifically, electrochemical impedance spectroscopy was used to examine the electrochemical performance of the full cell at different temperatures in this study. Detailed analysis was done to deconvolute the impedance results, including Distribution of Relaxation Times. Microstructures of the prepared cells were studied using a field-emission scanning electron microscope.

A similar setup to a solid oxide fuel cell was used to convert titanium dioxide to nitride electrochemically. Titanium nitride offers excellent properties such as high electrical conductivity and corrosion resistance up to 800 °C. TiN might address several key disadvantages of fuel cells, such as using direct hydrocarbon fuels and long-term electrode grain growth. We successfully converted a titanium dioxide support to titanium nitride in the presence of ammonia. This method offers a much cheaper sintering process, and the same cell can later be used as a fuel cell or electrolyzer.

Finally, an enhanced method for electrode deposition into a porous layer was developed. This method exerts an external electric field, forcing the infiltration precursor into the porous matrix and depositing the catalyst. The advantage of this method is it can be used for a thick layer. Another advantage is that it can deposit a higher amount of catalyst than conventional infiltration. The electrochemical performance improved despite this method needing further optimization.

Preface

This thesis is an original work by Taghi Amiri.

Chapter 2 of this thesis has been published as Taghi Amiri, Kalpana Singh, Navjot Kaur Sandhu, Amir Reza Hanifi, Thomas H Etsell, Jing-Li Luo, Venkataraman Thangadurai, Partha Sarkar, "High Performance Tubular Solid Oxide Fuel Cell based on $Ba_{0.5}Sr_{0.5}Ce_{0.6}Zr_{0.2}Gd_{0.1}Y_{0.1}O_{3-\delta}$ Proton Conducting Electrolyte", Journal of The Electrochemical Society, 165 (10), F764-F769, 2018. Taghi Amiri fabricated samples, conducted the experiments and measurements, analyzed the data, and participated in writing the manuscript. Kalpana Singh synthesized the electrolyte and conducted a portion of the experiments and characterizations. Navjot Kaur Sandhu and Amir Reza Hanifi carried out some of the fabrications. Thomas H Etsell, Jing-Li Luo, Venkataraman Thangadurai, and Partha Sarkar guided the research design, participated in the discussions, and reviewed and edited the manuscript.

Chapter 3 of this thesis has been published as Taghi Amiri, Thomas H Etsell, Partha Sarkar, " Using Microwave Irradiation for In-situ Infiltration of Electrodes in Solid Oxide Fuel Cells", Materials Technology. Taghi Amiri fabricated the samples, conducted the experiments and measurements, analyzed the data, and participated in writing the manuscript. Thomas H Etsell and Partha Sarkar guided the research design, participated in the discussions, and reviewed and edited the manuscript.

Chapter 4 of this thesis is accepted for publication as Taghi Amiri, Thomas H Etsell, Partha Sarkar, "Direct Microwave Sintering of Poorly Coupled Ceramics in

Electrochemical Devices", Journal of Electrochemical Science and Technology. Taghi Amiri fabricated the samples, conducted the experiments and measurements, analyzed the data, and participated in writing the manuscript. Thomas H Etsell and Partha Sarkar guided the research design, participated in the discussions, and reviewed and edited the manuscript.

Chapter 5 of this thesis is a paper in preparation for publication. Taghi Amiri fabricated the samples, conducted the experiments and measurements, analyzed the data, and participated in writing the manuscript. Thomas H Etsell and Partha Sarkar guided the research design, participated in the discussions, and reviewed and edited the manuscript.

Chapter 6 of this thesis is a paper in preparation for publication. Taghi Amiri fabricated the samples, conducted the experiments and measurements, analyzed the data, and participated in writing the manuscript. Thomas H Etsell and Partha Sarkar guided the research design, participated in the discussions, and reviewed and edited the manuscript.

Dedicated to My Beloved Family

Acknowledgments

I have been privileged to study at the University of Alberta. First, I would like to thank my supervisor, **Prof. Thomas H. Etsell**, for providing me with this opportunity. I want to express my utmost gratitude for his guidance, unconditional support, knowledge, and invaluable supervision throughout my studies. It has been my absolute honor and pleasure working under his supervision.

I want to express my sincere gratitude to **Prof. Jingli Luo** and **Prof. Hyun-Joong Chung** for thier supervision, influence in shaping my experimental methods, and critiquing my results.

I would be remiss not to mention **Dr. Partha Sarkar** for his kind support, insightful feedback, and suggestions during this study; they were a great help and impacted and inspired me during my research. I would also like to express my deep appreciation to **Dr. Amirreza Hanifi** for his kind mentorship, guidance, and instructive comments on my research.

I would also like to thank **Dr. Mirjavad Geramian** for his kind and insightful advice on improving this study and his generous support. I want to thank **Dr. Mehdi Alipour** and **Dr. Mark Cuglietta for** generously providing knowledge and expertise.

My gratitude also goes to all my friends for the support they offered me while pursuing this research. I would like particularly to thank **Dr. Mohammad Khalkhali**, **Dr. Hamid Niazi**, **Reza Khalkhali**, and **Dr. Mohsen Mohammadijoo**.

Thanks should also go to the technical staff of the Department of Chemical and Materials Engineering for all their assistance (in alphabetical order by the first name): Amy Chow, Kevin Heidebrecht, Lily Laser, Marion Pritchard (RIP), Mia Law, Nathan Gerein, and Walter Boddez.

I would like to acknowledge the financial support from Future Energy Systems at the University of Alberta, Natural Sciences and Engineering Research Council (NSERC), and Climate Change and Emissions Management Corporation (CCEMC).

Last but not least, I would like to express my immense gratitude to my parents for all their boundless love, sacrifices, and unconditional support. Their encouragement and dedication to my cause have been unfailing and way beyond the call of parental duty. I am deeply indebted to **Dr. Saeid Amiri** for his kind support, encouragement, and insightful pieces of advice throughout my life. And for my wife, **Dr. Maryam Abbasi**, who has stood by me through my struggles, absences, and impatience, thank you for all your support and continuous and unparalleled love; you have been amazing.

Taghi Amiri

Table of Contents

List of Tables

List of Figures

List of Abbreviations

EIS	Electrochemical Impedance Spectroscopy
GDC	Gadolinium-doped Ceria
HOR	Hydrogen Oxidation Reaction
LSM	Strontium-doped Lanthanum Manganite
OCV	Open Circuit Voltage
ORR	Oxygen Reduction Reaction
PEM	Proton Exchange Membrane
SDC	Samarium-doped Ceria
SEM	Scanning Electron Microscope
SOFC	Solid Oxide Fuel Cell
TPB	Triple Phase Boundary
TPL	Thin Porous Layer
XRD	X-ray Diffraction
YSZ	Yttria-stabilized Zirconia

Chapter 1. Introduction

1.1 Research background

1.1.1 Introduction

A fuel cell is an energy conversion device that produces electricity by electrochemically combining fuel and oxidant across an ionically conducting electrolyte. A dense electrolyte is sandwiched between two porous electrodes. In a positive species conductor electrolyte, fuel is fed to the anode, undergoes an oxidation reaction, and releases electrons to the external circuit. The oxidant is provided to the cathode, accepts electrons from the external circuit, and undergoes a reduction reaction. The electron flow in the external circuit from the anode to the cathode produces direct current electricity.

Advantages of fuel cells over traditional power generation include high energy conversion efficiency associated with direct conversion of chemical energy to electrical energy, environmentally friendly since they emit negligible amounts of pollutants, modularity, portability, and quiet, vibration-free operation [2]. Hydrogen is being referred to as the ideal fuel for fuel cell systems despite significant obstacles regarding its generation, storage and current infrastructure [1]. Classification of fuel cells is based on their electrolyte types. The operational characteristics of these fuel cells are summarized in Table 1-1.

.

Table 1-1 Operational characteristics of various fuel cells[5].

Type	Electrolyte	Operating Temp.	Fuel	Oxidant	Efficiency
Alkaline (AFC)	potassium hydroxide (KOH)	50–200°C	pure hydrogen or hydrazine	O_2/Air	50–55%
Phosphoric acid (PAFC)	phosphoric acid	160–210°C	hydrogen from hydrocarbons and alcohol	O_2/Air	40–50%
Sulfuric acid (SAFC)	sulfuric acid	80–90°C	alcohol or impure hydrogen	O_2/Air	40–50%
Proton-exchange membrane (PEM)	polymer, proton exchange membrane	50–80°C	less pure hydrogen from hydrocarbons or methanol	O_2/Air	40–50%
Molten carbonate (MCFC)	molten salt such as nitrate, sulfate, carbonates	630–650°C	hydrogen, carbon monoxide, natural gas, propane, marine diesel	CO_2/O_2/Air	50–60%
Solid oxide (SOFC)	ceramic as stabilized zirconia and doped perovskite	600–1000°C	natural gas or propane	O_2/Air	45–60%

Protonic ceramic (PCFC)	thin membrane of barium cerium oxide	600–700°C	hydrocarbons	O_2/Air	45–60%

Despite the discovery of fuel cells more than 160 years ago and their high efficiencies and environmental advantages, only in recent years have fuel cells been approaching commercial success [4]. During the past few years, tremendous attempts have been made to develop and improve fuel cell technology.

Among the different types of fuel cells, the solid oxide fuel cell (SOFC) is the one that can utilize a wide variety of fuels beside hydrogen, including hydrocarbons, due to the high working temperature [6]. Comparing existing hydrocarbon infrastructure to hydrogen gives the SOFC a significant advantage over other fuel cells. As SOFCs operate at high temperatures (600-1000°C), the high quality heat generated can be used in different ways, such as running a gas turbine or an endothermic internal fuel reformer[4]. Although the commercial life expectancy of SOFCs is 10–20 years, two to four times longer than other fuel cells, complications including material degradation, impurities, and carbon formation during hydrocarbon fuel usage hinder their reliability dramatically [2, 3]. Commercialization of these efficient devices is still suffering from high costs (material and fabrication) and limited lifetime [4]. Table 1-2 compares the cost of the PEM and SOFC, the two most prominent fuel cell systems, at different power outputs and manufacturing numbers.

Table 1-2 System Cost Comparision Between PEM and SOFC [5]

PEM System Cost

Description	100 kW 1,000 Units/year	100 kW 10,000 Units/Year	250 kW 1,000 Units/year	250 kW 10,000 Units/Year
Total stack manufacturing, testing & conditioning costs	$34,480	$23,303	$71,151	$53,494
Fuel, Water, and Air Supply Components	$22,857	$20,894	$28,186	$25,744
Fuel processor components	$48,005	$43,629	$58,304	$53,895
Heat recovery components	$33,994	$30,868	$51,218	$46,680
Power Electronic, Control, and Instrumentation Components	$43,221	$35,258	$94,238	$74,725
Assembly Components and Additional Work Estimate	$26,790	$24,080	$36,955	$33,300
Total system cost, pre-markup	$209,348	$178,032	$340,052	$287,838
System cost per kwnet, pre-markup	$2,093	$1,780	$1,360.21	$1,151.35
Sales markup	$1	$1	50.00%	50.00%
Total system cost, with markup	$314,021	$267,048	$510,077	$431,758
System cost per kwnet, with markup	$3,140	$2,670	$2,040	$1,727

SOFC System Cost

Description	100 kW 1,000 Units/year	100 kW 10,000 Units/Year	250 kW 1,000 Units/Year	250 kW 10,000 Units/Year
Total stack manufacturing, testing & conditioning costs	$32,005	$28,537	$73,566	$70,452
Fuel and Air Supply Components	$6,995	$6,293	$12,439	$11,391
Fuel processor components	$5,675	$5,114	$9,255	$8,377
Heat recovery components	$19,698	$18,430	$31,718	$29,718
Power Electronic, Control, and Instrumentation Components	$43,627	$35,622	$95,050	$75,453
Assembly Components and Additional Work Estimate	$9,975	$8,950	$16,935	$15,240
Total system cost, pre-markup	$117,976	$102,946	$238,963	$210,630
System cost per kw_{net}, pre-markup	$1,179.76	$1,029.46	$955.85	$842.52
Sales markup	50.00%	50.00%	50.00%	50.00%
Total system cost, with markup	$176,964	$154,418	$358,445	$315,945
System cost per kw_{net}, with markup	$1,770	$1,544	$1,434	$1,264

The critical challenge in accelerating the commercialization of SOFC technology is to develop robust materials and new fabrication methods that allow higher performance and improved durability at a lower cost [6].

This study aims to address some of the mentioned shortcomings. First, we focused on an enhanced proton-conducting electrolyte that can withstand hydrocarbons with excellent power performance. Then we focused on an in-situ method of catalyst deposition inside a porous layer as the electrode using microwave irradiation. Finally, a new way to directly microwave sinter a poorly-coupled electrolyte is developed to reduce processing time and cost significantly.

In this chapter, concepts and recent developments related to this research are highlighted. The research objectives and the experimental methods are specified. Lastly, the research outline is presented.

1.1.2 Solid oxide fuel cells

A solid oxide fuel cell (SOFC) is a solid-state electrochemical device that converts the chemical energy stored in the fuel directly into electrical energy resulting in high efficiency, which, along with low environmental impact, quiet operation and low maintenance, makes SOFCs highly suitable for stationary power generation applications [7]. In a SOFC stack, single cells are connected in an electrical series via an interconnect component to provide the desired power level.

SOFC uses an ionically conducting ceramic as its electrolyte. Two major types of ionic conductivity are used in this fuel cell: oxygen ion and proton conductor. Figure 1-1 shows a schematic design of both oxygen and proton conducting SOFCs.

Traditional SOFCs em Ni-YSZ ploy a Ni-YSZ cermet, oxide-ion conducting YSZ, and lanthanum strontium manganite as the anode, electrolyte and cathode, respectively [8]. To reduce the overpotentials associated with these materials, the cell needs to run at elevated temperatures near 1000 °C [9]. This high temperature negatively affects the choice of available materials, mainly for interconnects and sealants, and their long-term stability [10].

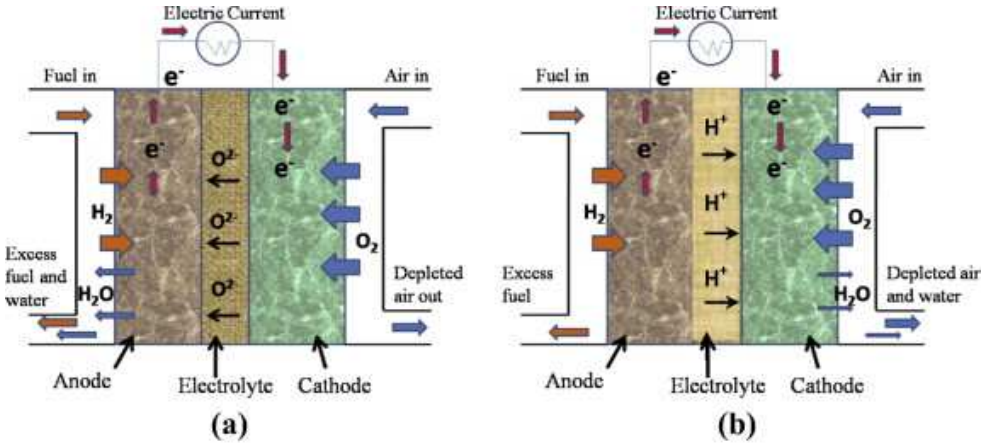

Figure 1-1 Schematic diagram of solid oxide fuel cells with (a) oxide-ion conducting electrolyte, and (b) proton conducting electrolyte [1].

One solution to reduce the operating temperature of SOFCs is to use new materials for cell components that exhibit lower overpotential. Oxygen ion conductor electrolytes such as $La_{0.9}Sr_{0.1}Ga_{0.8}Mg_{0.2}O_{3-\delta}$, $Ce_{0.8}Gd_{0.2}O_{2-\delta}$, and $Ce_{0.8}Sm_{0.2}O_{1.9}$, and mixed ionic and electronic conductors $Ba_{0.5}Sr_{0.5}Co_{0.8}Fe_{0.2}O_{3-\delta}$, $La_{0.99}Ca_{0.01}NbO_4$, and

nickelates for cathodes are some examples. Chemical incompatibility and higher cost have resulted in limited large-scale usage [11].

1.1.2.1 Proton conducting SOFC

Unlike YSZ, which conducts oxygen ions, there has recently been a new trend in developing electrolytes that conduct protons, as shown by eq. (1-1) with Kröger-Vink notation [12].

$$H_2O(g) + V_{O(s)}^{\bullet\bullet} + O_{O(s)}^{x} \rightarrow 2OH_{O(s)}^{\bullet} \quad (1\text{-}1)$$

where $V_O^{\bullet\bullet}$ indicates an oxygen ion vacancy with two effective positive charges and $OH_O^{\bullet}$ indicates a proton attached to a regular oxygen ion site with a relative positive charge.

Proton conducting electrolytes (PCEs) have two main advantages: first, they do not dilute the fuel, which lowers the performance based on the Nernst equation [13]. Also, due to their relatively low activation energy of conduction due to the smaller size of H^+, they can achieve high conductivity at lower temperatures [14-16].

Doped perovskites as solid proton-conducting electrolytes such as barium cerate (BaCeO3), strontium cerate (SrCeO3), and barium zirconate (BaZrO3), have been widely investigated in recent years to be used in electrochemical devices such as solid oxide fuel cells [17]. Iwahara et al. first reported high proton conductivity ($\sigma \sim 10^{-2}$ S cm^{-1} at 600 °C) in perovskite-type doped-$SrCeO_3$ and $BaCeO_3$ ceramics under humid atmospheres in the early and late 1980s [18, 19]. Despite their superior

performance, cerate-based perovskites face the problem of poor chemical stability in the presence of moisture and CO_2, which is a significant hindrance for commercial realization [20, 21]. As humidity is present in every fuel cell, and CO_2 is produced when hydrocarbons are used as fuel, researchers must solve this crucial issue. Iguchi et al. deposited a 0.7-micron $BaCe_{0.8}Y_{0.2}O_3$ electrolyte on top of a 40-micron palladium substrate as anode and achieved power densities of 570 mW/cm^2 at 430 °C and 780 mW/cm^2 at 510 °C under air/hydrogen conditions[22]. The authors protected the thin electrolyte from moisture and carbon dioxide by depositing it onto a dense layer of palladium foil, a well-known hydrogen separation material.

On the other hand, zirconate-based perovskites are stable, both mechanically and chemically [23]. However, zirconate based perovskites such as $BaZrO_3$ show lower conductivity than cerate based oxides due to significant grain boundary resistance, which arises due to low sinterability making it rather challenging to sinter a leak-free zirconate PCE, usually needing temperatures exceeding 1600 °C, hampering its actual usage [17, 24, 25]. Thus researchers have worked on solid solutions between $BaCeO_3$ and $BaZrO_3$ in order to achieve good chemical stability and high proton conductivity [24, 26].

1.1.2.2 SOFC configuration and geometry

There are three common self-supported cell configurations for SOFC; anode-, cathode-, and electrolyte-supported. As electrolyte-supported cells have a high ohmic loss, they require a high temperature to operate. Cathode-supported cells, even under high

pressures, are less efficient than anode-supported cells for hydrogen fuel. That leaves the anode-supported cell as the best choice [3]. Planar and tubular designs are the two most common that have been studied, shown in Figure 1-2. Planar geometry is more compact with less ohmic and concentration losses but higher thermal gradients than tubular cells. The current path is typically longer in tubular cells, so their performance is significantly limited beyond a specific radial extension [27].

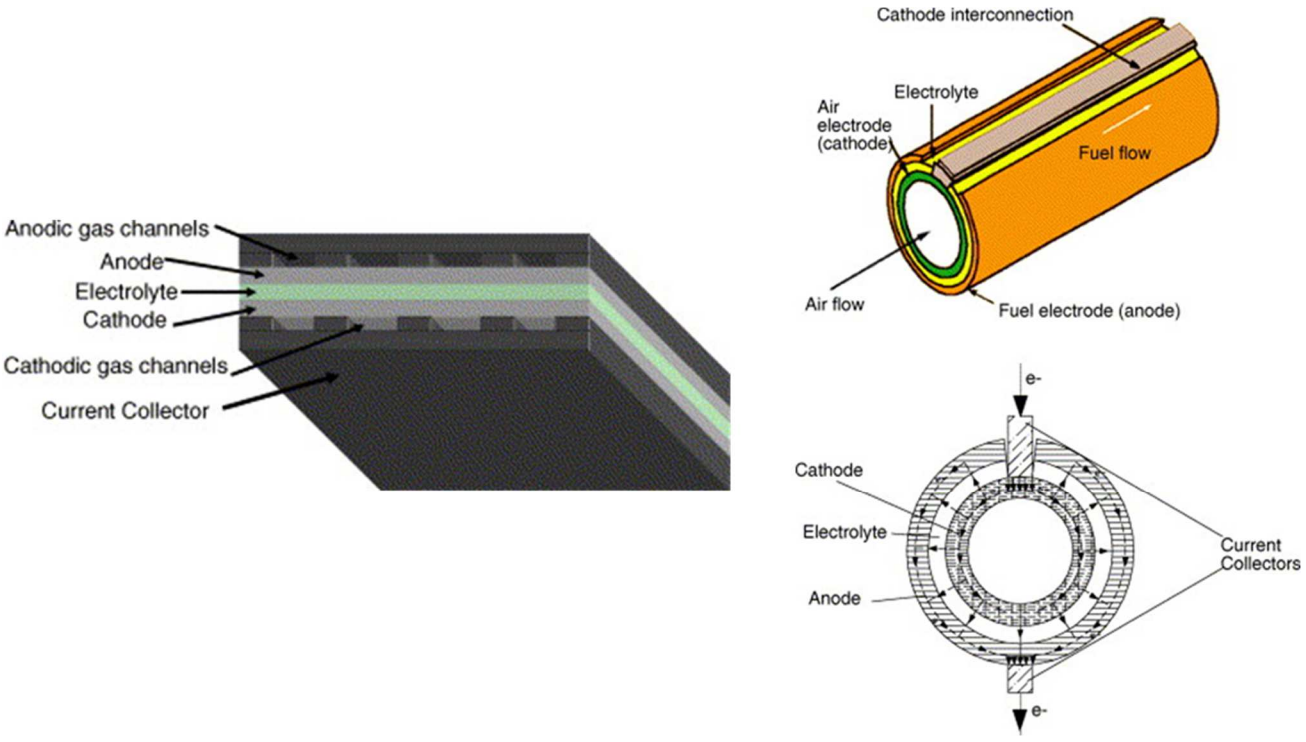

Figure 1-2 Schematic of a (left) planar SOFC (right) tubular SOFC [27]

Thus power density of tubular SOFCs is inversely related to the diameter [28]. The tubular design has two main advantages, more robust thermal shock resistance and simplified sealing [29].

1.1.3 Microwave irradiation

1.1.3.1 Introduction

Microwaves are electromagnetic waves characterized by frequencies between 300 MHz and 300 GHz with wavelengths ranging from 1 mm to 1 m, correspondingly. Due to the material–microwaves interaction, heating is fundamentally different from conventional heating since heat is generated internally, rather than being transferred from an external source via heat transfer mechanisms. Direct coupling leads to rapid volumetric heating that is difficult to produce by conventional heating[30].

1.1.3.2 Allocated frequencies

The Federal Communications Commission (FCC) has allocated 915 MHz, and 2.45, 5.85, and 20.2-21.2 GHz for industrial, scientific, and medical use because of their suitability for these purposes. Current medical and industrial usage are based on heating water, so only 915 MHz and 2.45 GHz have significant application. Also, these are the only frequencies readily available at practical power levels for the microwave processing of ceramics. A few other frequencies are available on a limited basis, i.e., 28, 60, and 140 GHz, and 500 MHz, because of their use as power sources in accelerators, plasma fusion devices, and commercial broadcasting [31].

The large dipole moment of a water molecule is what allows a microwave oven to heat food. The alternating electric field of the microwave radiation (created by a

magnetron) causes the water dipoles to rotate back and forth. This jiggling of the molecules causes them to bump into each other, which results in the thermal energy (the heat) that is observed. The specific microwave frequency used (usually about 2.5 GHz, which corresponds to a wavelength of about 12 cm) has nothing to do with the resonant vibrational frequency of a free water molecule in vapor, which is about 20 GHz. There isn't anything special about the 12 cm wavelength, although if it were much shorter, the waves wouldn't penetrate food as well [32].

1.1.3.3 Concept of permeability

The material response to an applied field is related to the dielectric and magnetic properties of that matter which is identified using ε^* and μ^*, respectively, known as complex dielectric and magnetic permittivity. ε^* describes the ability of the material to polarize (losing electric neutrality) in the presence of the applied electric field (static or dynamic) and ε can be expressed by eq. (1-2).

$$\varepsilon = \varepsilon' - j\varepsilon'' \tag{1-2}$$

It is convenient to use relative complex permittivity or dielectric constant, which expresses it relative to free space as in eq.(1-3).

$$\varepsilon_r = \varepsilon_r' - j\varepsilon_r'' \tag{1-3}$$

Relative permittivity and permittivity can be related to each other by eq.(1-4) .

$$\varepsilon = \varepsilon_r \varepsilon_\circ \tag{1-4}$$

$\varepsilon_\circ$ is the permittivity of vacuum and is equal to $8.86\times10^{-12}\ F/m$.

The real part shows the material's ability to store electric energy, while the imaginary part, also known as the loss factor, represents the ability of the material to dissipate energy from the electromagnetic field, i.e., by heat generation[33]. In addition to account for conductivity losses, the relative effective loss factor ε''_{eff} can be used and differs by the additional term $\sigma/\varepsilon_0 \cdot \omega$, where σ is the electrical conductivity (S/m), and ω is the angular frequency of the incident wave. The dielectric properties vary with frequency, temperature, chemical state, manufacturing process and purity.

The loss tangent, tan δ expressed by eq. (1-5), represents the efficiency of the material to convert absorbed energy into heat. It is used to describe the dielectric response of a material. δ is the phase difference between the oscillating electric field and the polarization of the material.

$$\tan\delta = \frac{\varepsilon''}{\varepsilon'} \tag{1-5}$$

Similarly, the response to an applied magnetic field can be described by the complex permeability μ, which is expressed by eq. (1-6).

$$\mu^* = \mu' - j\mu'' \tag{1-6}$$

The real part is the response of the material to the static magnetic field. μ'' represents the magnetic loss factor due to resonance and relaxation processes under the influence of an alternating magnetic field [34]. Relative to the empty space permeability $\mu_\circ$, which is equal to $4\pi \times 10^{-7}\, V\,s / A\,m$, permeability can be defined as:

$$\mu' = \mu_\circ \mu'_r \tag{1-7}$$

1.1.3.4 Power Generation by Microwaves

The absorbed power due to the conversion of electromagnetic energy into heat in the material is attributed to two factors: an electric loss given by eq. (1-8) and magnetic part as described by eq. (1-9) [34].

$$P_{av} = \sigma E_{rms}^2 = \omega \varepsilon_\circ \varepsilon''_{eff} E_{rms}^2 = 2\pi \varepsilon_\circ \varepsilon''_{eff} E_{rms}^2 = 2\pi f \varepsilon' \tan\delta E_{rms}^2 \tag{1-8}$$

$$P_{av} = \omega \mu_\circ \mu''_{eff} H_{rms}^2 = 2\pi \mu_\circ \mu''_{eff} H_{rms}^2 \tag{1-9}$$

E_{rms} and H_{rms} are electric and magnetic field root mean square; ε''_{eff} and μ''_{eff} are the effective relative dielectric and magnetic loss factors, respectively.

So the total dissipated power density (W/m^3) into the material is given by the total of both electric and magnetic loss as shown in eq. (1-10).

$$P_{av} = \omega \varepsilon_\circ \varepsilon''_{eff} E_{rms}^2 + \omega \mu_\circ \mu''_{eff} H_{rms}^2 \tag{1-10}$$

In the case of different materials present, the material with a higher loss factor dissipates heat more efficiently. Since loss factor can be tailored (dopant or particle size), this feature can be used as a means for selective heating.

The effective relative dielectric loss factor is the summation of losses from polarization and conduction. The dielectric polarization losses in eq. (1-11) include dipolar, electronic, atomic and interfacial polarization.

$$\begin{aligned} \varepsilon''_{eff} &= \varepsilon''_{polarization} + \varepsilon''_{conduction} = \left(\varepsilon''_{dipolar} + \varepsilon''_{electronic} + \varepsilon''_{atomic} + \varepsilon''_{\text{interfacial}}\right) + \varepsilon''_{conduction} \\ &= \left(\varepsilon''_{dipolar} + \varepsilon''_{electronic} + \varepsilon''_{atomic} + \varepsilon''_{\text{interfacial}}\right) + \frac{\sigma}{\omega \varepsilon_\circ} \end{aligned} \tag{1-11}$$

The second term of eq. (1-10) is usually negligible for most materials unless they have

relevant magnetic properties, like ferrites or metal powders. Power density dissipated in a material depends on the frequency of the microwaves, the material's loss factor, and the local value of the electric field. Thus, the nature of the material and the geometrical characteristics of the microwave applicator, i.e., where microwave–matter interaction takes place, affect the power density and hence the heat generation inside the material.

1.1.3.5 Microwave-Material Interactions

The incident electromagnetic wave may be reflected, transmitted or absorbed by materials. Magnetic materials can interact with the magnetic field component of the electromagnetic wave. The interaction of microwaves with materials can be classified as shown in Figure 1-3.

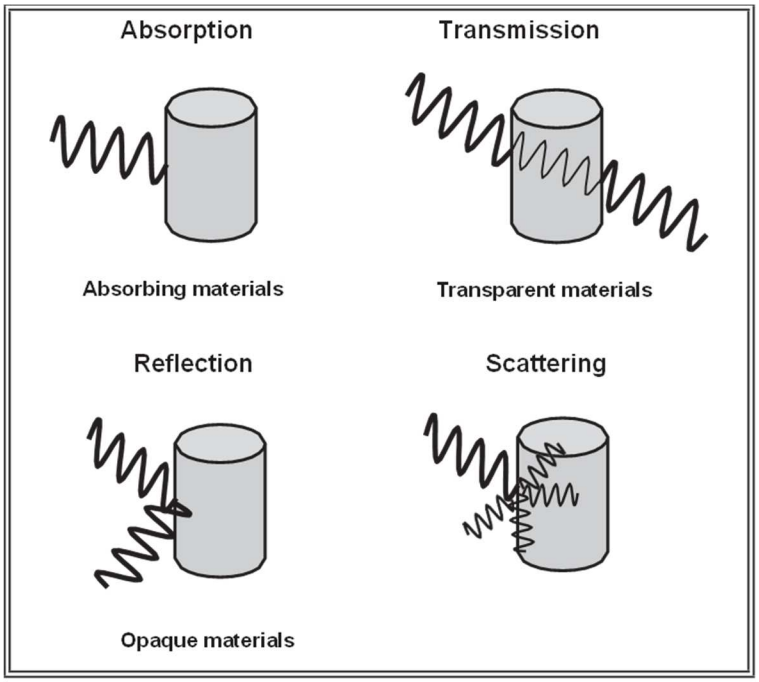

Figure 1-3 Interaction of the electromagnetic field with materials [34]

1. **Absorbing**: range from conductors to insulators with high dielectric loss, which can efficiently absorb electromagnetic energy and convert it to heat.
2. **Transparent**: materials such as ceramics, glass, and air that have a low dielectric loss. They reflect and negligibly absorb waves and allow them to pass through readily with little loss.
3. **Opaque**: such as metals with free electrons that reflect and do not allow waves to pass through.
4. **Magnetic**: such as ferrites that interact with the magnetic component of the wave and get heated.

The interaction between the microwaves' electric and magnetic field components and the materials can result in dielectric and magnetic losses, leading to heating. Dielectric losses can be attributed to the redistribution of charges or polarization under the influence of an alternating external field.

The different polarization mechanisms in dielectric materials due to interaction with the electric field are summarized in Table 1-3. The contributions by different polarization mechanisms are frequency-dependent. Electronic and ionic polarizations occur at visible and infrared frequencies and do not usually contribute to microwave heating. Microwave heating of dielectrics depends primarily on dipolar and interfacial polarization as well as conduction losses.

Table 1-3 Effect of different polarization mechanisms[34]

Polarization	Effect

Mechanism	
Electronic polarization	Displacement of valence electrons around the nuclei
Ionic polarization	Relative displacement of positive and negative ions or atoms from their equilibrium position
Dipolar polarization	Permanent dipole moments in molecules which tend to re-orientate under the influence of an alternating electric field
Interfacial polarization	Accumulation of charges at interfaces between components in heterogeneous systems

In materials with high conductivity, such as metals, heating depends on conduction losses. In magnetic materials, magnetic losses such as hysteresis, eddy currents, domain wall, and electron spin resonance contribute to the heating.

However, irrespective of the current understanding of microwave interactions with materials, no single theory can explain the different responses by materials to microwaves.

1.1.3.5.1 Electronic Polarization

When no external field is present, a neutral atom has no dipole moment. The charge distribution will change by applying an external field, and electrons will be shifted from their equilibrium position, resulting in an induced dipole moment.

1.1.3.5.2 Orientation or Dipolar Polarization

In the absence of an external field, permanent dipole moments (for example, water molecules) are randomly oriented due to thermal activation, and no net dipole exists. By applying the external field, molecules will try to align their orientation parallel to the field to reduce the system's total energy, so dipolar polarizations occur. Applying an alternating field (in our case in the microwave region) will lag the dipole's response since they do not have enough time (and speed) to catch up with the fluctuating field, as shown in Figure 1-4. As a result, the random collision of the molecules with each other dissipates the energy as friction heat.

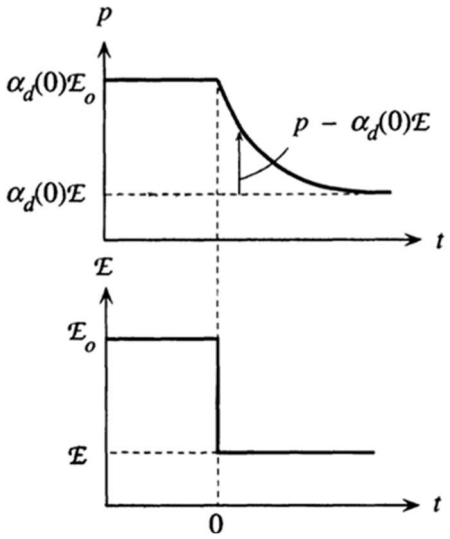

Figure 1-4 The applied DC field suddenly changes from E_0 to E at time t = 0. The induced dipole moment has to decrease achieved by random collisions of molecules in the gas [35]. $\alpha_d(0)$ is the polarizability at $\omega=0$

1.1.3.5.3 Ionic or Atomic Polarization

Unlike electronic polarization, where the only displacement of the electron charges surrounding the nuclei occurs, ionic or atomic polarization occurs due to the relative displacements of positive and negative ions or atoms within molecules and crystal structures from their equilibrium lattice sites. Figure 1-5 shows the ionic polarization mechanism of NaCl molecules in the presence of an external field.

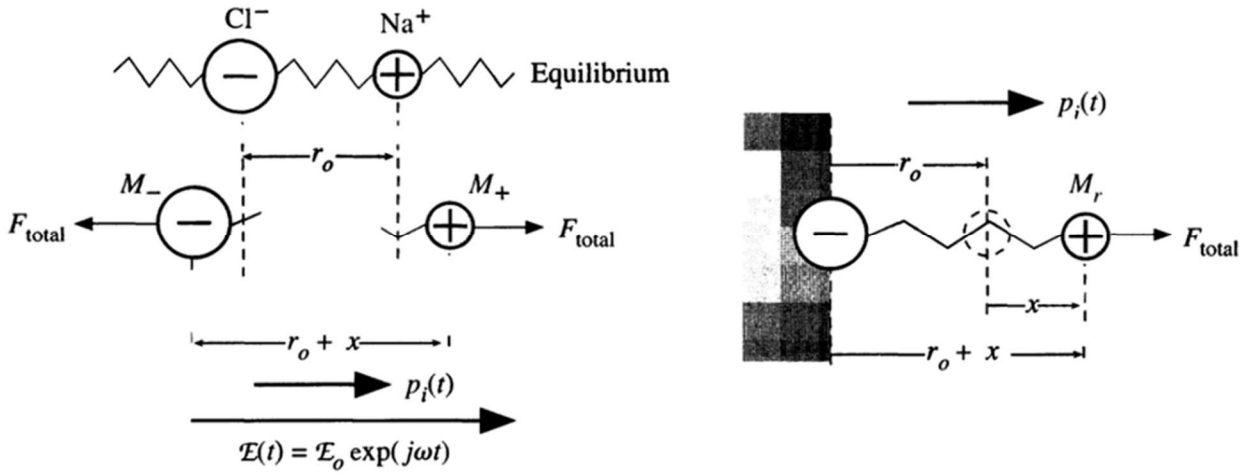

Figure 1-5 a pair of oppositely charged ions. In the presence of an applied field E along x, the Na+ and CI- ions are displaced from each other by a distance x. The net average (or induced) dipole moment is $p_i(t)$ [35]

1.1.3.5.4 Interfacial Polarization

When there is an accumulation of free charges at interfaces within the material such as defect regions, grain-phase boundaries, or between different materials, interfacial polarization (also known as Maxwell–Wagner or space charge polarization) happens.

By applying a field, the more mobile charges are readily displaced and accumulate at barriers such as grain/phase boundaries or free surfaces, resulting in interfacial polarization (See Figure 1-6).

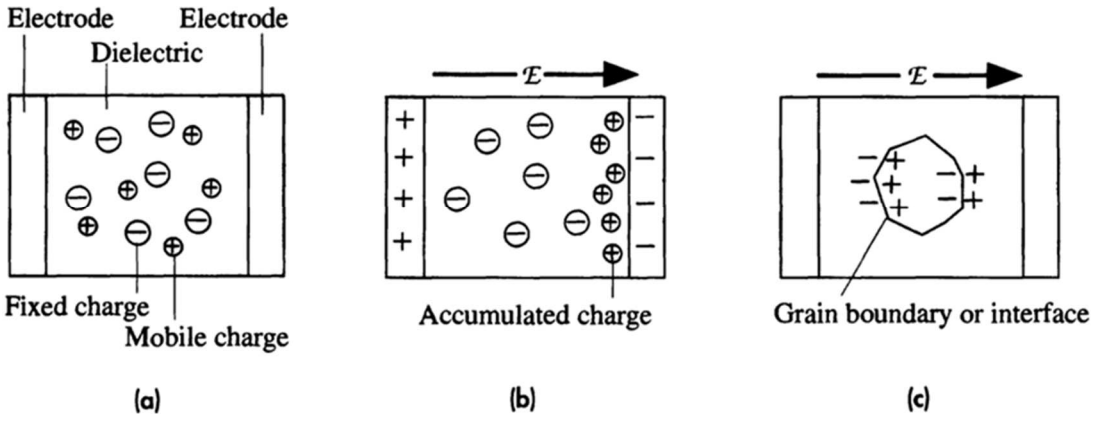

Figure 1-6 (a) A crystal with an equal number of mobile positive ions and fixed negative ions. In the absence of a field, there is no net separation between all the positive charges and all the negative charges

(b) In the presence of an applied field, the mobile positive ions migrate toward the negative electrode and accumulate there. There is now an overall separation between the negative charges and positive charges in the dielectric. The dielectric, therefore, exhibits interfacial polarization (c) Grain boundaries and interfaces between different materials frequently give rise to interfacial polarization[35]

Figure 1-7 summarizes these mechanisms for the polarization of the material. Eddy currents or magnetic induction play an essential role in heating high-conductivity materials such as metals [36]. The eddy currents induced in the conductor due to the interaction of the magnetic field produce a force that pushes the conducting electrons

outward into a narrow area near the surface [37]. Eddy current density decreases exponentially with increasing depth. This phenomenon is known as the skin effect. The use of the magnetic field to induce eddy currents in the material forms the basis for induction heating of metals.

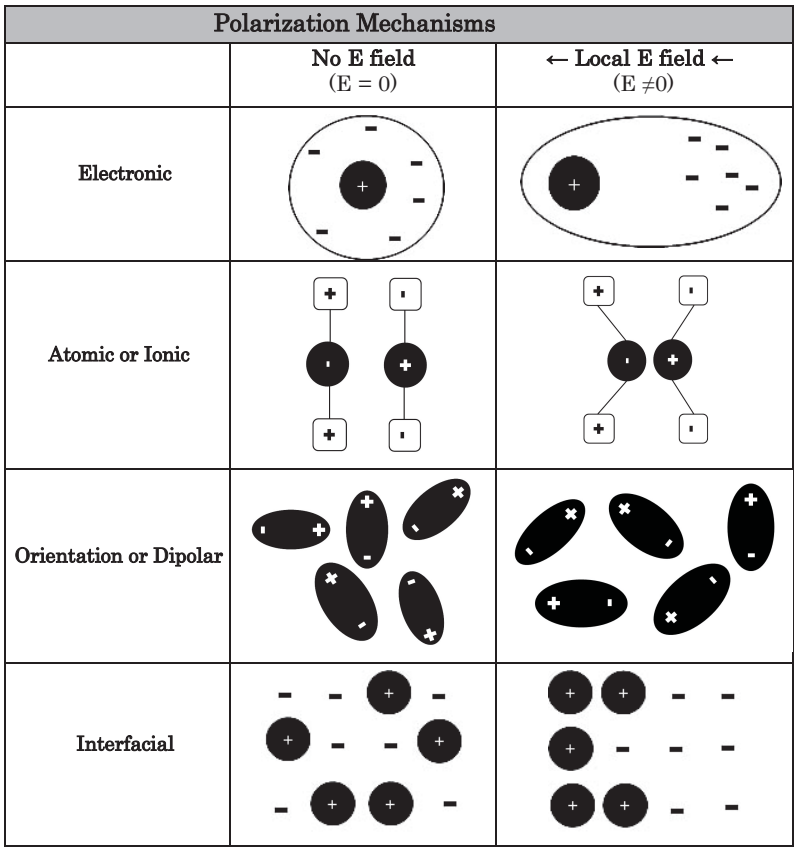

Figure 1-7 Different polarization mechanisms [34]

In the case of conductive powder compacts immersed in a relatively high-intensity electromagnetic field, other phenomena can occur, leading to a more pronounced and deeper heating of the conductive materials, like arcing and plasma formation [34]. Moreover, the oxide layer, which can be present on the metallic powders, can give a further heating contribution by dielectric heating [38].

1.1.3.5.5 Hysteresis Losses

Materials with magnetic properties (ferromagnetic) can absorb microwave energy by hysteresis loss caused by the alternating magnetic field. The energy loss per cycle is the area within the hysteresis loop. Figure 1-8 shows a typical magnetization curve.

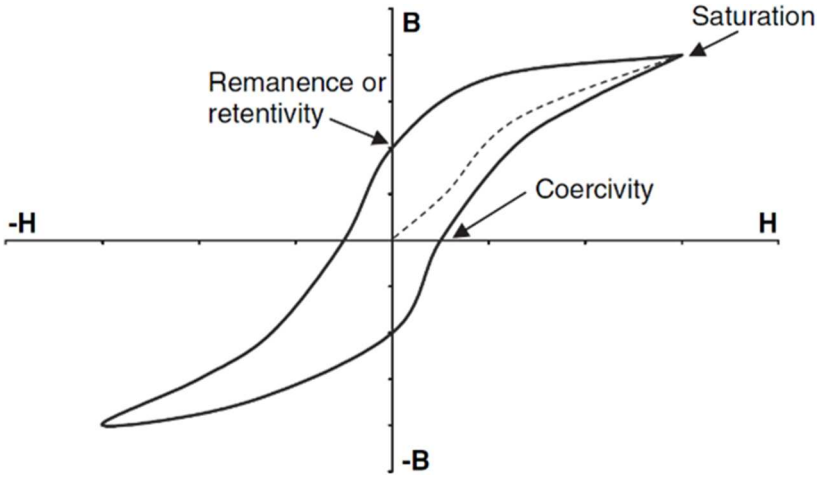

Figure 1-8 Typical B versus H hysteresis curve [34]

1.1.3.6 Frequency Dependence of Polarization Mechanisms

Polarization mechanisms are frequency-dependent. The general frequency dependence of the different polarization mechanisms in dielectrics is shown in Figure 1-9.

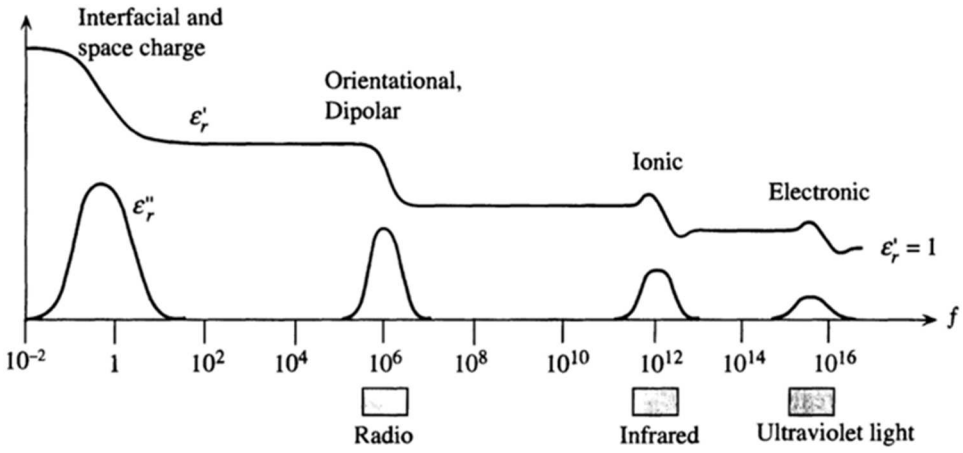

Figure 1-9 Frequency dependence of the polarization mechanisms for dielectrics

Having little inertia (p=mv, and having very small mass), electrons can follow the alternating electric fields up to high frequencies in the visible light portion of the spectrum. The vibration of atoms and ions is dependent on the thermal energy available, and the frequencies of these vibrations correspond to the infrared region of the electromagnetic spectrum. Since electronic and ionic polarization occur in the visible and infrared frequencies of the electromagnetic spectrum, they can polarize almost in phase with the alternating electromagnetic field and do not generally contribute to microwave absorption[37]. Molecules with permanent dipole moments, such as water, may have considerable mass; therefore, orientation polarization typically occurs near radio to microwave frequencies and occurs at lower frequencies compared with electronic and ionic polarization. Interfacial polarization requires the movement and accumulation of charges across the material body; hence the process occurs at much lower frequencies[34]. Therefore, the processing of dielectric materials using microwaves depends primarily on dipolar and interfacial polarization [36].

1.1.3.7 Microwave Sintering

Amongst the various methods available for ceramic processing, the use of microwaves as the energy source for synthesis and sintering of ceramics has gained substantial attention among scientists[2], [6], [12] due to its unique advantages, namely, shorter processing times and the superior quality of obtained samples. Therefore, microwave sintering opens up new possibilities, such as rapid sintering close to theoretical density values. Due to its volumetric heating nature, it could be a very cost-effective process.

In conventional heating, heat is generated by passing a current through elements that transfer heat to the sample via radiation, conduction and convection. It requires long times for sintering materials which may cause some of the constituents to evaporate, thereby modifying the desired stoichiometry and allowing undesired grain growth[16].

Volumetric heating happens when electromagnetic waves interact with the material, which originates from dielectric loss. The power generated in the ceramics is given by eq. (1-12).

$$P = \omega \varepsilon_{\circ} \varepsilon_{e}'' \left| E \right|^2 = \omega \varepsilon_{\circ} \left(\varepsilon'' + \frac{\sigma}{\omega \varepsilon_{\circ}} \right) \left| E \right|^2 \tag{1-12}$$

where E is the electric field, ε'' is dielectric loss factor, σ is the conductivity of the material, $\varepsilon_{\circ}$ is the permittivity of free space, and ω is the frequency of the microwaves[17].

Different crystal structures and loss mechanisms lead to different microwave adsorption levels for various ceramics—the degree of interaction between microwaves and ceramics changes with temperature. Most ceramics have a low absorption ability at lower temperatures but an increased absorption at higher temperatures [18].

Microwaves have been used to successfully sinter a variety of oxide and non-oxide ceramics, composites, and glass[16], [20]–[23]. Janney et al. report a microwave enhancement of 180°C for the sintering of ZrO_2-8 mol % Y_2O_3 to full density while using 2.45 GHz microwaves, although they encountered severe heat runaway, which causes cracking [23]. Most oxides are transparent to regular microwave generators (900 MHz and 2.45 GHz) since these waves are not in the range of their phonons. Increasing the temperature rapidly changes this and causes the specimen to absorb the waves. That is why it is convenient to use a susceptor material to absorb the microwaves at low temperatures and heat the specimen. Above a certain temperature, the specimen itself starts to absorb the waves. For example, Figure 1-10 shows a setup that uses SiC rods as the susceptor.

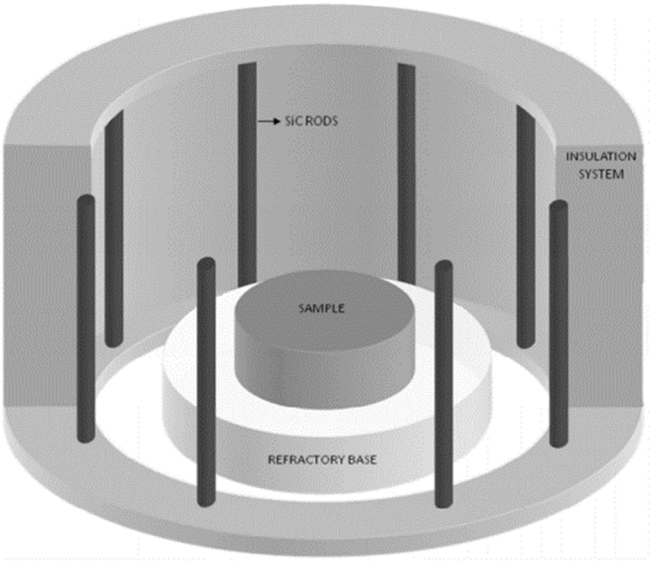

Figure 1-10 Hybrid microwave sintering. SiC rods are used to heat the sample initially[18].

1.1.3.8 Joule Heating in the Presence of Microwave

Microwave heating is only effective on metal powders or films as the bulk metal's temperature cannot increase much due to the electromagnetic field's shallow (order of micron or less) penetration depth [39]. In the case of ferromagnetic metals, microwave heating can also occur. Although the precise causes of the magnetic loss in metals in the GHz range are not always fully understood, magnetic mechanisms are thought to be the cause [40]. The induced eddy currents on the metal surface are considered the primary cause of the Joule heating of metals when exposed to an electromagnetic field. Also, the discharge current coming onto the metal surface causing arcing can cause heating by the Joule effect [41].

The Joule loss resulting from the eddy currents that the alternating magnetic field induces is known as eddy current loss. Eddy currents can form whenever there is relative motion between a conductive material and an external magnetic field [42]. In microwave processing, the Joule loss is significant in pure metals, metallic-based materials, and semiconductors. Free electrons start moving in the same direction as the external electric field E with velocity v as shown in Figure 1-11. As the conductivity of these materials is significantly high, the field experiences rapid attenuation within the material, which results in the large current I_i shown in Figure 1-11(c). An induced magnetic field (H_i) forms opposite the external magnetic field inside the material based on Lenz's law [40]. The resulting magnetic field forces move conducting electrons in the reverse direction with velocity v_r. As a result, electrons acquire kinetic energy, and their ability to move is constrained by inertial, elastic, frictional, and molecular interaction forces. This phenomenon is quickly repeated by the oscillating electric field, leading to volumetric and uniform heating inside the material, as shown in Figure 1-11 (d).

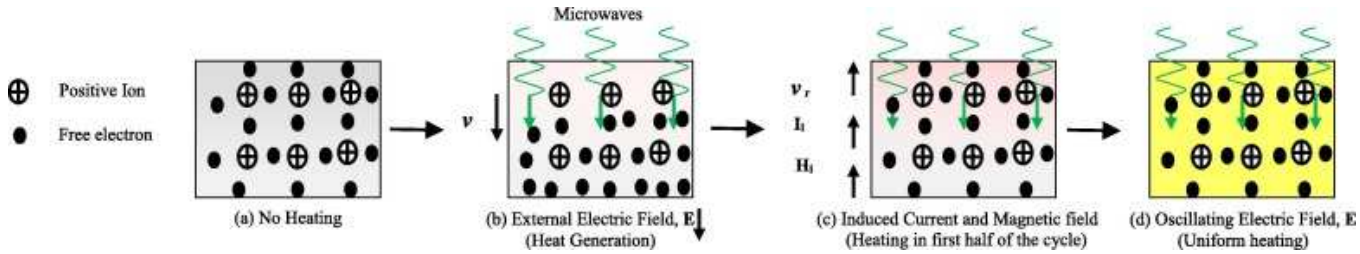

Figure 1-11 Heating mechanism in conduction loss [40]

1.2 Research motivations and objectives

Significant improvements of SOFCs in terms of cell life and power density have been possible by optimizing the cell geometry, materials, and design [43]. Despite the commercial life expectancy of SOFCs being more than two times longer than other fuel cells, material degradation complications and carbon formation during fossil fuel usage dramatically decrease their reliability [2, 3]. Excessive costs of materials and fabrication and limited lifetimes prevent wide commercialization of these devices [4]. The key is to develop robust materials and fabrication methods that increase the performance and durability at a lower cost [5].

Sintering is crucial for a high-performance cell; the electrolyte needs to be fully dense and leak-free. Conventional sintering is time consuming and expensive. Also, side reactions and the difficulty of sintering some materials need to be considered. The heating rates of ceramics can be considerably enhanced by adding a small fraction of electrically conducting powders to the specimen [24].

This study aims to address some of the mentioned shortcomings. First, we focused on an enhanced proton-conducting electrolyte that can withstand moisture and carbon dioxide with excellent power performance. Then we focused on a new in-situ method of catalyst deposition inside a porous layer as the electrode using microwave irradiation. Finally, a new way to directly microwave sinter a poorly-coupled electrolyte is developed to reduce processing time and cost significantly.

To successfully sinter ceramics, finding a way to avoid low microwave absorption at low temperatures is essential. Since even a small addition of metal powders can increase the microwave absorption and the reaction rate in solid-state reactions [36],

reducing the support before microwave sintering is being considered. Our unique method uses nickel-YSZ as the support since it can absorb the microwaves and act as a susceptor to heat the poorly coupled electrolyte until it can absorb the waves itself. Due to the fast sintering process, inhibited grain growth is expected.

1.3 Research outline

The focus of the current work was to develop new methods and materials to enhance the performance of solid oxide fuel cells and facilitate commercialization.

Chapter 2 is focused on making a complete cell using the newly developed proton conducting electrolyte. To improve the chemical stability of $BaCeO_3$, Sr at the A-site and Zr at the B-site were doped. $Ba_{0.5}Sr_{0.5}Ce_{0.6}Zr_{0.2}Gd_{0.1}Y_{0.1}O_{3-\delta}$ showed excellent chemical stability under humidity and carbon dioxide [44]. Using this electrolyte, Ni/YSZ as the support, and $La_{0.6}Sr_{0.4}Co_{0.2}Fe_{0.8}O_3$ as the cathode, a full cell was fabricated and electrochemically characterized, detailed in Chapter 2.

Microwave irradiation can be used instead of conventional heating, considering the drawbacks of the traditional sintering process, which leads to coarsening, unwanted secondary phases, and higher costs. This research used microwave irradiation to sinter the electrolyte and electrodes to improve fabrication efficiency and performance of cells. In chapter 3, microwave irradiation was used to in-situ decompose and sinter the infiltrated cathode inside the porous YSZ scaffold in a one-step heat treatment. This method was thoroughly compared with the conventional infiltration method, which consisted of two different heat treatments for

decomposition and sintering. A detailed comparison between the final product's crystal structure, electrochemical performance, and morphology is discussed.

Chapter 4 focused on a new sintering method using microwave irradiation for poorly coupled ceramics. The YSZ electrolyte with poor microwave coupling is successfully used as an example using this method. This method's microstructure, electrochemical performance, and challenges are discussed and compared with traditional heat treatment using an electric furnace.

Chapter 5 focused on using TiN to replace current anodes in solid oxide cells. TiN distinctive features and advantages are discussed, followed by the successful electrochemical reduction of TiO_2 to TiN. The same cell then can be used as a fuel cell or electrolyzer.

Chapter 6 focused on an enhanced infiltration technique using an electric field. The new method offers higher weight gain and longer penetration depth than conventional infiltration methods. A thick support confined with the electrolyte on one side was used. Nickel nitrate was used as the precursor for the infiltration. Several adjustments were used to prevent catastrophic damage to the cell during the infiltration process. The electrochemical performance shows excellent results with minimum overall resistance of the cell. Results show that this method is an effective way to enhance infiltration and improve the performance of the electrochemical devices.

Chapter 2. High Performance Tubular Solid Oxide Fuel Cell based on $Ba_{0.5}Sr_{0.5}Ce_{0.6}Zr_{0.2}Gd_{0.1}Y_{0.1}O_{3-\delta}$ Proton Conducting Electrolyte

2.1 Introduction

A solid oxide fuel cell (SOFC) is a solid-state electrochemical device which converts the chemical energy stored in the fuel directly into electrical energy resulting in high efficiency which along with low environmental impact, quiet operation, and low maintenance makes SOFC highly suitable for stationary power generation applications [7]. Traditional SOFCs employ Ni-YSZ cermet, oxide-ion conducting YSZ, and lanthanum strontium manganite as the anode, electrolyte and cathode, respectively [8]. To reduce the overpotentials associated with these materials, the cell needs to run at elevated temperatures near 1000 °C [9]. This negatively affects the choice of available materials mostly for interconnects and sealants and their long-term stability [10]. To reduce the operating temperature of SOFC, one of the alternatives is to develop new materials for cell components. Oxide ion conducting electrolytes $La_{0.9}Sr_{0.1}Ga_{0.8}Mg_{0.2}O_{3-\delta}$, $Ce_{0.8}Gd_{0.2}O_{2-\delta}$, and $Ce_{0.8}Sm_{0.2}O_{1.9}$, and mixed ionic and electronic conductor $Ba_{0.5}Sr_{0.5}Co_{0.8}Fe_{0.2}O_{3-\delta}$, $La_{0.99}Ca_{0.01}NbO_4$ and nickelates cathodes are some examples. These materials have their own drawbacks mostly related to chemical compatibility and cost resulting in limited large-scale usage [11]. Unlike YSZ which conducts oxygen ions, there has recently been a new trend in

developing electrolytes that conduct protons as shown by following equation with Kröger Vink notation [12]:

$$H_2O(g) + V_{O(s)}^{\bullet\bullet} + O_{O(s)}^{x} \rightarrow 2OH_{O(s)}^{\bullet} \quad [1]$$

where $V_O^{\bullet\bullet}$ indicates vacancy of oxide ion with effective two positive charges, and $OH_O^{\bullet}$ indicates proton attached to the regular oxygen ion sites with a positive relative charge.

Proton conducting electrolytes (PCEs) have two main advantages, first, they do not dilute the fuel which lowers the performance based on the Nernst equation [13]. Also, due to their relatively low activation energy of conduction due to smaller size of H^+, they can achieve high conductivity at lower temperatures [14-16]. Iwahara et al. first reported high proton conductivity ($\sigma \sim 10^{-2}$ S cm^{-1} at 600 °C) in perovskite type-doped-$SrCeO_3$ and $BaCeO_3$ ceramics under humid atmospheres in the early and late 1980s [18, 19]. But cerate based perovskites face the problem of poor chemical stability in the presence of moisture and CO_2, which is a major hindrance for commercial realization [20, 21]. As humidity is present in every fuel cell, and CO_2 is produced when hydrocarbons are used as fuel, this is an important issue for researchers to solve. On the other hand, zirconate based perovskites are stable, both mechanically and chemically [23]. However, zirconate based perovskites such as $BaZrO_3$ show lower electrical conductivity than cerate based oxides, due to large grain boundary resistance, which arises due to low sinterability and hence is also rather hard to sinter a leak-free PCE usually needing temperatures exceeding 1600 °C, hampering

its actual usage [17, 24, 25]. Thus researchers have worked towards solid solutions between $BaCeO_3$ and $BaZrO_3$ in order to achieve good chemical stability and high proton conductivity [24, 26].

Tubular SOFC has two main advantages over the planar design. First, ease of sealing especially if the tube has only one open end which greatly reduces the chance of cell failure due to sealant degradation and enables the cell to be run under high pressure operation [45]. Second, it has more resistance toward thermal shock which improves the start-up times [29]. The main drawback of this design would be its lower performance compared to its counterpart mainly due to the longer path current must take to reach the current collector [46].

Power density of the tubular SOFC is inversely related to the diameter [28]. Zhang et al. [47] reported high peak power density of 513 mW/cm^2 at 850 °C for a tube with outer diameter of 1.3 mm and 1.03 V for the open circuit voltage (OCV) with a YSZ electrolyte. Duan et al. [48] achieved 522 mW/cm^2 at 850 °C. With the help of PdO impregnation, this result jumped to 1220 mW/cm^2 at the same temperature. The outer cell diameter was 10.5 mm and the electrolyte was YSZ. Hanifi et al. [21] reported maximum performance of 416 mW/cm^2 at 700 °C using $BaZr_{0.1}Ce_{0.7}Y_{0.1}Yb_{0.1}O_{3-\delta}$ but saw rapid degradation under $CO\text{-}H_2$ mixtures.

In previous work, we have developed and reported a PCE based on $Ba_{0.5}Sr_{0.5}Ce_{0.6}Zr_{0.2}Gd_{0.1}Y_{0.1}O_{3-\delta}$ (BSCZGY) with excellent chemical stability under humidity and carbon dioxide [44]. For improving chemical stability, Sr at the A-site and Zr at the B-site were doped into $BaCeO_3$ [44]. For increasing ionic conductivity,

aliovalent Gd and Y were doped at the B-site of $BaCeO_3$ [44]. In the subsequent report, mechanically mixed Ni-BSCZGY (50:50 vol. %) anode composite exhibited area specific resistance (ASR) of 0.8 $\Omega.cm^2$ at 710 °C under H_2+3vol.% H_2O [49]. By the same analogy to oxygen conductor SOFCs, if we use a PCE/Ni cermet as support, we face some challenges as well. Cerates have large thermal expansion coefficients due to the reduction of Ce^{4+} to Ce^{3+} which results in cell degradation in long-term operation [50]. Zirconates have poor sinterability and thus not ideal mechanical properties as the support [44]. Ni/YSZ can still be used instead to provide sufficient rigidity and electronic conductivity of the cell without performance penalty but extra caution needs to be taken to match the shrinkage of the support and the electrolyte [51]. Bae et al. [52] successfully used Ni/YSZ both for the support and anode functioning layer to make a thin film proton conductor fuel cell with a heterogenous structure to mitigate sintering shrinkage mismatch, achieving more than 1 V in open circuit. This study is aimed at using this stable proton conductor as the electrolyte in a complete cell consisting of both an anode and cathode to evaluate its electrochemical performance.

2.2 Experimental

2.2.1 PCE synthesis.

Proton conducting electrolyte with the following nominal chemical composition $Ba_{0.5}Sr_{0.5}Ce_{0.6}Zr_{0.2}Gd_{0.1}Y_{0.1}O_{3-\delta}$ (BSCZGY) was synthesized via conventional solid-state synthesis method, as reported in the previous report [44]. Stoichiometric ratios

of $BaCO_3$, $SrCO_3$, CeO_2, ZrO_2, Gd_2O_3, and Y_2O_3 (~99.9%, Alfa Aesar) were first mixed and ball-milled with 10 mm zirconia balls and iso-propanol as solvent in 50 mL zirconia ball mill jars (Fritsch planetary ball mill, Pulverisette 5) for 6 h. Iso-propanol from milled powders was evaporated at 90 °C and then powders were pre-treated at 1050 °C for 24 h under air in an alumina crucible, followed by a second milling for 6h. After second milling, powders were uni-axially pressed at 200 kN pressure into cylindrical discs (~2 cm thickness, ~1 cm diameter). Cylindrical discs were then calcined twice at 1450 °C for 24 h under air in an alumina crucible, with milling and pelletisation steps in between. In order to avoid reaction with the alumina crucible and Ba evaporation, cylindrical discs were kept on and covered by parent powders. Resulting pellets after final sintering were ground to fine powders in a mortar and pestle for powder-X ray diffraction (PXRD), chemical compatibility, and electrochemical analyses.

2.2.2 Support fabrication.

As-received YSZ (Tosoh TZ-8Y) and NiO (Aldrich, <50 nm particle size) were mechanically ball-milled together with 35:65 weight ratio in water medium (1:1 ratio) for 24 h. To create enough porosity, 30 volume % graphite (Sigma Aldrich <325 mesh) was added to the mixture followed by final pH adjustment to 4. Slip casting in a plaster mold was used to make the support. By controlling the time, a suitable thickness of support can be cast, and the excess slurry removed. The supports were

pre-sintered at 1000 °C for 3 h to gain sufficient strength and remove pore-former and water.

2.2.3 Anode functional layer (AFL) fabrication.

NiO, PCE, ethanol and binder (6 wt% ethyl cellulose in terpineol) with appropriate ratio were mixed together and ultrasonicated to remove any undesirable agglomeration or air bubbles. The AFL was dip coated and pre-sintered at 1000 °C for 3 h.

2.2.4 Electrolyte coating.

Electrolyte suspension was a mixture of PCE, ethanol and binder. Similar to the AFL coating, the coating continued until desirable electrolyte thickness of 10 micron was reached. Sintering was done at 1450 °C for a leakage-free electrolyte.

2.2.5 Cathode coating.

A mixture of $La_{0.6}Sr_{0.4}Co_{0.2}Fe_{0.8}O_3$ (LSCF, Fuel Cell Materials)-BZCZGY, azeotrope solvent, polyvinyl butyral as binder, Menhaden fish oil as the dispersant and 30 vol.% graphite was used for cathode ink. The resulting mixture was dip coated on top of the electrolyte followed by sintering at 1000 °C to form a LSCF-BZCZGY cathode. The top and base diameter of the cell was 5.5 mm and 5.23 mm, respectively, with a length of 33 mm and total area of 1.79 cm^2 for the cathode.

2.2.6 Chemical compatibility between PCE and electrodes.

The chemical compatibility of the PCE electrolyte with the LSCF (synthesized through sol-gel route) and NiO (Alfa Aesar) powders, was investigated by co-firing the powders at 1000 °C and 1450 °C, respectively, and analyzing the fired powders through PXRD. LSCF and BSCZGY powders (50:50 and 70:30 wt %) were mixed and milled for 6 h with iso-proponol, and were fired at 1000 °C for 3h with a heating rate of 5°/minute and cooling rate of 10°/minute. Similarly, NiO and BSCZGY powders (50:50 wt. %) were ball milled for 6 h with iso-propanol followed by co-firing at 1450 °C for 3h with the heating rate of 5°/minute and cooling rate of 10°/minute. Bruker D8 powder X-ray diffractometer with CuKα was used to analyze the phase purity of co-fired electrolyte and electrode powders.

2.2.7 Electrochemical characterization.

An Agilent electronic load (model # N3301A) was used to measure the OCV and I-V curves. An Agilent scanner (model # E4970A) monitored the thermocouples, while LabView software was used for automated measurements and data collection. Electrochemical impedance spectroscopy (EIS) measurements were used to measure the area specific resistance (ASR) of the cell with a four-probe configuration using a Solartron 1255 frequency response analyzer in combination with a Solartron 1287 electrochemical interface. The frequency range of measurement was between 0.01Hz - 1MHz with 12 points per decade. The data were recorded with 50 °C interval in a

temperature range of 600 °C – 850 °C using a four-probe setup with H_2 +3vol.% H_2O as fuel and air as the oxidant

2.2.8 Microstructure characterization.

The study on the microstructure of the prepared cell was conducted on the fractured samples using a Zeiss Sigma 300 field-emission scanning electron microscope (SEM). Carbon coating of the samples was done using a Leica EM SCD005 evaporative carbon coater.

2.3 Results and discussion

2.3.1 Chemical compatibility.

Figure 2-1a and Figure 2-1b show the PXRD patterns of mechanically mixed NiO and BSCZGY powders (50:50 wt.%) at room temperature, and the co-fired powders at 1450 °C. Figure 2-1 (a) only shows the diffraction peaks of NiO and BSCZGY phases, and no additional diffraction peak of second-phase impurities such as $BaNiO_x$, BaY_2NiO_5. As in the previous report [53], it has been shown that there is a possibility that Ni might substitute on the Zr site during mechanical mixing or firing at high temperatures owing to their similar ionic radii (rZr^{4+} = 0.72 Å, rNi^{2+} = 0.69 Å). Figure 2-1 b shows the magnified PXRD pattern where it can be seen that there is a very slight shift of BSCZGY (110) peak to high 2θ after firing, which indicates slight or no substitution of Ni in the Zr/Ce site of BSCZGY, indicating no change in stoichiometry of the BSCZGY electrolyte.

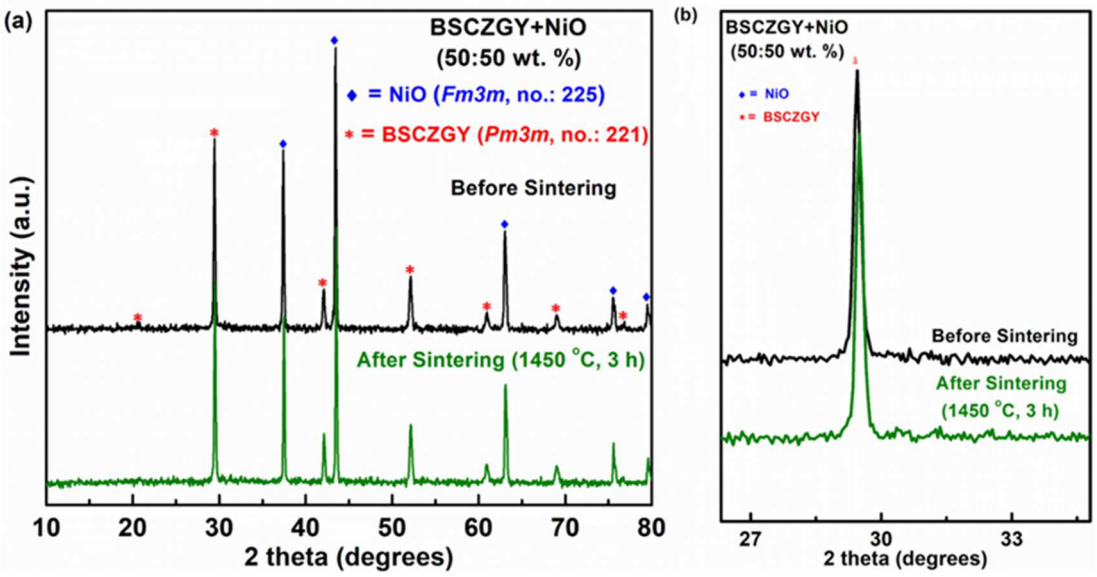

Figure 2-1 (a) XRD patterns of the fresh mixed and fired mixed powders containing NiO and BSCZGY with a weight % ratio of 50:50. (b) Magnified XRD patterns for (a)

Similarly, Figure 2-2 shows the room temperature PXRD patterns of mechanically mixed LSCF and BSCZGY (50:50 and 70:30 wt.%) powders, and the mixtures co-fired at 1000 °C.

Even though the main cubic (*Pm3m*) perovskite phases for both BSCZGY and LSCF remained the same as the mechanically mixed powders at room temperature, the (111) peak of CeO_2 appeared after firing at 1000 °C. When comparing this result to the NiO and BSCZGY compatibility result, the tendency of LSCF to react with the electrolyte at firing temperature above 800 °C might be responsible for some secondary reactions that occur at the interface between the cathode and BSCZGY resulting in the appearance of CeO_2 as a separated phase [54, 55].

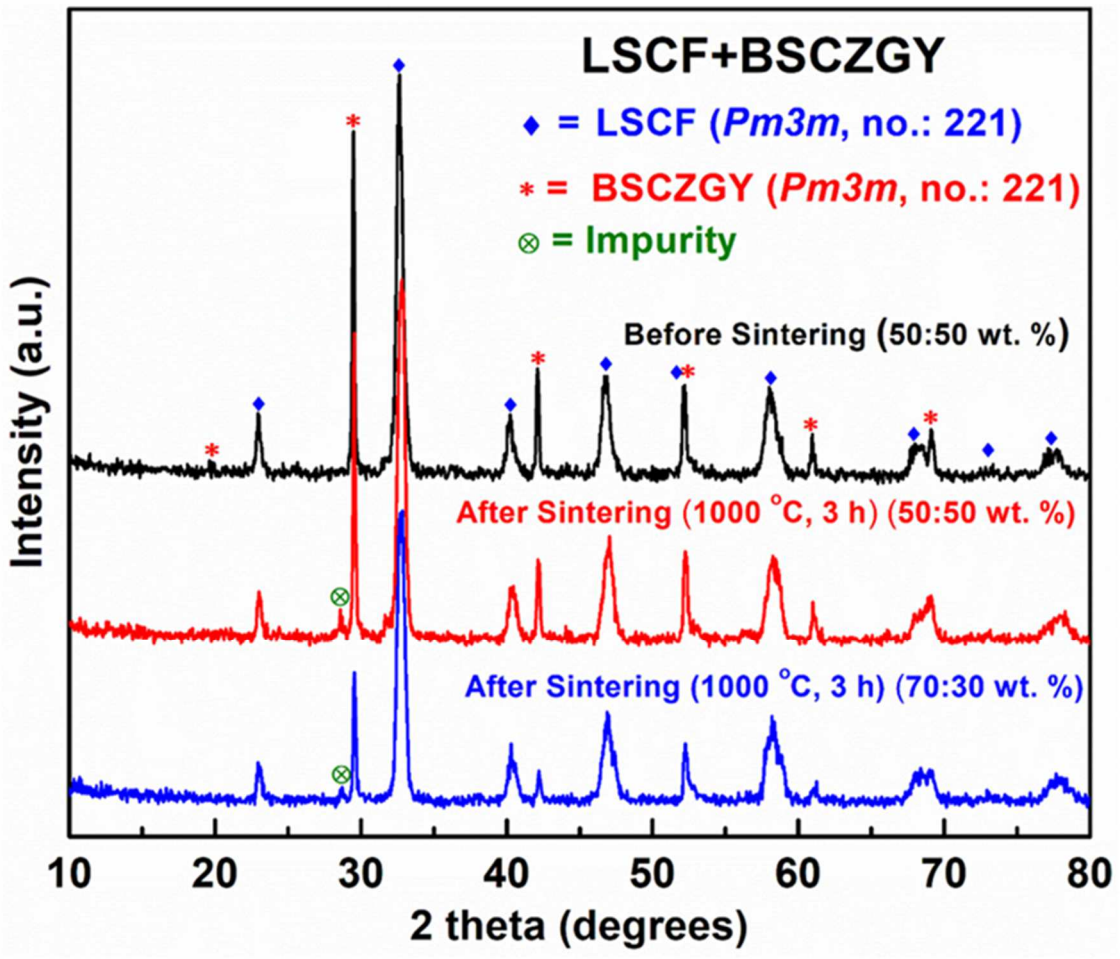

Figure 2-2 XRD patterns of the fresh mixed and fired mixed powders containing LSCF and BSCZGY with a weight % ratio of 50:50 and 70:30. Where fired powders show probable impurity (111) peak of CeO_2.

2.3.2 Electrochemical performance.

Figure 2-3 shows the I–V and power density output curves of the cell measured under air/H_2+3vol.% H_2O.

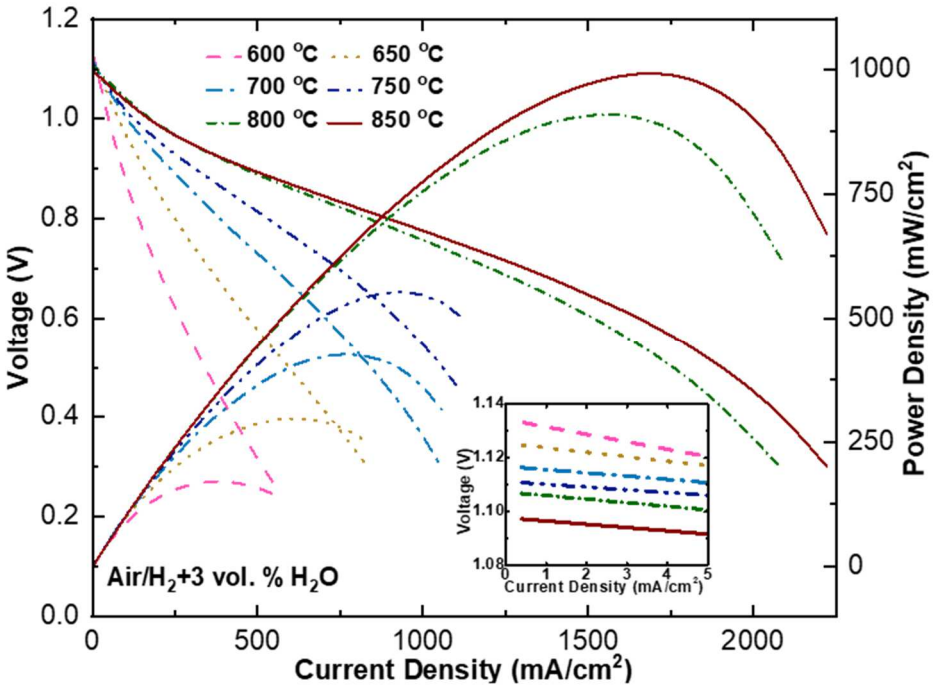

Figure 2-3 Electrochemical performance of the cell air / H2 + 3 vol. % H2O as a function of temperature.

The optimum temperature for operating the cell was found to be above 800 °C with the maximum performance of 1 W/cm^2 achieved at 850 °C, making this cell a high temperature SOFC. The almost linear behavior of I–V data especially at higher temperature indicated ohmic behavior, the majority of the loss coming from the electrolyte and the connections. At higher currents, especially for 800 °C and 850 °C, the end of the curves which signifies fuel starvation, becomes more significant. By increasing the temperature, OCV decreases and the values get closer to theoretical expectation based on the Nernst equation, suggesting a dense electrolyte that prevents charge transfer or gas diffusion directly between the two electrodes.

Nyquists plots of the cell are shown in Figure 2-4 (a) under open-circuit conditions. The R0-(CPE1-R1)-(CPE2-R2)-(CPE3-R3) equivalent circuit was used to fit the impedance spectrum similar to previous work [44]. As expected, an increase in temperature reduces both ohmic and polarization contributions to overall cell resistance. Figure 2-4 (b) shows that at both 800 °C and 850 °C, similar ohmic contributions are observed, indicating that electrolyte conductivity appears to have increased slightly after 800 °C. This can be ascribed to progressive dehydration at elevated temperatures and increase in oxide ion or electronic conductivity, leading to decrease in proton conductivity due to lower proton concentration [24, 56].

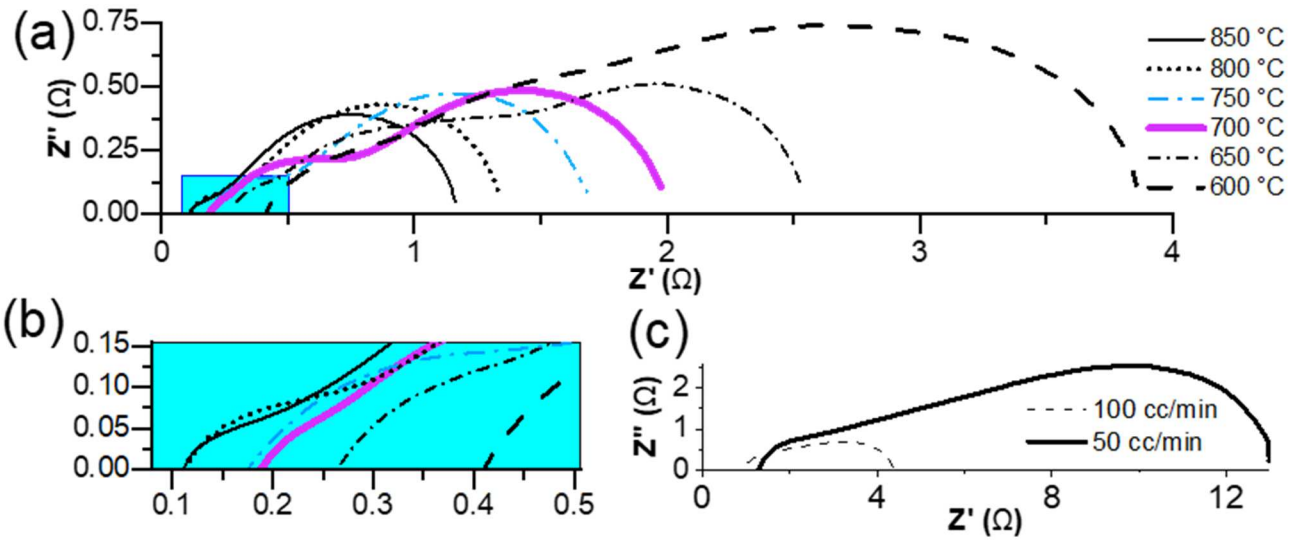

Figure 2-4 (a) Nyquist plots (not normalized) of cell at different operating temperatures (b) closer near origin (c) effect of oxidant flow on impedance spectrum at T = 600 °C.

The far-right polarization arc belongs to a mass transfer occurring at the electrodes [57] with $\omega_{max} = 6-8\ Hz$ and capacitance in the range of 0.1 F; it has arisen both from

the cathode contribution [58] and surface electrochemical reactions at the anode [49]. Our results also show that this portion is extremely dependent on the flow of oxidant as shown in Figure 2-4 (c). Fuel flow has similar outcomes, but its effect was hampered due to the non-preheating fuel injection and deteriorating effect of cooling of the cell which both lowers the performance and becomes problematic in the long run.

2.3.3 Ohmic and polarization contributions and activation energy

Since proton conduction is a thermally activated process, the proton can be pictured as a trapped charge in an elastic crystal field and thus satisfies the definition of a polaron and resembles a polaron-type conductivity with Arrhenius behavior [59]. LSCF follows a polaron conduction regime as well [60]. Activation energy E_a depends on the concentration of charge carriers and can be related to electrical conductivity as shown in following equation [61]:

$$\sigma T = \sigma_{\circ} \exp\left(\frac{-E_a}{k_B T}\right) \qquad [2]$$

In equation 2, k_B is the Boltzmann constant, T is absolute temperature and $\sigma_{\circ}$ is the pre-exponential factor mostly involving the carrier concentration in the material [62]. Using the data obtained from the fitting of impedance curves, the activation energy can be calculated from the slope of ln (T/resistivity) versus 1000/T plots as can be seen in Figure 2-5 for both the polarization and ohmic parts. This figure also shows total resistance at each temperature point. The approximately linear slope indicates that

the conduction mechanism remains the same in the temperature range of 600-850 °C [63]. If we consider the electrolyte contribution to be entirely from the ohmic part, then the activation energy is estimated to be around 0.53 eV similar to the value reported previously [64]. Since 30% of the cathode is PCE, the activation energy of 0.39 eV seems logical knowing that the value for pure LSCF is 0.21 eV [60].

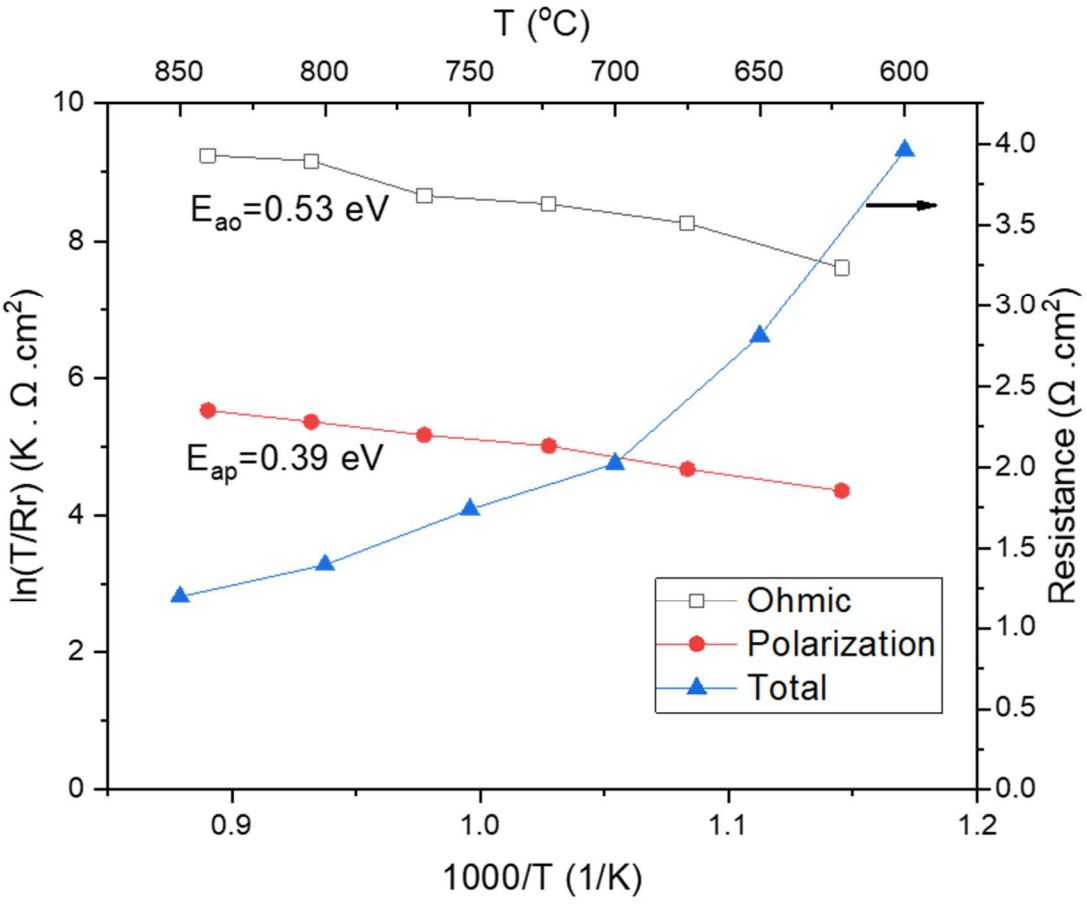

Figure 2-5 Arrhenius plots of resistivity as a function of temperature and activation energy values calculated from ohmic and polarization part of impedance. The lines passing through symbols are only guide for the eyes.

2.3.4 Long-term degradation.

Figure 2-6 shows the long-term run of the cell under load for four consecutive days. The voltage is kept constant at 0.7 V and the current is measured over time. Fluctuations in current are mainly due to imperfect current collector attachment especially at the anode side and coarsening of the electrode particles [65]. After four days, some slight variation was observed but there was no significant decrease in the performance compared to the start of the test.

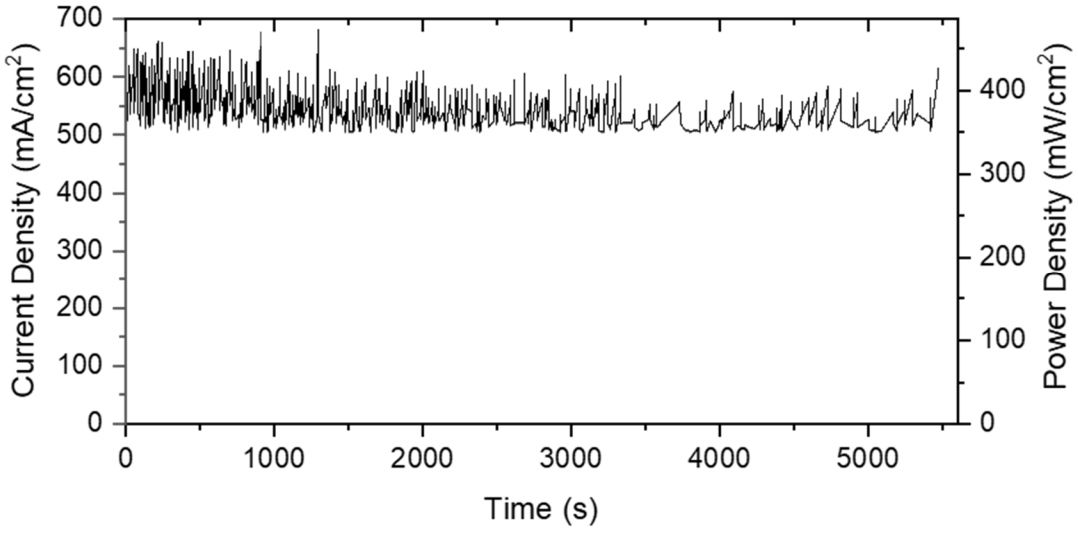

Figure 2-6 Long-term performance of cell under load at 0.7 V.

Figure 2-7 shows the impedance spectrum initially, after 18 hours, and at the end of the test after four days, verifying no major degradation during the test. The ohmic contribution shows a slight increase in magnitude mainly due to imperfect attachment of mesh on the anode side. The activation portion of the polarization sees a hike which is mainly due to coarsening and lowering of the number of active sites.

Polarization resistance is the main mechanism for degradation of the cell in agreement with other reported results [66-68].

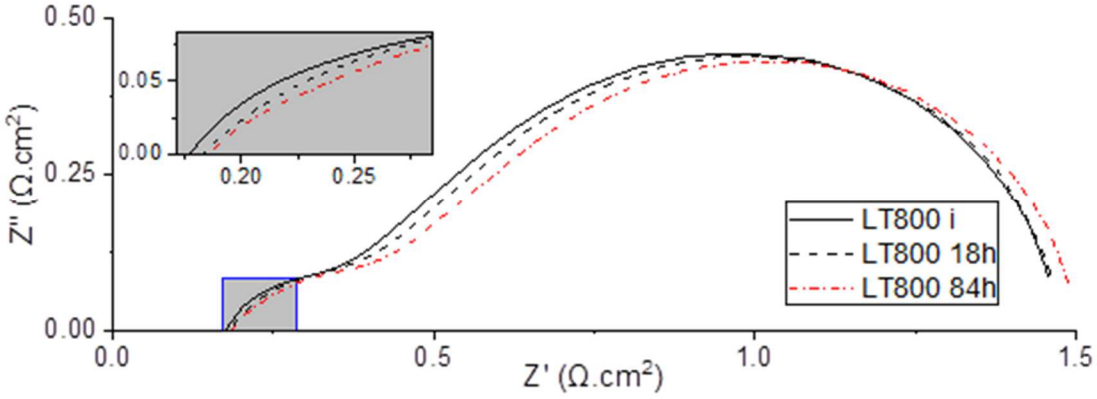

Figure 2-7 Long-term run impedance spectrum.

2.3.5 Cell microstructure after electrochemical tests.

Figure 2-8 shows the cross-section micrograph of a broken cell. The total thickness of the cell is estimated to be around 410 microns with the AFL and electrolyte about 8 and 10 microns, respectively. The cathode is estimated to be 25 microns in thickness. The far right side of Figure 2-8 (a) shows the gold current collector. To achieve superior performance, it has been suggested to design a dual layer microstructure comprising an outer layer having coarser particles that act as a conduction layer while the second one near the electrolyte consists of fine particles known as the AFL that has a high electrocatalytic activity which results in a decrease in activation polarization [69].

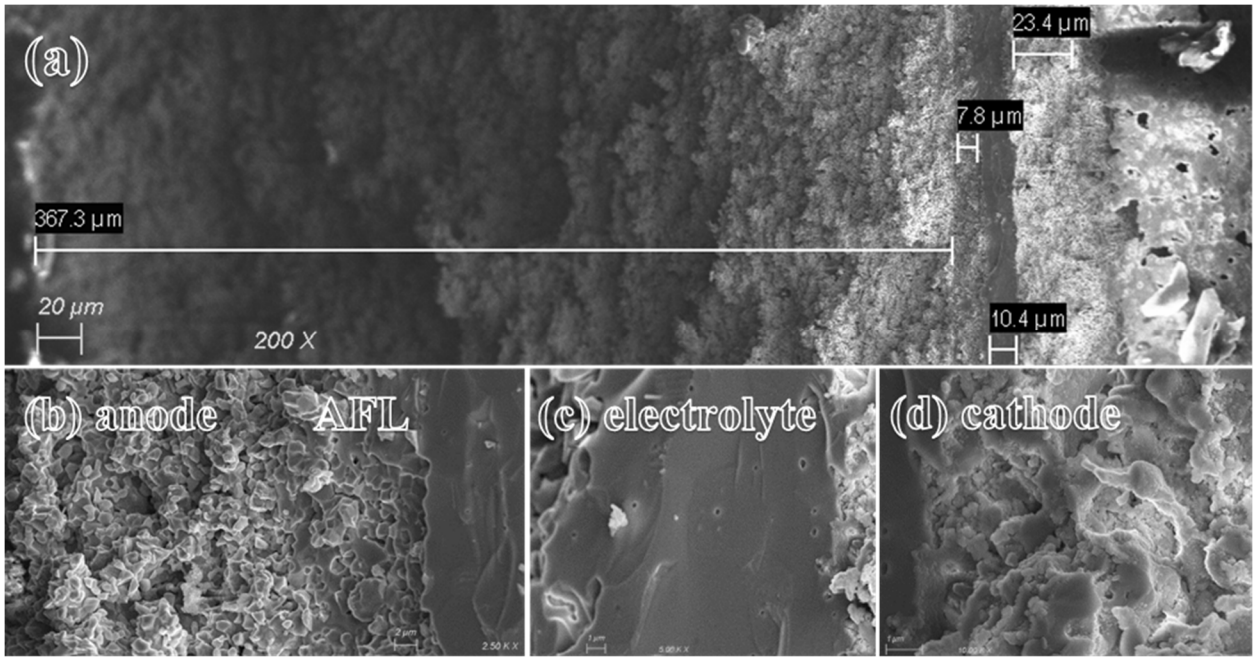

Figure 2-8 SEM images of cross-section view of the (a) whole cell, (b) from left to right, anode, AFL, electrolyte, (c) electrolyte, and (d) cathode after electrochemical testing in the air/H_2 + 3 vol.% H_2O.

Based on Figure 2-8 (a) and (b), the support is evenly distributed, although the high sintering temperature results in lower overall porosity and causes higher concentration polarization as previously observed. More tailoring of the microstructure seems essential, allowing the fuel to reach the functional layer more easily. The density of the AFL seems satisfactory, having enough active sites to convert hydrogen atoms to ion species. The electrolyte in Figure 2-8 (c) is fully dense thanks to nano-grain precursors that were made using the sol-gel method. Adherence looks satisfactory with no gaps in between and a smooth transition from the support to the AFL and to the electrolyte. The composite cathode in Figure 2-8 (d) consists of

a BSCZGY matrix with LSCF particles dispersed in it. BSCZGY guarantees good bonding and ionic pathways for reactants and LSCF contributes electronic conductivity and is an excellent catalyst for the oxygen reduction reaction at the cathode generating a volumetric active region rather than a thin film one.

2.4 Conclusions

A tubular SOFC based on a BSCZGY electrolyte was prepared using slip casting and dip coating. Investigations on chemical compatibility of the anode-electrolyte and electrolyte-cathode combinations revealed no major obstructive secondary phases resulting due to the sintering process. The dependence of performance on temperature was studied, achieving maximum 1 W/cm^2 at 850 °C, one of the highest powers reported so far on tubular proton conductor SOFCs. The conductivity of the electrolyte changes only slightly above 800 °C. Impedance analysis revealed the major part of the resistance comes from polarization, dominated by bulk diffusion, which is the bottleneck for performance and makes it essential to optimize cell microstructure. The micrograph also confirms this understanding. Satisfactory long-term results seen for four day run under load and impedance confirms negligible degradation. Detailed investigation of activation energies calculated both for the electrodes and electrolyte shows similar activation energies as reported in the literature. Therefore, this SOFC based on BSCZGY would be a suitable candidate for practical applications, especially in power generation and solid membrane reactors.

Chapter 3. Using Microwave Irradiation for In-situ Infiltration of Electrodes in Solid Oxide Fuel Cells

3.1 Introduction

Solid oxide fuel cells (SOFCs) are a class of fuel cells characterized by a solid oxide ceramic as the electrolyte. The advantages of this class of fuel cells include high efficiency, fuel flexibility, low emissions, and relative cost [70]. One of the biggest challenges for SOFCs is its inferior power output compared to proton-exchange membrane fuel cells and its inadequate long-term stability due to the high working temperature, leading to a higher degradation rate [71]. To tackle the latter, much of the efforts focus on reducing the operating temperature without significant performance loss [68]. In electrode-supported SOFCs, due to a substantial reduction in the electrolyte thickness, voltage loss is dominated by polarization of the electrode reactions [72]. Thus, improving the structural and functional characteristics of electrodes are crucial, especially the cathode, as it is generally where the highest voltage loss occurs in a solid oxide fuel cell [67].

Wet impregnation, either in the form of salt precursors or a slurry of fine particles into a porous scaffold, is an effective way to achieve this goal. Impregnation is usually carried out to enhance catalytic activity by maintaining a higher surface area thanks to the lower required sintering temperature which results in finer particles. Higher electrical conductivity could also be achieved as this technique provides optimized

interconnected pathways both for electrons and ions [73]. Infiltration approaches might involve depositing the catalyst material on top of the barebone scaffold, usually an ionic conductor [74], or depositing additional phase(s) to improve the catalytic activity of the electrode that is already present [75].

Amongst the various methods available for ceramic processing, the use of microwaves as an energy source for synthesizing and sintering ceramics has gained substantial attention [76-78]. Advantages include shorter processing times and superior quality of obtained samples compared to traditional heating methods [79]. The higher heating rate of microwaves leads to less coarsening than conventional electric furnaces, resulting in higher surface area (13) and highly porous final microstructures due to a large amount of flowing outgas arising from self-combustion [80]. Thus, a higher performance electrode and, consequently, a fuel cell can be achieved by using microwave irradiation [81].

This research aims to combine the advantages of both wet impregnation and microwave irradiation to synthesize in-situ electrodes in the porous scaffold. The cathode is the main focus of this research, yet it could easily be extended to the anode since similar precursors and methods could be used. $La_{0.6}Ca_{0.4}Fe_{0.8}Ni_{0.2}O_3$ (LCFN) was chosen as a mixed ion-electron conductor (MIEC) cathode due to its excellent electrochemical performance, high electronic conductivity, and good redox stability [82, 83]. Considering the long-term operation, which is essential for commercialization, tubular geometry was chosen as brittleness, thermal shock, and sealing problems associated with planar cells could be largely mitigated. Our goal

was to obtain comparable power output to planar designs, as usually tubular cells have about half the performance of similar planar designs [84]. For a better understanding, a detailed comparison between two identical samples, one prepared using microwave irradiation for in-situ deposition of the cathode and the other using traditional electric furnace heat-treatment was conducted.

3.2 Material and methods

3.2.1 Support fabrication

As-received YSZ (Tosoh TZ-8Y) and NiO (Baker) with a 35:65 weight ratio were mechanically ball milled together in a water medium (1:1 ratio) for 3 h. 30 volume % graphite (Sigma Aldrich <325 mesh) was added to the mixture to create enough porosity followed by pH adjustment using HCl to 4.0 to improve the stability of the suspension as explained in more details elsewhere[73]. Slip casting in a plaster mold was used to make the tubular support. The green supports were pre-sintered at 1000 °C for 3 h in air to reach sufficient strength.

3.2.2 Electrolyte coating

Dip coating was used to put a thin electrolyte on top of the support, as described in detail elsewhere [85]. In short, appropriate amounts of as received YSZ, ethanol, and binder were ball milled for an hour. The resulting slurry was then coated, followed by ambient temperature drying for 10 min. The procedure was repeated twice. The tubes were then sintered at 1400°C for 3 h in air to produce a leak-free electrolyte.

3.2.3 Thin porous layer

Calcined YSZ (1500 °C for 3 h, CYSZ) was ball milled for 72 h in the water medium, Dried CYSZ, then mixed with graphite (20 vol.%), dispersant (Menhaden fish oil), azeotropic solvent (toluene/ethanol), and binder (polyvinyl butyral), was coated on top of the electrolyte by dip-coating once to make the thin porous layer (TPL). Then the tube was sintered at 1350 °C in air for 3 h to prepare the scaffold for infiltration. The TPL area was then measured to determine the active area of each cell.

3.2.4 Infiltration process

Appropriate amounts of metal salt precursors were dissolved in deionized water and Triton X-45 surfactant (5.8:1:0.3 wt % ratio) as explained in more detail elsewhere [86]. Surfactant was added to improve the wettability of the solution and to develop a more uniform coverage of the cathode over the porous matrix [87]. Before infiltration, cells were dried at 120 °C for 1 h, and the infiltration solution was pre-heated to 100 °C. Two batches were prepared to compare the post-heat treatment effect on infiltration, one using a microwave oven (LCFN-M) and the other using a conventional electric furnace (LCFN-C). Figure 3-1 shows the overall scheme of how samples were prepared.

In the case of LCFN-M, a microwave oven (Panasonic NN-CD989S) was used. The inner chamber was pre-heated to 190 °C, and microwave power was set to 30% (330 W) to prevent possible thermal runaways.

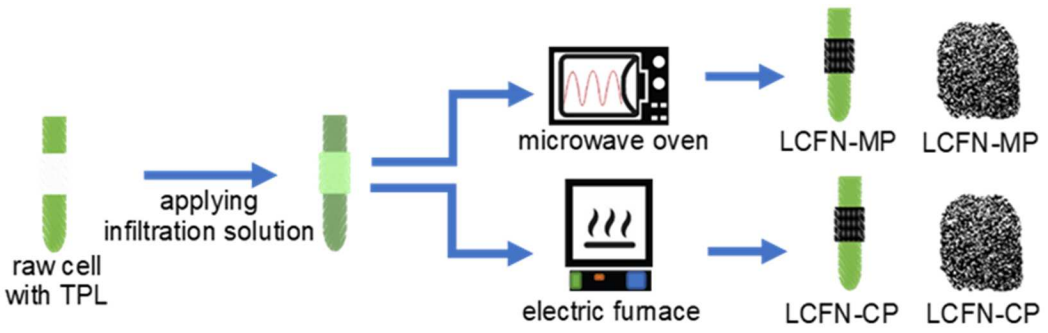

Figure 3-1 Schematics of sample preparation.

The total irradiation period was limited to 3 min as no more visible activity was observed after that. The green precursor starts to swell rapidly during radiation, and self-ignition follows quickly with a very bright flame and a massive amount of flowing outgas. For final phase formation, an additional sintering process was done on LCFN-C at 800 °C for 3 h and 28% cathode weight loading resulted. For LCFN-C, the sample was transferred to a pre-heated electric furnace and left there for 10 min at 400 °C. Then the excess cathode was removed using a soft cloth, and cathode precursors were re-applied. For similar cathode loading as LCFN-M, this procedure was repeated four times. In the last step, a gold paste was painted on top of the cathodes as current collectors with gold wires as leads; copper mesh and wires were used for the anode side.

3.2.5 Phase characterization

For X-ray diffraction (XRD), two batches with the same recipe and heat treatment for each infiltrated sample were prepared and ground using a mortar and pestle and

named according to their heat treatment process (LCFN-MP microwaved powder and LCNF-CP for electric furnace heat treatment).

Since the final phase was not detected by XRD of LCFN-CP (not shown), an electric furnace performed additional heat treatment at 800 °C for 3 h. XRD patterns of samples were recorded at room temperature using a Philips X'Pert-MPD (Brag-Brentano geometry) diffractometer with Cu-Kα radiation. The scan conditions were 30 kV and 20 mA, and data were collected over the angular range of $10° \leq 2\theta \leq 100°$ with a step size of 0.02° and a step time of 1 s.

3.2.6 Electrochemical characterization

Electronic load and scanner (Agilent models N3301 and E4970A) were used to obtain the current-voltage curves. Electrochemical impedance spectroscopy (EIS) measurements with a four-probe configuration were carried out to assess the polarization and resistance of cells using a combination of a Solartron 1255 frequency response analyzer and Solartron 1287 electrochemical interface. The frequency range is set to be between 0.01Hz - 1MHz with 12 points per decade. The data were recorded at 50 °C intervals in the temperature range of 600 °C – 800 °C with H_2 +3 vol.% H_2O as fuel feed and air as the oxidant. Distribution of relaxation times (DRT) was calculated using DRTTOOLS based on Tikhonov regularization with Gaussian discretization [88].

3.2.7 Microstructure characterization

The microstructure of tested cells and synthesized powders was analyzed using a Zeiss Sigma 300 field-emission scanning electron microscope (SEM). Carbon coating of the samples was done using a Leica EM SCD005 evaporative carbon coater.

3.3 Results and discussion

3.3.1 Phase characterization

Figure 3-2a shows the diffraction pattern of LCFN-MP, its Rietveld calculated lines, and their differences. It was determined that LCFN-MP has an orthorhombic structure with Pnma space group and lattice constants of a = 5.5441 Å, b = 7.7108 Å, and c = 5.4512 Å consistent with values reported elsewhere [83]. LCFN-CP showed a similar crystal structure with larger lattice constants; a = 5.5535 Å, b = 7.7669 Å, and c = 5.4910 Å.

Comparing LCFN-MP and LCFN-CP shows that the former pattern has shifted to a higher 2θ (Figure 3-2b). Peaks were similar to LCFN-CP, with no additional diffraction peak for secondary phases observed. The average crystalline size of LCFN-MP and LCFN-CP was determined at 333.0 Å and 236.8 Å, respectively. The larger crystallite size of LCFN-MP can be attributed to oxygen deficiencies in the lattice. In perovskites, oxygen loss and change in the oxidation state of B-site ions can occur, which are responsible for the mixed ionic and electronic conductivity of these materials at elevated temperatures [89].

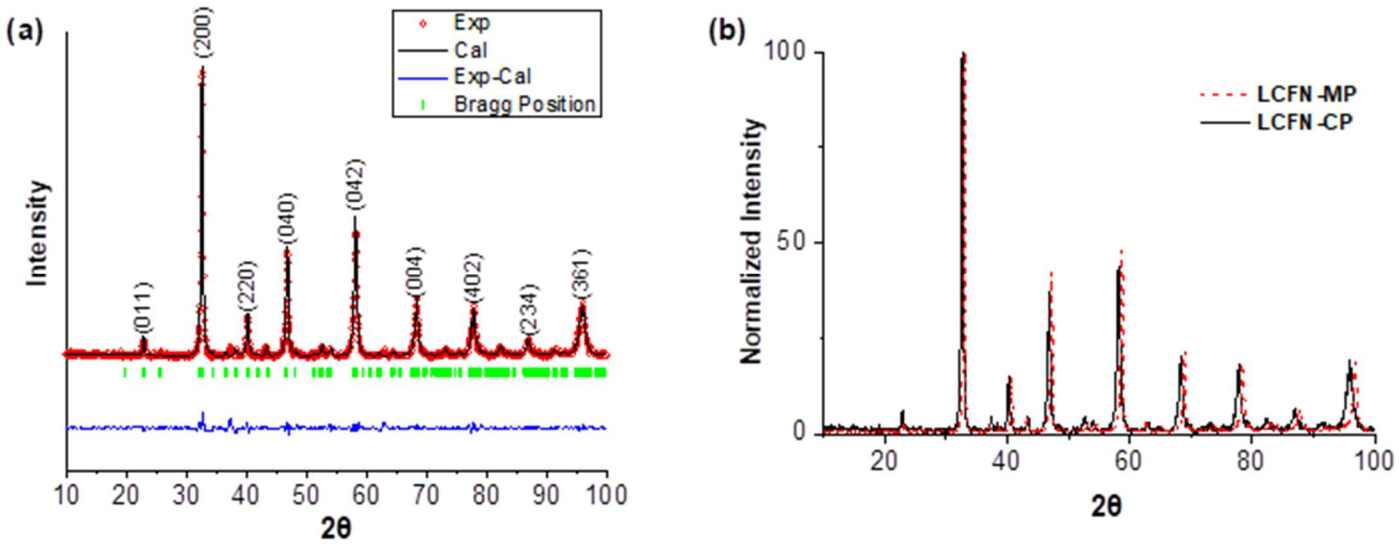

Figure 3-2 (a) Rietveld refinement of LCFN-MP (b) comparison of LCFN-MP and LCFN-CP powders.

In LCFN, oxygen vacancy formation is more favorable than the change in oxidation state of B-sites due to the strain induced by the larger size nickel at a higher oxidation state [90]. As the cooling rate is faster in the LCFN-MP sample, inferior lattice reoxidation can generate more oxygen vacancies than LCFN-CP [91]. In addition, as the microwave chamber is isolated and no extra flow of oxygen was provided, oxidation of nitrate precursors can provide an oxygen-deficient environment. To maintain charge neutrality, these oxygen deficiencies will lower the oxidation state of B-sites which has a higher radius. Additional heat treatment on LCFN-MP at 800 °C for 3 h in an electric furnace with air flow and XRD analysis (not shown) confirmed it. The observed shift in XRD results disappeared with similar crystal parameters now found between heat-treated LCFN-MP and LCFN-CP.

3.3.2 Electrochemical performance

Figure 3-3 shows I-V and I-P behavior of both cells. Due to our load and wiring limitation, current densities above 1500 mA/cm2 were not possible (the vertical line at the end of each measurement) to observe concentration polarization and possibly even higher maximum power output. Open circuit voltage (OCV) values for both cells confirm a dense and leak-free electrolyte as theoretical values suggested. LCFN-C showed the maximum performance of 697 mW/cm2 at 800 °C, while LCFN-M achieved close to 843 mW/cm2 under the same conditions, a 20.9% improvement in power output.

Nyquist plots of both cells under open-circuit conditions are shown in Figure 3-4a. The R0-(Q3-R3)-(Q2-R2)-G-W-(R1-Q1) equivalent circuit was used to fit the impedance spectrum similar to other works [92, 93]. R0 represents the overall ohmic loss; RQ3 and RQ2 show gas diffusion coupled with the charge transfer reaction and ionic transport within the anode functional layer.

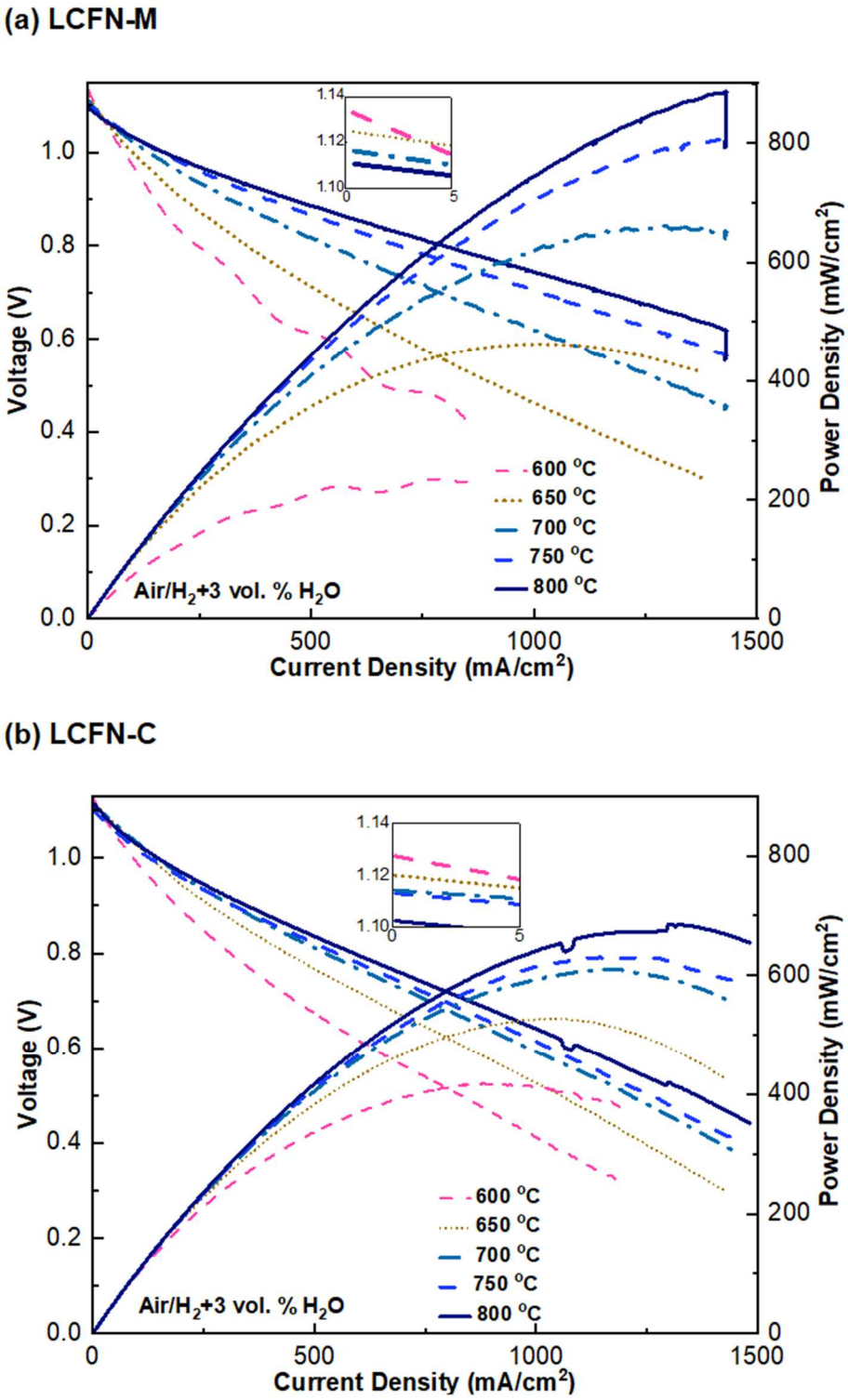

Figure 3-3 Electrochemical performance of cells as a function of temperature.

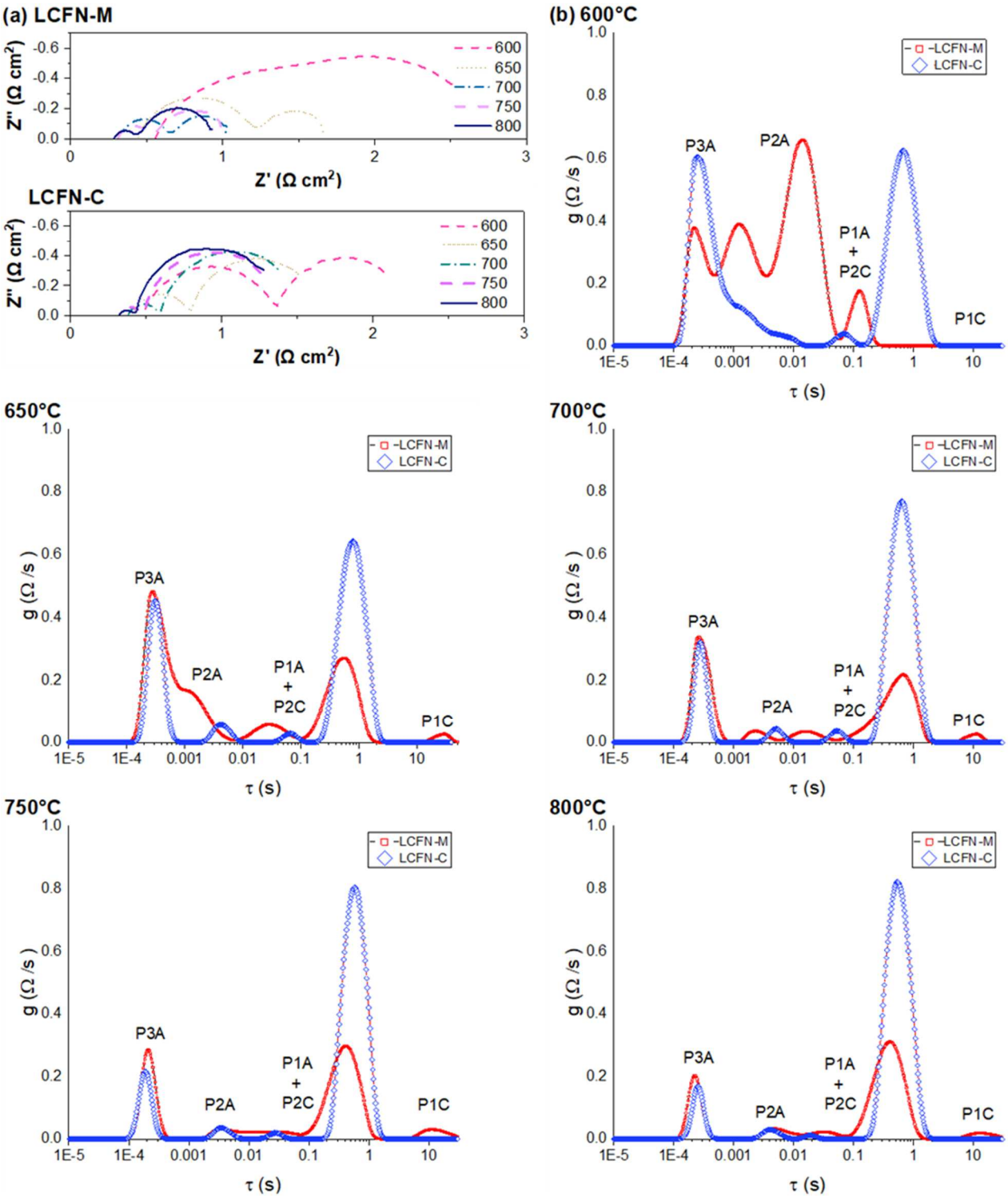

Figure 3-4 (a) Nyquist plots (not normalized) (b) calculated DRT of samples at different operating temperatures.

Similarly, RQ1 belongs to gas diffusion in the cathode structure. G is the Gerischer element that shows activation polarization at the cathode and W is a generalized finite length Warburg element accounting for diffusion losses in within the anode substrate. As expected, increasing the temperature reduces both ohmic and polarization contributions to the overall cell loss as most of the reactions involved are thermally activated. At 800 °C, both LCFN-M and LCFN-C show similar ohmic resistance, 0.29 $\Omega.cm^{2,}$ and 0.32 $\Omega.cm^2$, respectively, for the ohmic part thanks mainly to the very thin electrolyte and optimal design of the cell that will be explained in the microstructure section.

However, LCFN-M showed more than 35% lower overall polarization than LCFN-C with a total polarization of 0.65 $\Omega.cm^2$ which we can attribute to the improvement of the cathode in LCFN-M as both cells were almost identical in fabrication and testing. DRT response was calculated based on the measured impedance data and is shown in Figure 3-4b. We could distinguish five different processes labeled as shown. P1A is the gas diffusion polarization in Ni/YSZ support pores, modeled by a generalized finite-length Warburg element; P2A and P3A are attributed to gas diffusion coupled with the charge transfer reaction and ionic transport in the anode functional layer [92]. P1C is the diffusion polarization of the cathode, and P2C, which is a Gerischer element, is related to oxygen surface exchange kinetics and O^{2-} diffusivity in the bulk of the cathode. The area under each process corresponds to the total resistance of the respective process [94].

Both cells showed almost identical behavior for anodic processes, except at 600 °C, LCFN-M showed a rather large P2A peak. The reduction of nickel oxide in the support to metal will increase the porosity and thus enhance the gas diffusion of fuel through the anode. Since we reduce and test the cell at 600 °C and then go to higher temperatures, relatively high P1A and P2A could be due to an incomplete reduction process. Our gas injector is a simple tube that feeds the fuel at the end of the fuel cell. Due to variation in the placement of this tube, the complete reduction of both cells might not happen simultaneously. Also, imperfect current collector attachment, which is rolled mesh, may result in this discrepancy. However, P1A and P2A contributions become identical at higher temperatures in both cells. P3A is inversely temperature-dependent in the high-frequency region, as reported elsewhere [93].

P1C process showed a small peak in LCFN-M; we presume the finer particles with the higher cathode surface area make it harder for the oxidant to diffuse through. With the same impregnated weight load, the smaller LCFN-M particles inside the YSZ scaffold can impose more restraint on oxygen travel pathways than LCFN-C. As the gas diffusivity is directly related to the mean free path, this decrease in the mean free path will lead to a lower local effective diffusivity and increase the concentration polarization [95].

For both samples, P1A and P2C peaks overlapped over a wide range with much higher values for LCFN-M. Since both samples are made identically except for infiltration, we attribute this difference mainly to P2C. At 700 °C, LCFN-M showed the smallest value of P2C. We speculate as the highest electrical conductivity of

LCFN is around 700°C, the electrical conductivity of the cathode becomes the bottleneck for P2C [90].

P1A + P2C and P3A are rate-determining processes for both samples at lower temperatures. Above 700 °C, P2C becomes the major bottleneck for LCFN-C; for a thick porous MIEC, surface chemical exchange and oxygen diffusion dominate the impedance [92, 96]. LCFN-M showed a different behavior at higher temperatures; superior electrochemical performance of the cathode made P3A rate determining.

Oxygen molecules adsorbed on the surface of the cathode in the form of atoms and ions; these species then reach the electrolyte through different mechanisms, either on the surface or through the bulk. Smaller cathode particles with a higher surface area for LCFN-M compared to LCFN-C could justify this improvement as the cathodic polarization is proportional to the grain size [97]. This is also in line with our findings on the high value of P1C for LCFN-C. Similar works also confirmed the improvement of microwave samples in this regard [98-100].

3.3.3 Long-term degradation

Figure 3-5 shows a long-term run of the cell under load for about four days. The voltage was kept constant at 0.7 V, and the current was recorded vs. time at 700 °C after the initial tests.

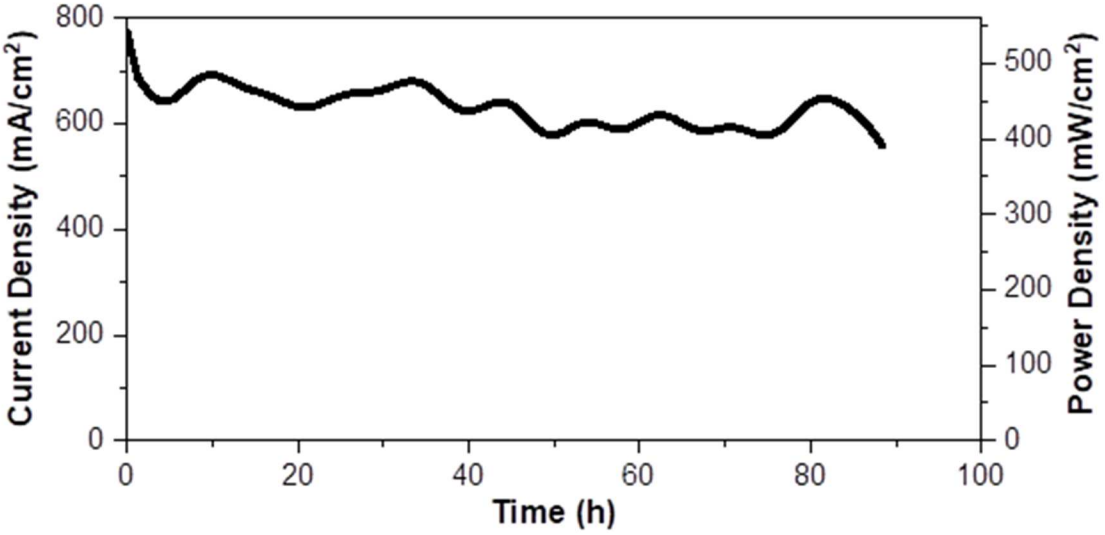

Figure 3-5 Long-term performance of a cell under load at 0.7 V at 700 °C.

This temperature was chosen to both have a reasonable power output and, at the same time, minimize degradation due to coarsening, which lowers the surface area of the active region near the electrode/electrolyte interface and thus decreases the performance.

Several factors contribute to the initial degradation in performance. Coarsening of the electrode, especially nano-size cathode particles, lowers the active area and decreases the oxygen reduction reaction (ORR) sites. Current collector attachment loosening due to the softening of metal at the high temperature can also contribute [65].

Figure 3-6a shows the impedance spectrum initially and at the end of the test with the calculated DRT shown in Figure 3-6b.

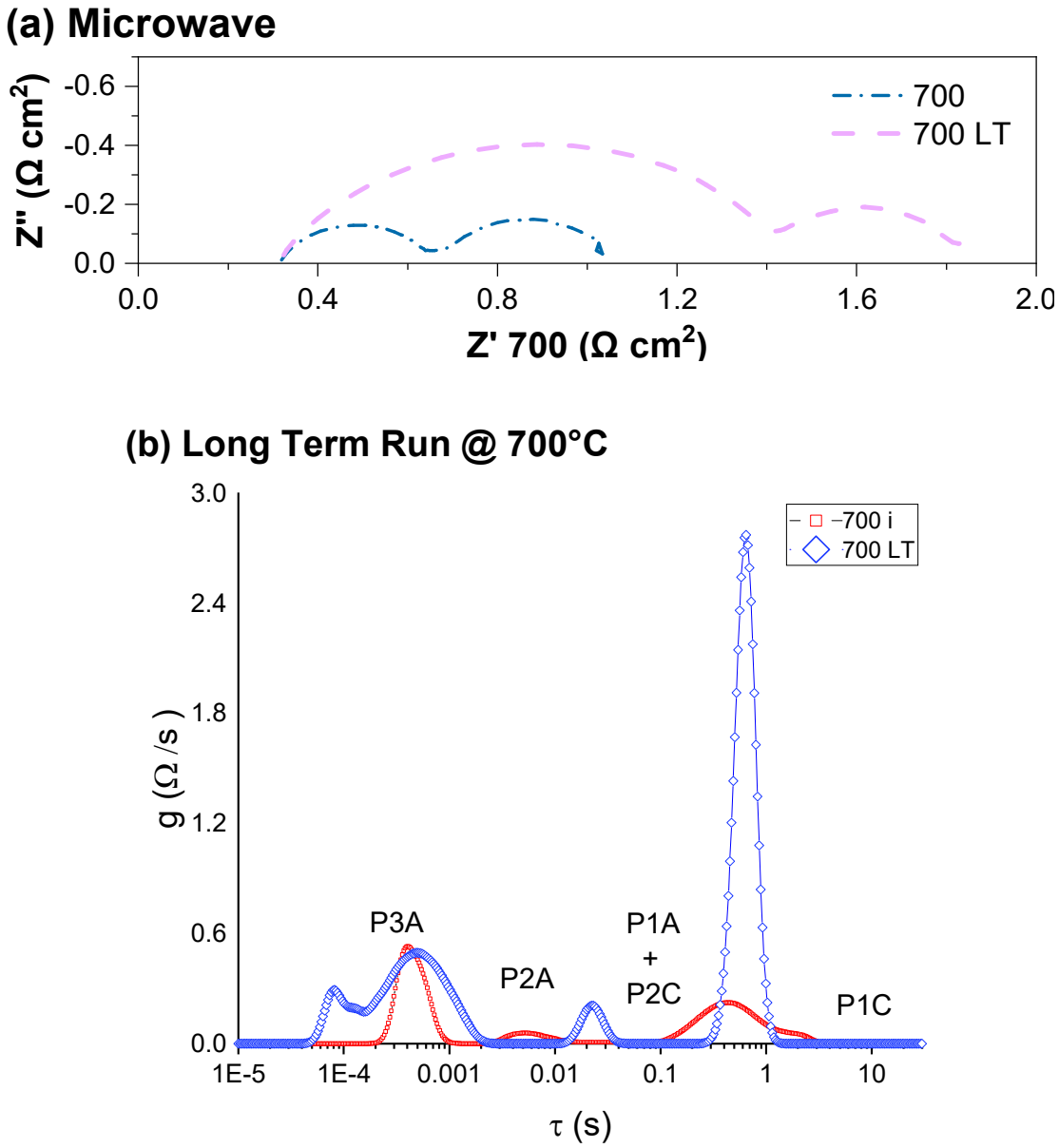

Figure 3-6 (a) Impedance (b) calculated DRT of the LCFN-M cell initially (700 i) and after the long-term run (700 LT).

Both polarization resistance at high frequency and ohmic resistance were the mechanisms for degradation of the cell. The ohmic contribution showed no change as we performed the initial heat treatment on the cell at 800 °C. The significant

polarization increase happened in P1A + P2C and P3A processes. Both infiltrated particles and nickel in the support start to coarsen, thus lowering the active area in the electrode/electrolyte active region.

As a result, it becomes harder for the fuel to diffuse through the support and reach the reaction area. The lower surface of nickel also reduces the active sites near the functional anode/electrolyte interface. The P2C process strongly depends on oxygen ion transfer from the MIEC to oxygen vacancies in the electrolyte [101]; thus, coarsening of cathode particles, especially in the TPB region, could lower the pathways from the cathode to electrolyte and hence increase the polarization [102].

3.3.4 Cathode particles and cell microstructure

LCFN-MP and LCFN-CP particles were annealed 3 h at 800 °C in the electric furnace for consistent comparison, and their micrographs are shown in Figure 3-7.

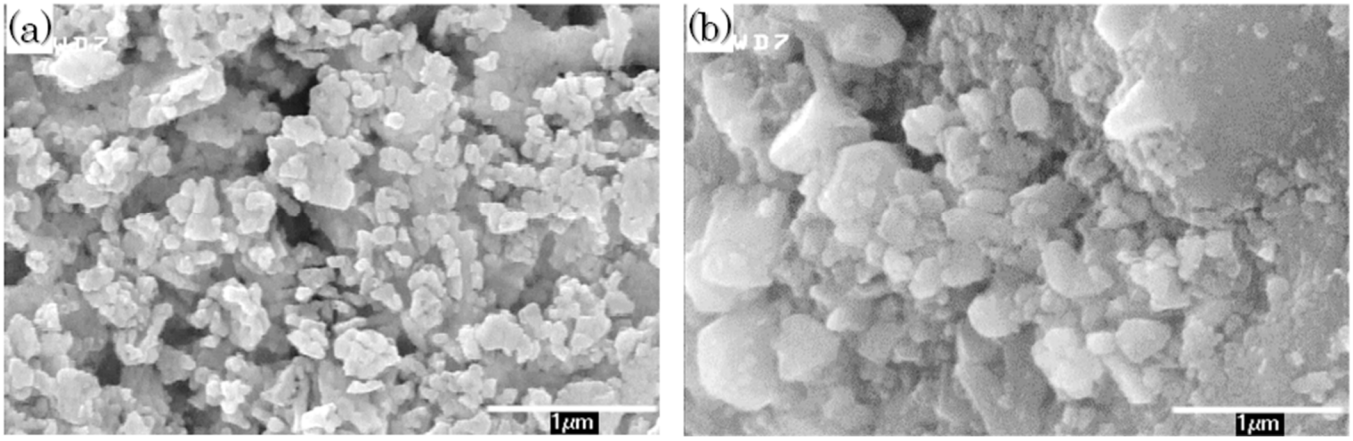

Figure 3-7 SEM micrographs showing (a) LCFN-MP (b) LCFN-CP particles.

LCFN-CP shows more tendency for agglomeration with a wide range of particle sizes; the average particle size was estimated to be 80 nm. By contrast, LCFN-MP shows much more uniformity and less tendency for agglomeration with an average size of 55 nm. We suspect the finer particle size of LCFN-MP is due to precursors' higher self-ignition temperature, which resulted in finer particles as the flame of LCFN-MP was more intense [103].

The cross-section micrograph of LCFN-M after testing is shown in Figure 3-8. The total thickness of the cell is estimated to be around 430 microns, with the TPL and electrolyte about 40 and 10 microns, respectively. Figure 3-8a shows the elongated pores that are signature of flake graphite as the pore former as previously observed [104], allowing the fuel to reach the functional layer more efficiently. Although we did not add any additional layer as AFL (anode functional layer), the porous nature of the support and the dip-coating technique seem to make a unique smooth transition from the support to the electrolyte with a denser layer near the electrolyte with a thickness of around 20 microns which could act as an AFL, and improve electrocatalytic activity and lower activation polarization [69]. Based on our experiments, including an additional AFL layer helps little as it increases the overall polarization and more severe fuel starvation that we suspect is due to the thickening of this layer that complicates charge transfer and diffusion-coupled charge transfer reactions in the AFL as reported elsewhere [105].

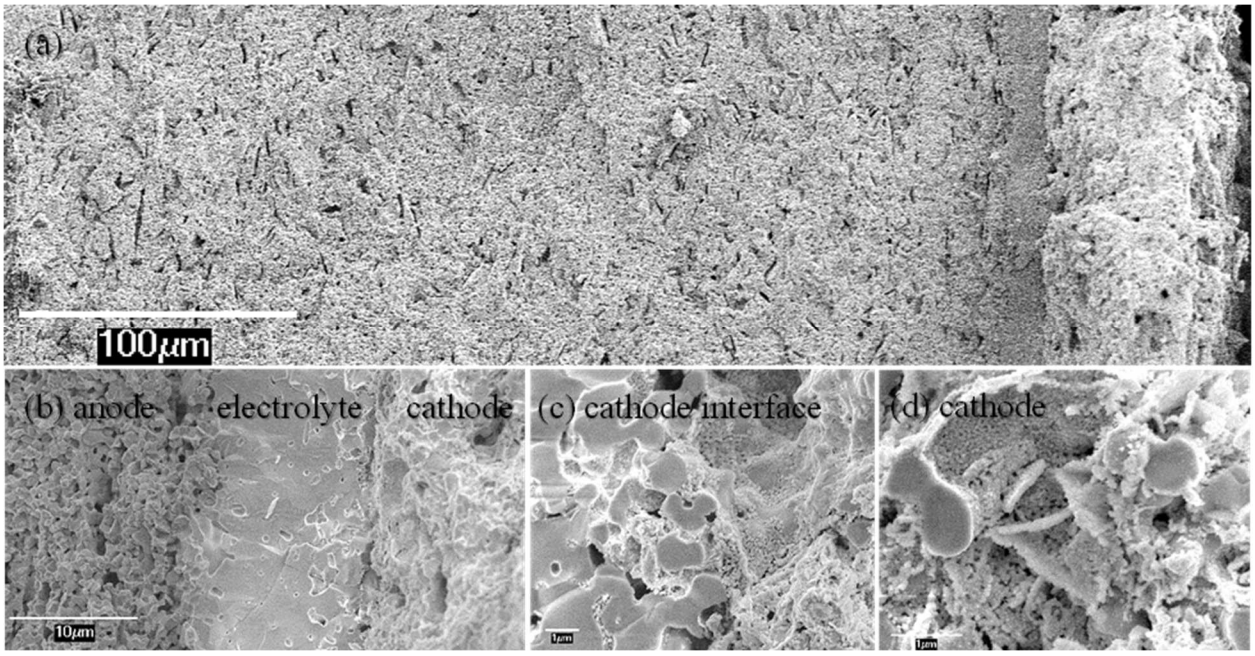

Figure 3-8 Cross-section view of (a) whole cell, (b) anode/electrolyte/cathode, (c) electrolyte/cathode interface, and (d) cathode after electrochemical testing.

The electrolyte in Figure 3-8b can be seen as fully dense, which was confirmed by a blue methane leakage test, with some closed pores that could improve mechanical properties of the electrolyte as they can prevent crack propagation and limit stress concentration which is essential as the electrolyte is the weakest part in anode supported SOFCs [106].

The infiltrated cathode, which can be seen in both Figure 3-8c and d and consists of a YSZ backbone matrix with connected nanoparticles of LCFN with high surface area, uniformly forms interconnected pathways for the reaction through to the electrolyte that can enhance performance and reduce degradation [72]. In this case, the dual role of YSZ can be seen as a scaffold and ionic pathways for ionic oxygen species.

Depending on the working temperature, LCFN can contribute as an electronic and ionic conductor with a volumetric active region rather than a purely electronic path to improve the ORR active sites. Even after a prolonged cell test at 700 °C, most LCFN particles still retain their nanoparticle sizes around 30 nm, well below the 100 nm threshold suggested for optimized electrochemical performance [107, 108].

As XRD results showed no significant difference between LCFN-MP and LCFN-CP final phases, we suspect performance improvement was mainly due to the morphology and distribution of infiltrated particles. With the higher rate of heating in LCFN-M, less grain coarsening becomes favorable, which can cause a significant improvement in surface area. The infiltrated particles combined with the YSZ backbone resulted in an optimized microstructure for the electrode, enhancing its performance.

Some agglomeration can be seen that could reduce the uniformity of the cathode and channelize the path for ORR, which might explain the increase in polarization and lower performance after the long-term test. This problem might be mitigated by repeating the infiltration and increasing the concentration of the infiltrated solution to have a higher yield after decomposition, as the initial results before the long-term run were excellent. Lowering the working temperature might be the most practical way to prevent coarsening and agglomeration of the cathode particles.

Therefore, the combination of wet impregnation and in-situ microwave heating is a very effective method to cut manufacturing processing time and produce an optimum microstructure to achieve optimum power performance without the need for a

complicated design or use of more costly materials to achieve similar performance. This technique could be implemented in other areas such as solid membrane reactors and heterogeneous catalysts, in which a high surface area catalyst is essential.

3.4 Conclusions

In this investigation, the infiltration of a porous scaffold using in-situ deposition with the help of microwave irradiation was studied. $La_{0.6}Ca_{0.4}Fe_{0.8}Ni_{0.2}O_3$ was used as the cathode because of its good electron and ion conductivity, chemical stability, and satisfactory catalytic activity. A second sample with the same parameters except a traditional electric furnace heat-treatment step after infiltration was prepared for comparison.

XRD analysis revealed that microwave irradiation resulted in a smaller crystalline size, attributed to an oxygen deficiency in the crystal. Heat treatment in an air atmosphere resulted in the same final phase for both samples. Measurement of performance vs. temperature was carried out. The best results were achieved at 800 °C with a maximum power density of 0.843 W/cm^2 for the microwaved sample, a 20.9% improvement compared to the electric furnace sample. Impedance and DRT analysis revealed much of the loss comes from cathode polarization which was lower in LCFN-M as cathodic polarization is proportional to grain size. A 90 h long-term run at 700 °C shows about 20% degradation that falls within our expectation as this mainly has to do with coarsening the nano-size cathode that might limit the pathway for the ORR, and nickel coarsening on the anode side.

SEM of powders revealed much more uniformity and less tendency for agglomeration of the microwaved cathode. Cross-section micrographs confirm both a leak-free electrolyte with a homogenous cathode spread over the TPL right to the electrolyte. The average cathode particle size in the TPL after the long-term test was estimated to be around 30 nm. Results showed that microwave heating leads to a smaller final size and more uniform distribution, enhancing the electrode's overall performance.

Chapter 4. Direct Microwave Sintering of Poorly Coupled Ceramics in Electrochemical Devices

4.1 Introduction

Unlike traditional sintering, where heat is transferred to objects by conduction, radiation and convection mechanisms, microwave irradiation (MI) provides rapid, economic, volumetric and uniform heating throughout the sample [109]. Since MI can achieve a higher heating rate and lower dwelling time at elevated temperatures, superior mechanical properties can be attained due to a lower tendency for coarsening and higher for sintering [110].

Indeed, microwave coupling is conditioned by the existence of strong dielectric relaxations which can be excited by the microwave beam, relaxation for an inorganic compound either to proton species (OH^-, H_2O, H_3O^+, etc.) or to conductive ions or at least locally mobile ions [111]. Eddy currents or magnetic induction play an essential role in heating high-conductivity materials such as metals [36]. The eddy currents induced in the conductor due to the interaction of the magnetic field produce a force that pushes the conducting electrons outward into a narrow area near the surface [37]. In the case of conductive powder compacts immersed in a relatively high-intensity electromagnetic field, other phenomena can occur, leading to a more pronounced and deeper heating of the conductive materials, like arcing and plasma formation [34]. Direct heating using MI in metals tends to be superficial;

consequently, the practical usage would be limited to starting powders with a particle size in the order of skin depth [112]; for 2.45 GHz, this would be in the order of microns.

Most ceramics such as alumina and zirconia are poorly coupled with MI at low temperatures with 900 MHz and 2.45 GHz frequencies. This dependence varies greatly depending on temperature and increases rapidly with increasing temperature, making microwave heating extremely difficult to control for these types of materials [34]. Thus, ceramic microwave heating is mainly assisted by a susceptor, a material with a high dielectric loss at room temperature, that transmits heat to the part being sintered mainly by radiation [113]. Since the demonstration of the possibility of sintering ceramics by microwave heating by Berteaud & Badot in 1976, many works have been published without the technique being used other than for drying or melting [114].

Unlike structural applications that utilize MI to sinter thin films with a dense substrate such as implants or industrial cutting tools, the support often needs to be porous in an electrochemical cell such as a fuel cell to allow fuel and oxidant to pass through. Several attempts have been made to incorporate MI in ceramic electrochemical cells, including using MI to synthesize precursor powders for each cell component and fabricate a whole cell, with improvements in densification, conductivity and performance compared to traditional heating being reported. Wang et al. used a one-step co-firing with a SiC susceptor for a proton-conducting solid oxide fuel cell (SOFC) based on barium cerate with more than a 50% increase in

performance over traditional heat treatment [115]. In another study, microwave heating resulted in finer particles near the anode interface but coarser near the cathode interface with overall improved performance resulting from the finer anode microstructure and the non-thermal effect of microwave sintering at the cathode [116]. Molero-Sanchez et al. used nitrate precursors and direct microwave heating to synthesize $La_{0.3}Ca_{0.7}Fe_{0.7}Cr_{0.3}O_{3-\delta}$ and then used a susceptor to fabricate a half-cell [117]. In all of the electrochemical cell fabrication research, susceptor-assisted microwave heating was used, making it challenging to incorporate in practice.

To successfully sinter poorly coupled ceramics, finding a way to efficiently increase microwave absorption at low temperatures without producing local hot spots is essential. One way is adding a small fraction of electrically conducting powders to the specimen that can increase microwave absorption of the body [118]; moreover, the oxide layer, which can form on the metallic powders due to oxidation, can contribute further [38]. This technique has been used for zirconia with the addition of SiC whiskers to enhance microwave absorption [119].

Finding a way to conduct susceptor-less microwave heating can lead to several advantages: as microwave energy absorption is divided between the susceptors, insulation, and sample, it can be more energy-efficient [120]. It also shortens the processing time as the specimen directly absorbs and dissipates the heat. On top of that, the whole MI setup becomes simpler, and cheaper to make.

In order to remove the need for a susceptor, preserving the metallic state of the substrate could be the key to incorporating direct microwave heating. By doing that,

the support acts as a built-in susceptor at low temperatures and can uniformly heat the entire sample.

It is possible that microwave-induced Joule heating is the driving force behind this heating process. The microwave's oscillating magnetic field can cause an induced current. As the magnetic field's oscillations change, the induced current will change direction[120]. As a result, the microwave energy converts to heat via Joule heating, resulting in quick and even volumetric heating. It has been demonstrated that moderate electronic conductivity is crucial for microwave absorption and rapid heating [121].

As the temperature of the support rises, direct coupling of MI and the ceramic portion of the cell in the support and electrolyte will follow. Since this process occurs in ambient air, the exothermic oxidation of the metal support and direct microwave absorption at elevated temperature provide the necessary energy to conduct the sintering process rapidly.

This study focuses on using direct microwave sintering on poorly microwave coupled ceramics without the use of any susceptor. To fabricate the electrochemical cell, Ni-YSZ cermet support is used as the substrate. YSZ was chosen as an electrolyte that has wide applications as a solid electrolyte yet poorly interacts with microwaves below 600 °C [122]; the electrolyte was sintered directly on top of the anode-support without the need of a susceptor. Tubular geometry was chosen as it has better resistance toward thermal shock [29]. For better comparison to conventional electric furnace heating, MI only was used for the electrolyte sintering. To the best of the

authors' knowledge, this is the first report on the direct use of MI on a poorly microwave coupled oxide that is being used in an electrochemical cell.

4.2 Experimental

4.2.1 Support fabrication

For the support, YSZ (Tosoh TZ-8Y) and NiO (Aldrich, <50 nm particle size) with a 35:65 weight ratio were mechanically milled for 24 h in an aqueous medium. 30 vol. % graphite (Sigma Aldrich <325 mesh) was added to the mixture. Slip casting in a plaster mold was used to fabricate the support which was pre-sintered at 1000 °C for 3 h. In the case of the microwave sample, the cermet support was reduced in an electric tube furnace at 750 °C for 3 h under a flow of 20 vol.% hydrogen in nitrogen.

4.2.2 Electrolyte coating

The coating slurry consisting of a mixture of as-received 8YSZ (Tosoh TZ-8Y), ethanol and binder (6 wt % ethyl cellulose in terpineol) was ball-milled for 24 h followed by ultrasonication to obtain a homogeneous suspension. Three rounds of dip coating were performed with 15 min intervals for drying at room temperature in ambient air.

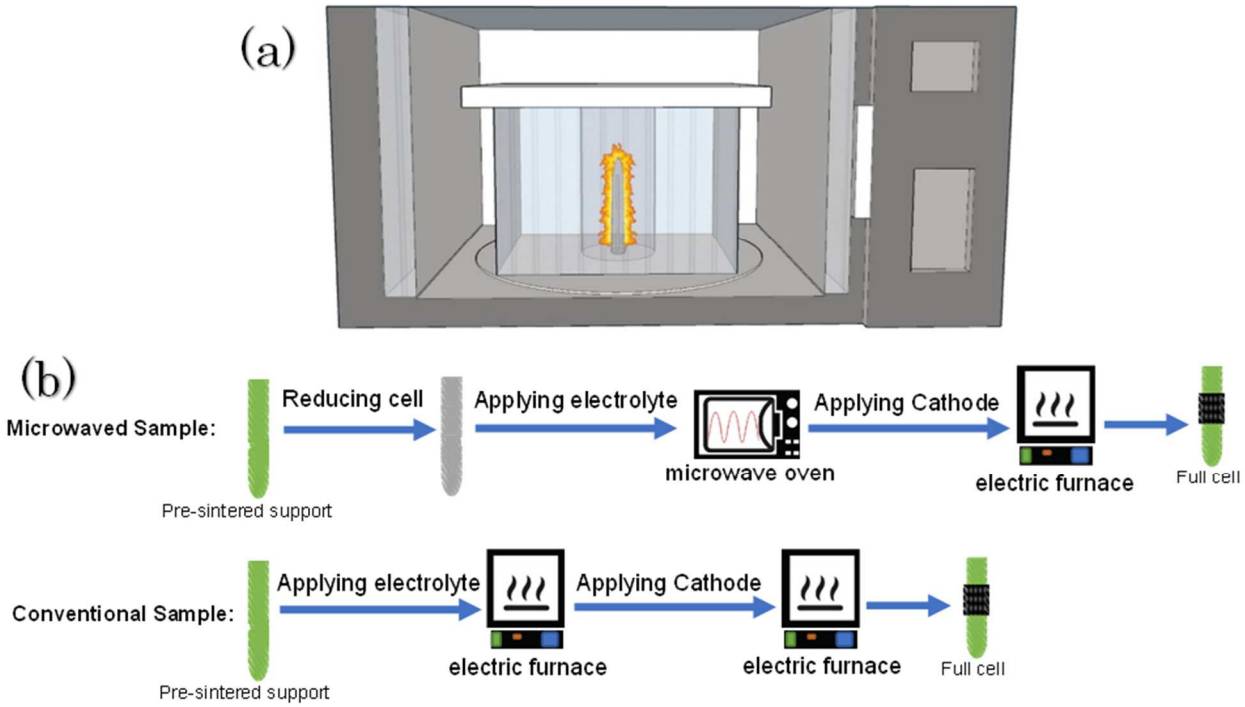

Figure 4-1 (a) Schematic of the sample inside microwave chamber with insulator (b) Schematics of sample preparation.

For microwave sintering, the microwave furnace used in this study was a modified household microwave oven (Panasonic NN-CD989S) shown schematically in Figure 4-1 (a). Power was supplied by a 1.1-kW continuously variable 2.45-GHz microwave generator with power settings manually controlled. The microwave cavity was surrounded by alumina fiber (C4501, Zircar Inc.) to prevent the magnetron and surroundings from heating up and from thermal shock. The sample was placed inside a three-piece custom-made cylindrical alumina fiber insulator to preserve the generated heat and prevent thermal shock. Zirconia felt (ZYF-100, Zircar Inc.) was used as the inner separator to prevent contamination. A type R thermocouple inside an alumina shell was placed underneath the sample to record the temperature. Methylene blue dye leakage tests were performed after microwave sintering to ensure

leak-free electrolytes. For the conventional sample, sintering was conducted at 1400°C for 3 h in air using an electric furnace to have a leak-free electrolyte.

4.2.3 Full cell fabrication

A mixture of $La_{0.6}Sr_{0.4}Co_{0.2}Fe_{0.8}O_3$ (LSCF, Fuel Cell Materials), azeotrope solvent, binder (polyvinyl butyral) and Menhaden fish oil as the dispersant was used for the cathode ink. The resulting mixture was dip-coated on top of the electrolyte, then sintered at 800 °C for 3 h. Gold paste and wires and copper mesh and wires were used for the cathode and anode lead connections, respectively. Figure 4-1 (b) shows the fabrication steps for both samples.

4.2.4 Electrochemical characterization

An electronic load and scanner (Agilent model N3301 and E4970A) measured the current-voltage curves. A Solartron 1255 frequency response analyzer and Solartron 1287 electrochemical interface were used for electrochemical impedance spectroscopy (EIS) measurements. The frequency range was between 0.01Hz - 1MHz, with 12 points per decade under open-circuit conditions. The data were recorded with 50 °C intervals in a temperature range of 600 °C – 750 °C using H_2+3vol.% H_2O as fuel feed and air as the oxidant.

4.2.5 Microstructure characterization

The morphological features of fracture cross-section of cells were examined by scanning electron microscopy (Zeiss Sigma 300 field-emission scanning electron microscope). The relative density is calculated by bulk density divided by theoretical density. The open porosity of the sintered samples was measured by Archimedes' method using water as the suspending fluid. The average of three sets of samples was taken.

4.3 Results and discussion

4.3.1 Microwave sintering

Several attempts with different MI powers and dwelling time were made to sinter a crack-free electrolyte. Some of the failed attempts can be seen in Figure 4-2 (a).

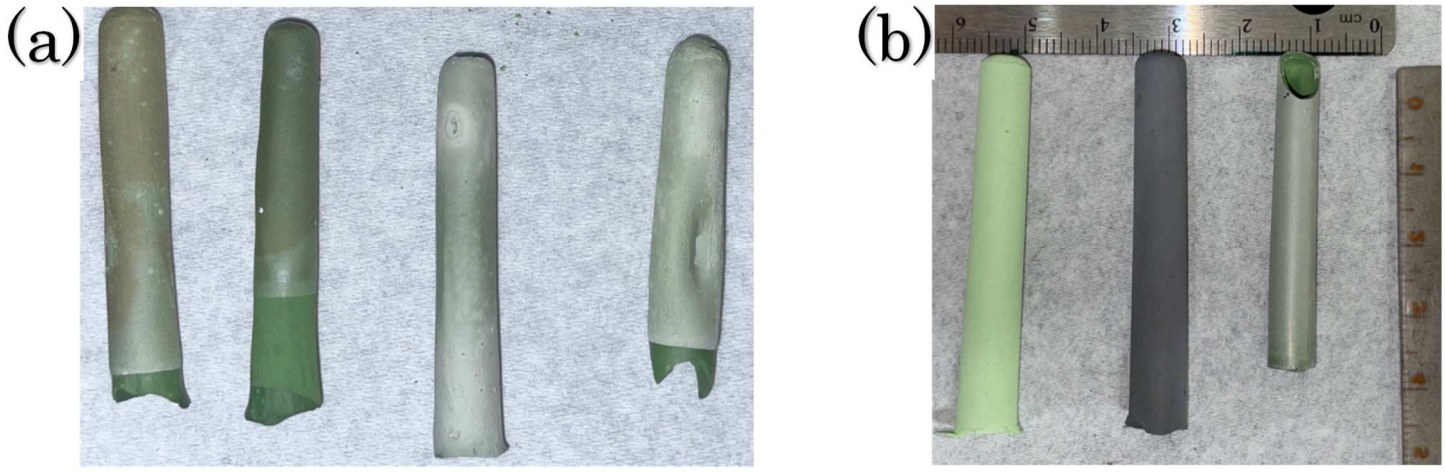

Figure 4-2 (a) Some defective samples during microwave sintering (b) (left) pre-sintered support, (middle) reduced pre-sintered support, (right) after electrolyte sintering using MI.

These include local deformations and inconsistency in the support due to the formation of hotspots during sintering, which compromise cell integrity. During MI heating, inherent temperature gradients may result in severe temperature nonuniformities and cracking of processed materials [123]. Several adjustments on power rate, timing, sample position, holder and insulators were made. Janney et al. found that uniform heating is the key to preventing the local thermal hot spots [122]. Initially, the oven's convection feature pre-heated the inner chamber to 190 °C. Although even at room temperature MI can be started, this will lower the thermal runaways for further steps. After 10 min, MI at 30% of power was applied for 10 min. Followed by 5 min, the power was set at 70% to maintain the temperature reached and conduct the sintering step, and 5 min at 10% for the last step to mitigate thermal shock. Figure 4-3 shows the temperature profile of the sample during sintering.

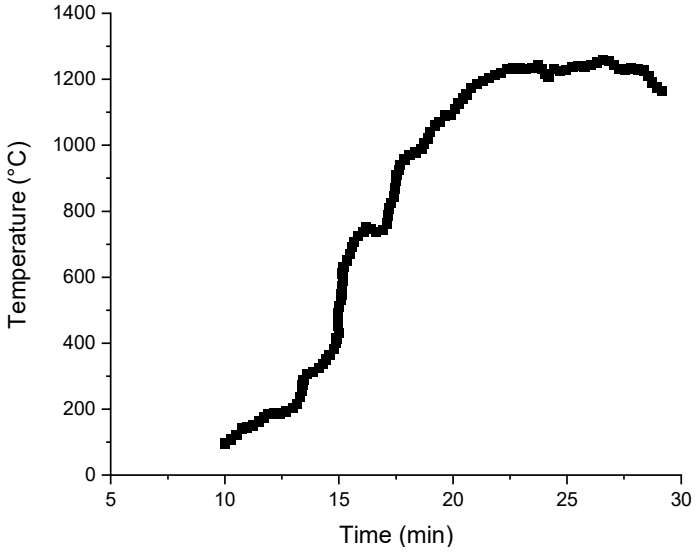

Figure 4-3 Temperature measurement vs. time.

Initially, it slowly started to increase. This part was due to the direct interaction of the metal portion in the support with MI; for nickel, eddy current loss, hysteresis loss and residual loss contribute to heating [42]. Above 500 °C, the exothermic reaction of nickel oxidation also increases the heating rate [124]. Over 600 °C, YSZ microwave coupling dramatically increases with the formation of intrinsic defects, leading to direct heating of the entire sample [31].

Figure 4-2 (b) shows the Ni-YSZ support before and after the electrolyte sintering using this method. In many instances, the top portion of cells cracked and separated during sintering as we suspect the top portion experienced the highest thermal shock and temperature gradient; yet this did not affect the integrity of the electrolyte. As the starting phase of nickel in the support was in oxide form and then reduced to nickel, we suspect the empty space due to this shrinkage provides enough space for the expansion of nickel to nickel oxide during microwave heating, and thus nickel inherently can have a negligible contribution to building up stress and cracking the sample. Final microwave cells had higher total shrinkage on average compared to the conventional sample as listed in Table 4-1; Matsuda et al. found that shrinkage needs to be more than 20% to form a dense YSZ film using susceptor-assisted microwave sintering [125].

Table 4-1 Comparison of samples between microwave and conventionally made cells

Sample	Compositions	Shrinkage During Electrolyte Sintering (%)	Active Area (cm^2)	Raw Porosity (%)	Final Porosity (%)
Microwave	35% YSZ, 65% NiO	21	1.88	8.6	28.6
Conventional	35% YSZ, 65% NiO	17	1.92	14.4	38.0

4.3.2 Electrochemical performance

Figure 4-4 (a) and (b) show the I–V and power density output curves of microwaved and conventional cells measured under air/H_2+3vol.% H_2O. At lower temperature, the power performance of both cells is very comparable. At higher temperatures, conventional cells have a slight advantage.

At higher currents of microwaved samples, the end of the curves which result from concentration polarization and fuel starvation becomes more significant and deviates from ohmic behavior of the conventional cell which resulted in lower performance for the microwaved sample.

OCV results of both cells are close to theoretical values based on the Nernst equation, suggesting a dense electrolyte that prevents direct charge transfer or gas permeability and successful microwave sintering. OCV of the microwaved sample was slightly higher than the conventional sample, which might be due to better densification of the electrolyte, as reported in a similar study [126].

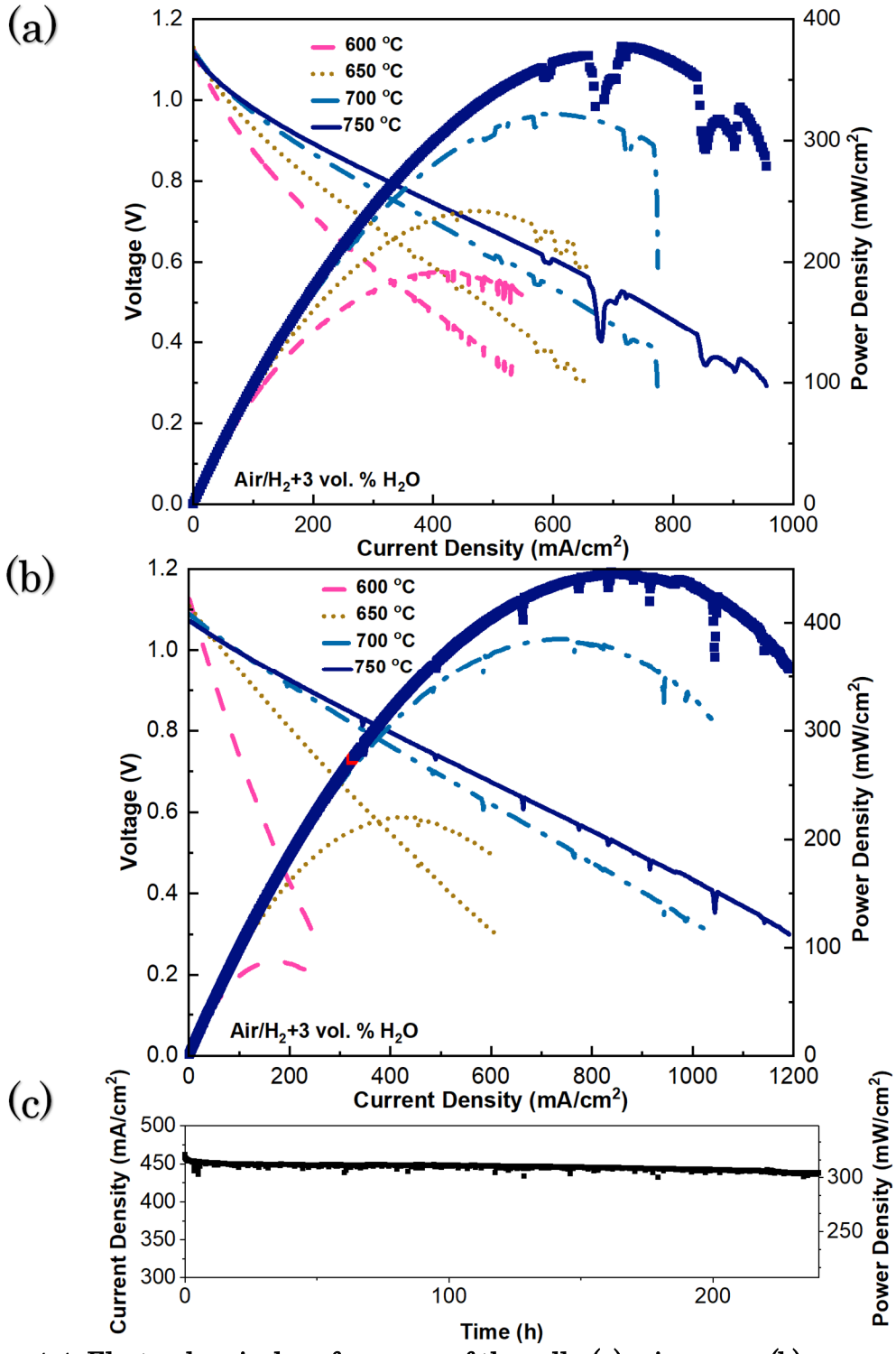

Figure 4-4. Electrochemical performance of the cell , (a) microwave (b) conventional.

(c) long-term stability

Figure 4-4 (c) shows the long-term run of the microwaved sample under load for seven consecutive days. The voltage is kept constant at 0.7 V for this test, and the current is recorded over time. Some slight variations were observed mainly due to imperfect current collector attachment, especially at the anode side and coarsening of the electrode particles [85]. No excessive degradation in the performance was observed for the microwaved sample.

In Figure 4-5, the far-right polarization that is temperature independent belongs to mass transfer occurring at the electrodes with $\omega_{\max} = 8\ Hz$ [127]. In agreement with I-V performance of both cells, concentration polarization of the microwaved sample is relatively large compared to our conventionally prepared cells with the same cathode. As the support experiences relatively high temperatures compared to the electric furnace, it undergoes more rapid aggregation that reduces the overall porosity making it more difficult for the fuel and steam to pass through. The ohmic part of the impedance correlates to the electrolyte and the connections. For the microwaved sample it shows a slight improvement; we suspect this might be due to better crystallization of the electrolyte due to the higher sintering temperature or it might be just slight variations among samples.

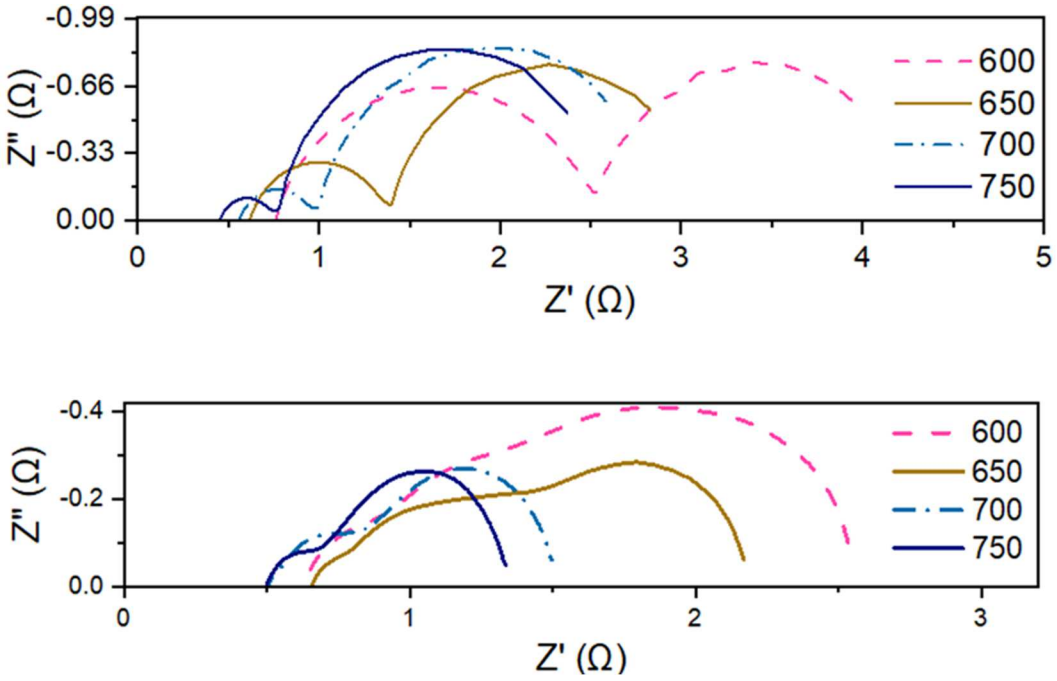

Figure 4-5 Nyquist plots (not normalized) of cell at different operating temperatures. (top) microwave (bottom) conventional

4.3.3 Cell microstructure

Figure 4-6 shows the cross-section micrograph of both cells after electrochemical characterization. The distinctive longitudinal porosity which developed during conventional heating cannot be seen here. Instead, the support consisted of several big chunks with very little porosity inside and large vacancies around them. This swallowing behavior of MI to form a more prominent grain was also seen in an Al-SiC cermet [128]. These non-uniformities might be attributed to liquid phase formation during microwave sintering of nickel powder [129].

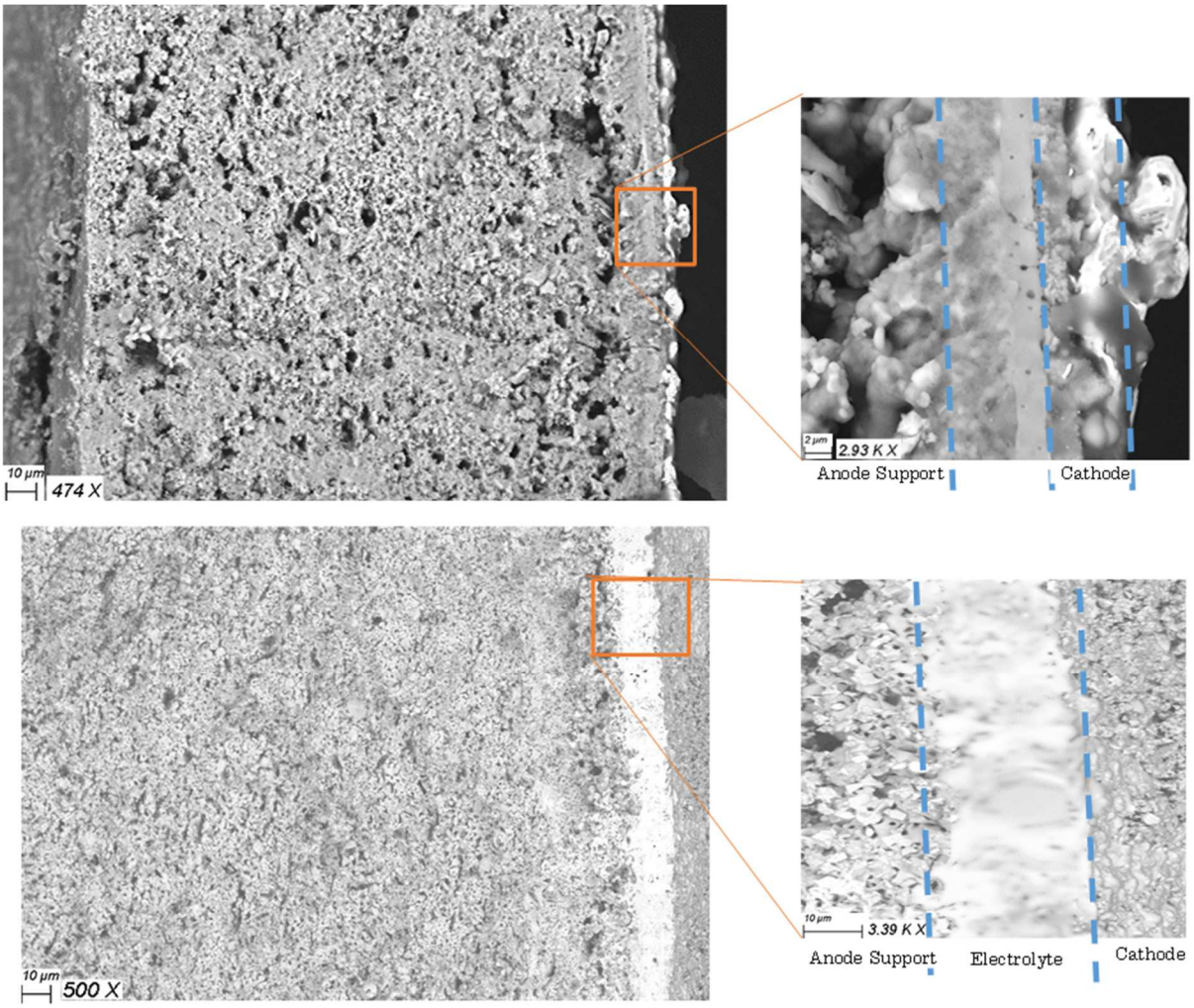

Figure 4-6 SEM images of cross-sections of (top) microwave (bottom) conventional samples

The electrolyte region consisted of two unique features. The inner part (left side) consisted of almost melted particles of nickel and YSZ sintered together, and the outer side (right side) forms a very dense layer with a small number of closed pores. The combination of exothermic oxidation of nickel and microwave coupling can locally raise the temperature to melt nickel, explaining this phenomenon [123]. Also, arcing and localized melting can occur as the local concentrations of electric field exceed the dielectric strength of the air inside [79].

Table 4-1 shows the measured open porosity of both microwaved and conventionally prepared supports. Raw porosity indicates the open porosity after sintering and final is the open porosity after reducing the support to a cermet. The microwave sample shows lower porosity compared to the conventionally prepared sample. The microstructural findings are in line with the overall electrochemical behavior of the full microwaved cell with a large concentration polarization bottleneck. This can be mitigated by additional optimization to preserve the open porosity during MI sintering, such as pre-coarsening the starting powder and increasing the pore-former content in the support. Since there is a limitation on the particle size of the metal to have non-superficial interaction with MI, this leaves the ceramic part of the support as the only viable part to be adjusted.

Geometry and composition uniformity of the support are essential to prevent thermal runaways. Extrusion would be a suitable method to maintain these properties for the substrate. In addition, with nickel metal powder and YSZ as the starting powder of the support, direct microwave sintering implementation can become much simpler and faster. The green body resulting from extrusion can be directly coated with ceramic electrolyte and sintered in one step in a microwave chamber with no pre-sintering or reduction necessary making it cheaper and faster compared to the conventional sintering process using an electric furnace. The cathode cannot be incorporated into this scheme as the high temperature of the sintering process promotes insulating phase formation such as lanthanum zirconate as a secondary phase, lowering the overall performance.

This study has some limitations. First is the lack of automation; for an ideal setup, a feedback loop system with direct temperature control of heating using thermometer and power regulation software of microwave output would be necessary, which enable a more precise sintering temperature and more uniform heating. The second limitation was using a household microwave oven. Although it provided a proof of concept, it was not optimized for high-temperature sintering; the non-uniform distribution of microwave irradiation, temperature and insulation were problematic. The lack of a susceptor in this process could make it ideal for practical applications as it would increase efficiency and decrease the processing time and the use of expensive setups. This process can easily be used for other similar devices that have (a) a portion of the support that can be reduced to metal form (b) poorly coupled coating material: heterogeneous catalysts, ceramic electrochemical cells and solid state batteries are some examples. Proton conductor oxides can be a great use case as they usually need higher sintering temperatures and thus expensive furnaces compared to oxygen conductor counterparts; especially barium zirconate needs sintering temperatures exceeding 1600°C for a leak-free electrolyte [85]. Compared to previous results, we have a much simpler fabrication process that is faster and more cost-effective with a comparable power density [130].

4.4 Conclusions

In this study, we focused on a new method based on partial reduction of the substrate to enable the direct microwave sintering of a poorly coupled top layer without the need for any susceptor. The metal phase in the substrate can directly absorb the irradiation and increase the temperature of the whole sample, enabling direct microwave heating. The heat resulted in microwave interaction which along with substrate oxidation can then sinter the sample without a susceptor. The lack of a susceptor would increase the efficiency and decrease the complication of the system and processing time, making it ideal for practical applications. A solid oxide electrochemical cell was used as an example; YSZ electrolyte was coated on top of a Ni-YSZ support, and microwave sintering was used to sinter the half-cell. YSZ is poorly coupled with microwave irradiation, but we managed to sinter without any susceptor with this technique. The leakage test and full-cell power measurement results revealed a fully leak-free electrolyte. A similar sample using the conventional electric furnace was tested and compared.

The cell shows electrochemical performance comparable to traditional sintering techniques; some fuel starvation at high current was seen due to non-optimized microstructure of the support. Scanning electron microscopy was used to study the cross-section of the cell. It shows a distinct swallowed microstructure compared to the needle shape of conventional heat-treated samples. Density measurements also confirm lower open porosity of microwave prepared samples compared to traditional heating. In the end, we found this direct microwave irradiation technique very promising. Although the technique cannot be incorporated in all applications due to

its requirements, it can be used extensively in heterogeneous catalysts and ceramic electrochemical cells such as solid oxide fuel cells and solid state batteries.

Chapter 5. Electroreduction of Titanium Oxide to Titanium Nitride Using Solid Oxide Electrolyte

5.1 Introduction

This chapeter will discuss the use of titanium nitride as an electrode in solid oxide fuel cells. This was conducted through an electroreduction of the titanium oxide and the formation of titanium nitride in the presence of nitrogen. First, a brief introduction to titanium and titanium nitride will be given. Then the progress that led to the selection of titanium nitride will be examined. The experiment, discussions, and conclusion will follow.

5.1.1 Titanium production

Titanium is one the most valuable metals available due to its distinctive characteristics; it has the highest strength-to-density ratio of any metal. Its corrosion resistance makes it very useful for highly corrosive environments such as high temperatures, the presence of halides, and aerospace industries.

The primary method for commercial production of titanium metal is the Kroll process. In this pyrometallurgical process, titanium chloride is reduced by liquid magnesium to produce titanium metal, as shown in the equation (1-13).

$$TiCl_4 + 2Mg \xrightarrow{825^\circ C} Ti + 2MgCl_2 \qquad (1\text{-}13)$$

The process is conducted in a stainless steel retort at 800–850 °C, as shown in Figure 5-1. The magnesium chloride will be refined back to magnesium.

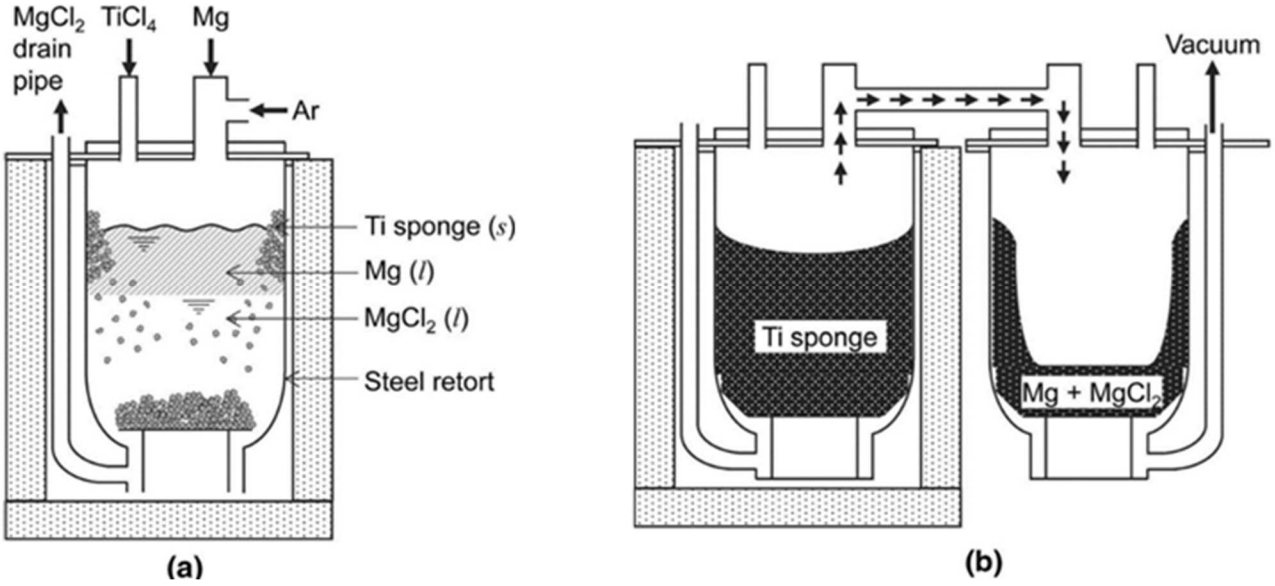

Figure 5-1 —Schematic illustration of the reaction system in the Kroll (a) Magnesiothermic reduction of $TiCl_4$. (b) Removal of Mg and $MgCl_2$ from titanium sponge by vacuum distillation[131].

The sponge titanium will be purified by additional vacuum distillation or a leaching process. The resulting sponge is then crushed, pressed, and melted in a consumable carbon electrode vacuum arc furnace and solidified under vacuum. A further remelting step can be conducted to remove any possible unwanted phases and ensure uniformity. These steps increase the cost of the product, resulting in it being six times as expensive as stainless steel, although titanium oxide is abundant and inexpensive[132]. Other disadvantages of the Kroll process include extensive raw material preparation and by-products that require proper disposal as they are hazardous[133].

Titanium chloride required for the Kroll process comes from the reaction of rutile ore in a fluidized bed furnace with chlorine gas in the presence of coke at approximately 1300 K using the reaction shown in the equation (1-14).

$$TiO_2(s) + 2Cl_2(g) + C(s) \rightarrow TiCl_4(g) + CO_2(g) \quad (1\text{-}14)$$

Several attempts have been made to use electrochemical reduction rather than a pyrometallurgical process similar to aluminum's Hall–Héroult process to lower costs and make the final product more environmentally friendly.

In recent years, FFC (Fray-Farthing-Chen) and OS (Ono-Suzuki) processes have become more popular for directly reducing TiO_2 than others. In these approaches, TiO_2 powder in the vicinity of a cathode is immersed in molten $CaCl_2$ and electrolyzed to produce titanium metal. One major drawback of this method is the need to control the atmosphere during the electrolytic reduction, which was insufficient. Therefore, the purity of the yielded titanium was low [131].

5.1.2 Titanium nitride

Titanium nitride is a refractory material with high hardness, high corrosion resistance, and chemical and thermal stability. Titanium nitride applications include special refractories and cermets, crucibles for casting metals in the absence of free O_2 in the environment, non-toxic exterior for medical implants, and a wear-resistant and decorative "gold-like" coating[134]. The coating can be used on titanium alloys, steel, carbide, and aluminum to enhance the materials' surface properties. Most titanium

nitride applications are based on thin films formed by sputtering, physical vapor deposition (PVD) evaporation, chemical vapor deposition (CVD), and ion plating.

5.1.3 TiN Sintering

Few studies have been reported on the synthesis of bulk TiN samples. Synthesis of bulk TiN ceramic is extremely difficult to conduct because of its high melting point, low self-diffusion coefficient, strong covalent bonding and high oxygen affinity, and is often done by hot isostatic pressing (HIP) with the sintering temperature exceeding 1700 °C and pressures more than 30 MPa [135].

Because of large porosity, covalent bonding, surface oxide impurity, and poor self-diffusion coefficient, it is challenging to sinter a completely dense TiN ceramic, resulting in poor fracture toughness. The processing that has been used to sinter TiN includes laser cladding, explosive synthesis, reactive milling, and layers of atomic deposition with combustion synthesis[136].

Sintering aids such as hydrides (TiH_2), carbides (TiC, WC, HfC), oxides (SiO_X), transition metals (Co, Ni, Mo), nitrides (AlN, BN, Si_3N_4), and diborides (TiB_2) have been used in TiN to enhance the densification with success but alters the TiN properties in many cases[137].

5.1.4 TiN and solid oxide fuel cell

Titanium nitride would be an interesting choice to be used in solid oxide cells as an anode. Some of the characteristics of TiN include,

- Melting point: 2930 °C
- Oxidation starts form 800 °C
- Thermal expansion: 9.35×10^{-6} /°C
- Electrical conductivity: 25 μΩ·cm

There are many advantages to using the TiN in the electrode; the very high melting temperature prevents the growth of grains during SOFC operation, preserving its porosity and microstructure, something that metal phases such as nickel and copper suffer from [138]. The thermal expansion is very close to cubic YSZ8 (10.5×10^{-6} /°C), preventing cracks from forming and poor adhesion during heating and cooling and ensuring thermal shock resistance, something that nickel suffers (13.3×10^{-6} /°C). Electrical conductivity is another vital aspect of the electrode, guaranteeing minimal ohmic loss for the cell, and TiN has excellent electrical conductivity. The electrode material should have a conductivity greater than 1 S/cm in order to be practical since a conductivity of 1 S/cm would lead to a cell resistance of 0.1 Ω cm^2 for an electrode thickness of 1 mm [139].

On top of the mentioned properties, the oxidation resistance can help the cell stability in case of any leakage in the system, especially in the anode, which could lead to catastrophic failure. It has been shown that TiN shows good catalytic activity toward methanol oxidation, ethanol oxidation, formic acid oxidation, and oxygen reduction [140]. The oxygen reduction reaction is the most sluggish in the cell; lowering the working temperature TiN might be able to be used as the cathode in the fuel cell. Despite these reports, in many studies, TiN was either a thin film or was accompanied

by another material such as Pt, so more studies are necessary to assess the bulk TiN catalytic activity, which is out of the scope of this study. The catalytic activity of TiN might be enhanced by adding secondary phases such as nickel, ceria, or other active materials in case of insufficient catalytic activity.

One significant advantage of TiN is that it does not suffer from coke formation, which nickel is known for and hinders the usage of direct hydrocarbons as it significantly shortens the cell's life cycle.

TiN can be used as the interconnect, replacing chromium-based lanthanides or high chromium alloys such as 718 SS, 302 SS, 430 Ti SS, 439 SS, Haynes 230 and Crofer 22, which could poison the cell due to chromium migration during cell operation[141]. This study uses an electrode-supported solid oxide electrolyte cell to electrochemically reduce the titanium oxide to titanium nitride in the presence of nitrogen. YSZ acts as the electrolyte, and graphite was used as the counter.

5.2 Experimental

5.2.1 Support fabrication

For the support, as-received TiO_2 (98.0-100.5% TiO_2, Thermo Scientific) was mechanically milled for 24 h in an aqueous medium with a weight ratio of 1:1. 30 vol. % graphite (Sigma Aldrich <325 mesh) was added to the mixture, followed by pH adjustment using HCl to 3.0 to improve the stability of the suspension. Slip casting in a plaster mold was used to fabricate the support, which then pre-sintered at 1000 °C for 3 h.

5.2.2 Buffer layer coating

To prevent electrolyte delamination which will be explained later, a coating slurry consisting of a mixture of 1:1 of as-received yttrium(III) oxide (99.9%, Thermo Scientific), 8YSZ (Tosoh TZ-8Y), ethanol and binder (6 wt % ethyl cellulose in terpineol) was ball-milled for 24 h followed by ultrasonication to obtain a homogeneous suspension. Two rounds of dip coating were performed at 15 min intervals followed by drying at room temperature in ambient air. Sintering was conducted at 1400°C for 3 h.

5.2.3 Electrolyte coating

The coating slurry consisting of a mixture of as-received 8YSZ (Tosoh TZ-8Y), ethanol, and binder (6 wt % ethyl cellulose in terpineol) was ball-milled for 24 h, followed by ultrasonication to obtain a homogeneous suspension. Three rounds of dip coating were performed at 15 min intervals prior to drying at room temperature in ambient air. Sintering was conducted at 1450°C for 3 h in air using an electric furnace to have a leak-free electrolyte.

5.2.4 Cell fabrication

Graphite conductive adhesive (Thermo Scientific) was used as the counter on top of the electrolyte. The paste was applied using a brush and dried at room temperature.

Nickel mesh and wires and graphite foil and wires were used for the cathode and anode lead connections, respectively.

5.2.5 Phase characterization

XRD patterns of samples were recorded at room temperature using a Rigaku Ultima IV diffractometer with Co-Kα radiation. The scan conditions were 38 kV and 38 mA, and data were collected over the angular range of $10° \leq 2\theta \leq 75°$ with a step size of 0.02° and a scan speed of 2 deg/min. The phase identification was conducted using Match! Software (Version 3, Crystal Impact).

5.2.6 Electrochemical reaction

Solartron 1287 electrochemical interface was used to provide the bias current for the electrochemical reduction of the cell. The current and voltage curves were recorded at 850 °C using ammonia as the reducing gas and nitrogen source fed to both the cathode and anode.

5.2.7 Microstructure characterization

The morphological features of fracture cross-section of cells were examined by scanning electron microscopy (Zeiss Sigma 300 field-emission scanning electron microscope). Bruker energy-dispersive X-ray spectroscopy (EDS) system with dual silicon drift detectors, each with an area of 60 mm^2 and a resolution of 123 eV, was used for phase characterization.

5.3 Results and discussion

5.3.1 Chemical compatibility

Initially, delamination of the YSZ electrolyte from the titanium dioxide support was observed without the yttria buffer layer shown in Figure 5-2. As the thermal expansion of the titania is very close to YSZ, this indicates chemical incompatibility between YSZ and titanium dioxide.

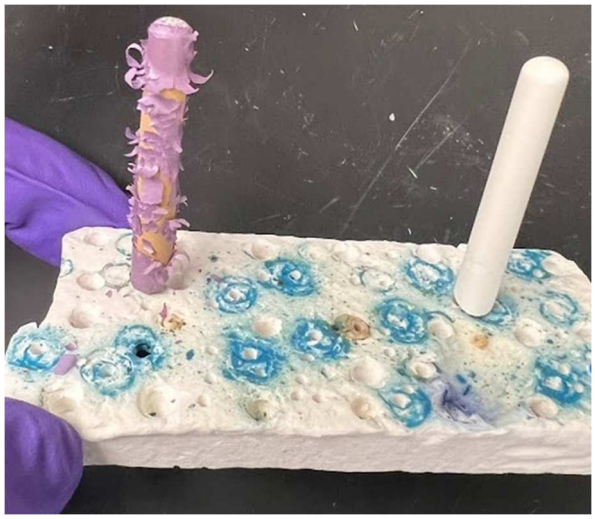

Figure 5-2 (left) Delamination of the electrolyte from the TiO_2 support (right) using yttria buffer layer to prevent delamination of the electrolyte

Several samples were made to analyze further the resulting phase, which was purple. The delaminated coating was collected and ground to fine powders in a mortar and pestle for powder-X ray diffraction (PXRD) to examine the chemical compatibility. Figure 5-3 shows the XRD pattern of the sample.

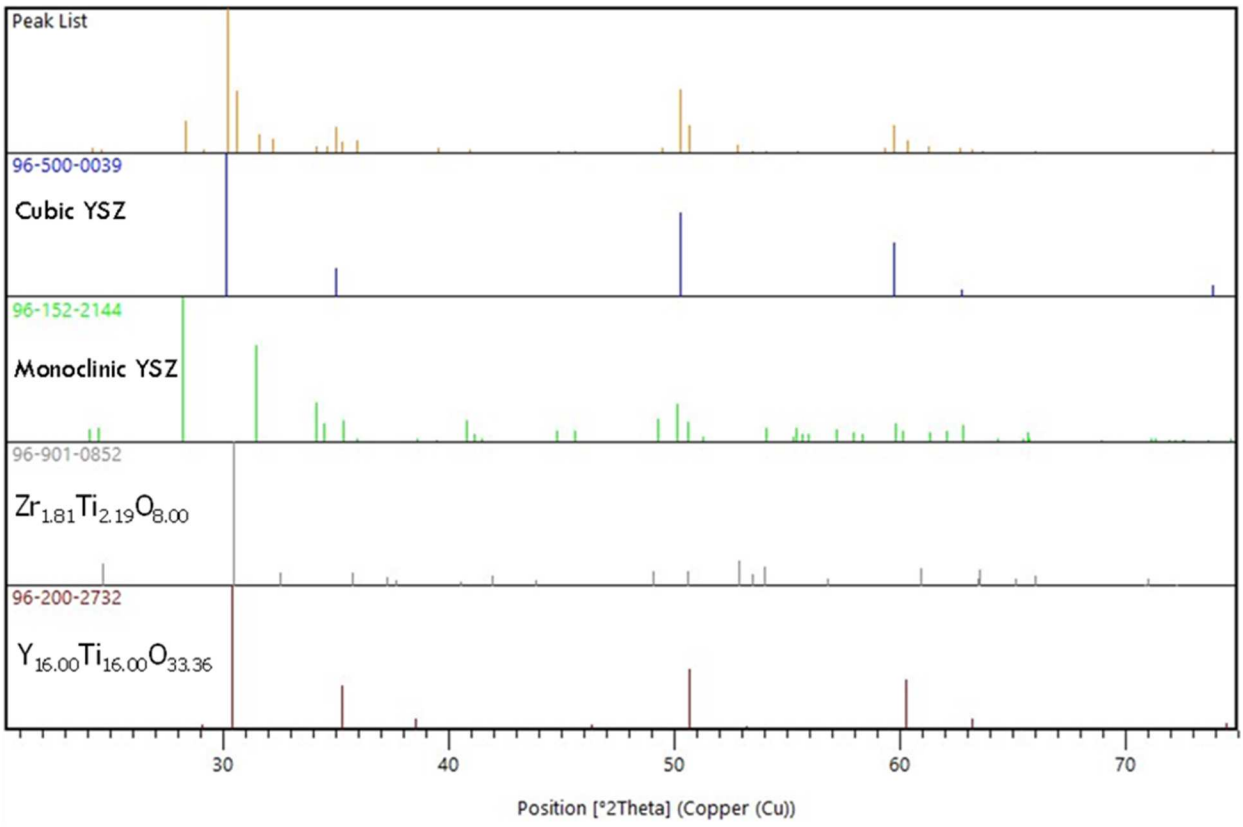

Figure 5-3 XRD pattern of the delaminated electrolyte phase and comparison with possible formed phases.

The XRD pattern reveals the presence of monoclinic YSZ in the electrolyte. Also, zirconium titanate and a trace of yttrium titanate were detected. Although no previous work was found for yttria, similar destabilization of calcium-doped zirconia was reported elsewhere where TiO_2, an acidic oxide, removes the CaO (strong base) from the CSZ structure resulting in crack formation in the product. [142]. For this reason, a yttria-YSZ buffer layer was applied between the titania and YSZ, which prevents titania from soaking out the yttria from the zircona and hence delamination of the electrolyte, as can be seen in Figure 5-2.

5.3.2 Electrochemical reduction

To conduct the electrochemical reduction, first, the cell was heated to 900 °C in the presence of nitrogen. Then the gas was switched to ammonia. Several electrochemical schemes were tested; some resulted in crack formation after the electroreduction. Figure 5-4 demonstrates some of these failures, which resulted in crack formation in the sample. It was concluded that uniform current and lack of any excessive force from current collectors could help mitigate these mechanical damages. Also, a slow ramping current for electroreduction becomes critical as well.

Figure 5-4 Some failures during electrochemical reduction.

Based on this, the galvanostatic mode was used; the current set to 1 A/cm^2 and the running time was set to 24 hours. The applied voltage and current vs. time are shown in Figure 5-5.

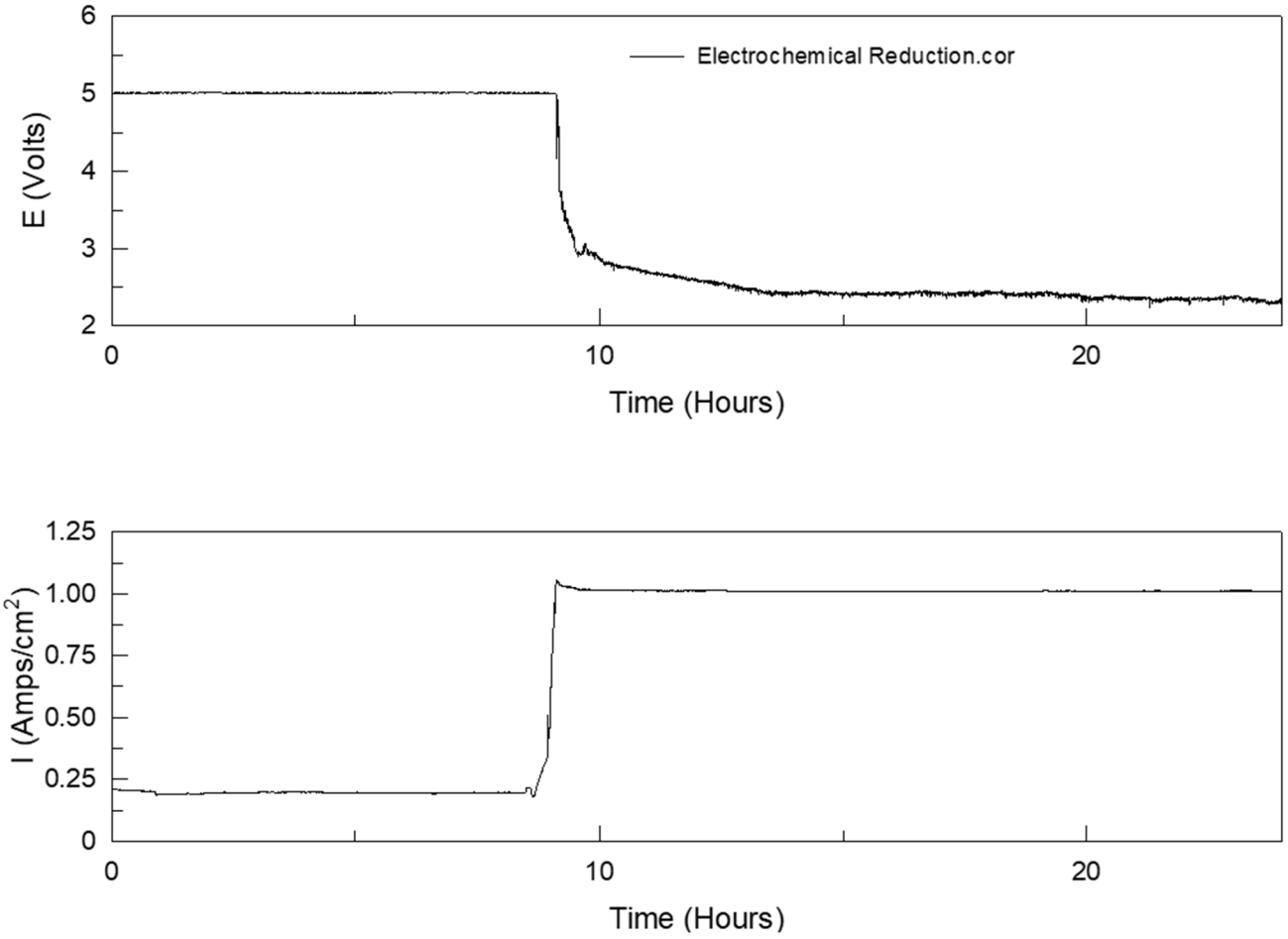

Figure 5-5 Voltage and current measurement vs. time during electrochemical reduction

Initially, due to the considerable electrical resistance of the support, the machine could only apply 5 V and 0.2 A/cm^2. After nine hours, the current suddenly increased to 1 A/cm^2, and voltage decreased rapidly to maintain the galvanostatic mode. The electrochemical reduction was carried out for 24 h, hitting a plateau at the end. The cell was then cooled to room temperature without any current passing through in the presence of nitrogen.

Impedance measurements were also conducted initially, after 9 h, and after 24 hours which are shown in Figure 5-6.

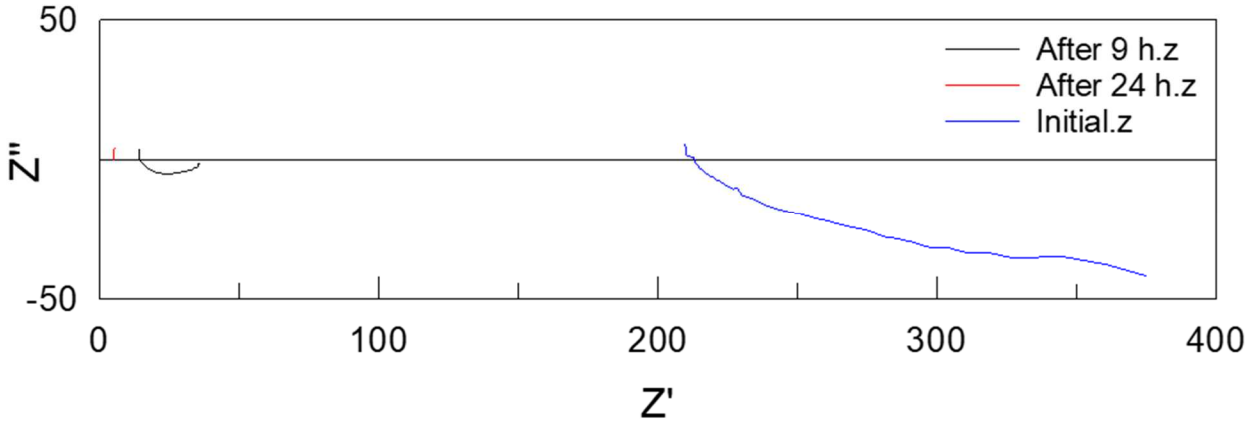

Figure 5-6 Impedance spectrum of electrochemical reduction at t=0, t=9 h, and t=24 h

5.3.3 Cell microstructure

Figure 5-7 Fractured cell after electrochemical reduction

Figure 5-7 shows the fractured cell after removal of the cell. The distinctive golden color indicates the successful formation of TiN. TiN forms primarily as bulk TiN through the thickness, and most of the support was converted to TiN. A small region did not convert to TiN which might be due to imperfect contact of the current collector in that region; the nickel mesh current collector was rolled and putted inside. Failure of contact leads to insufficient current passing through that region and performing the reduction.

Figure 5-8 shows the cross-section micrograph of the support part that was not fully converted to TiN.

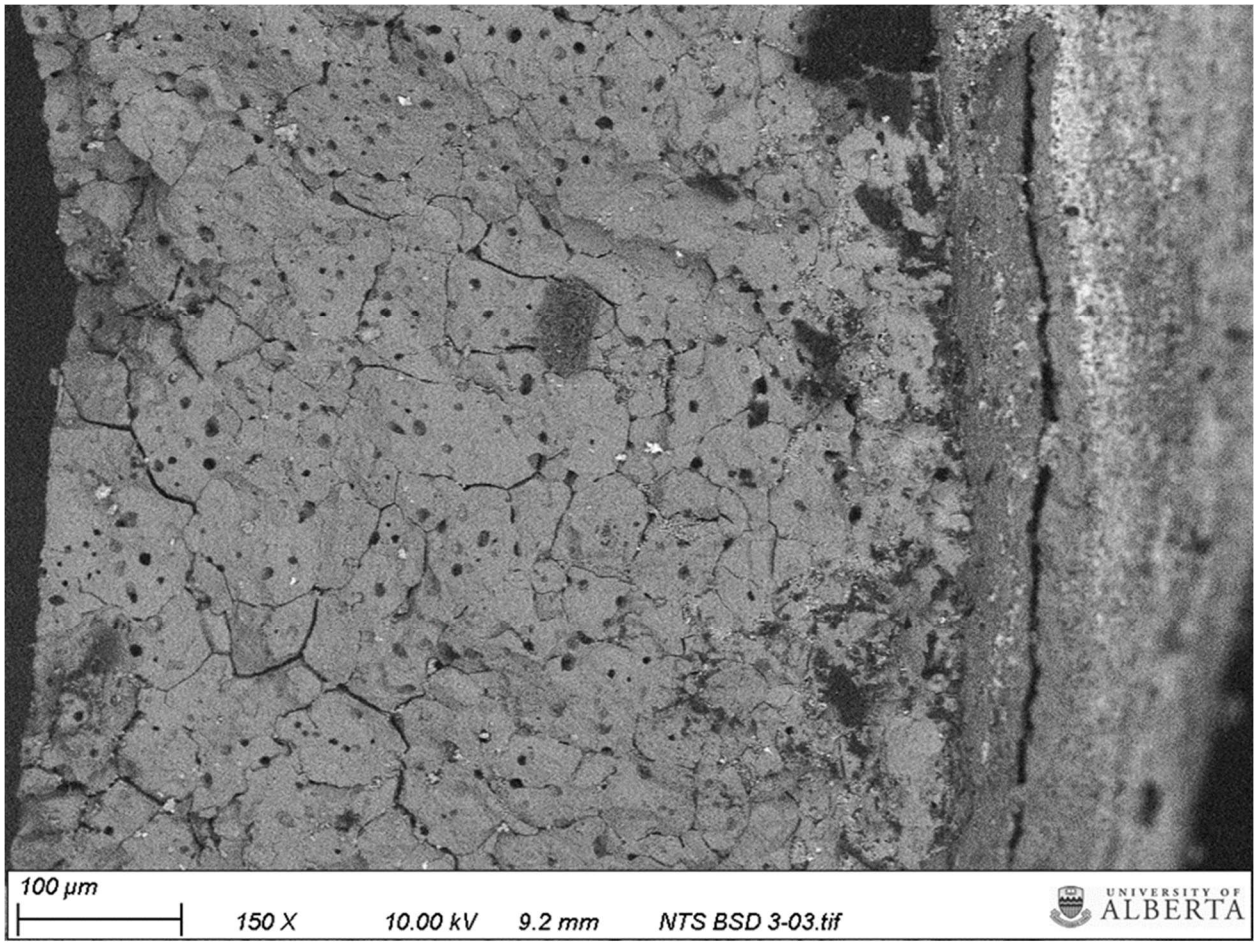

Figure 5-8 Micrograph of fractured cell

Figure 5-9 shows the EDS of the cross-section for the part that was not fully converted to TiN. As can be seen, almost half of the thickness of the support was successfully converted to stoichiometric TiN, and the oxygen present is minimal. For the rest, as we get closer to the electrolyte, the oxygen ratio increases up to stoichiometric TiO_2 while titanium nitride does not form.

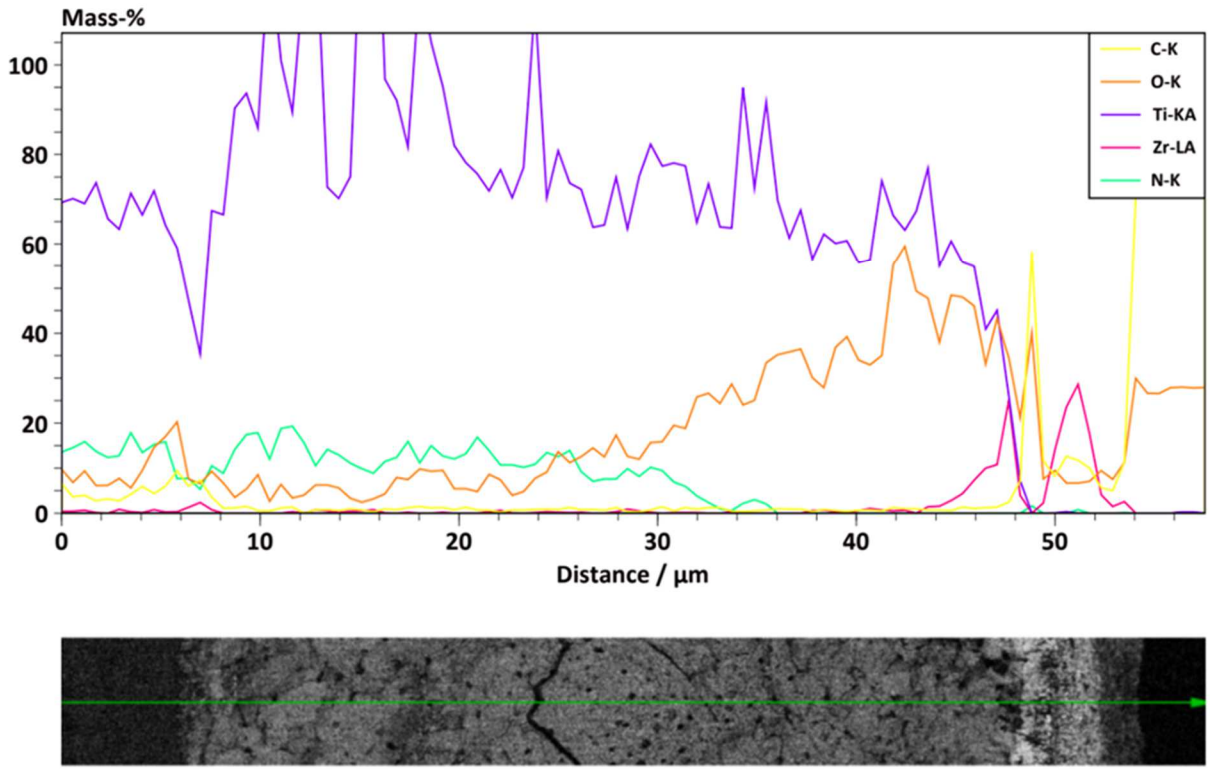

Figure 5-9 EDS characterization of the cross-section

On top of the lack of good contact, we also suspect that the electrolyte in that region might be compromised, which resulted in incomplete TiN formation. Stress might develop during cell assembly from the insertion of the current collector inside the cell, which causes the formation of a microcrack that grows over time at higher temperatures. The stress from the phase change that happens during the electroreduction of the cell might also be another factor worth considering as TiN has several phases with different crystal structures ranging from fcc to rhombohedral and hexagonal. The higher density of TiN (5.21 g/cm^3) vs. TiO_2 (4.23 g/cm^3) indicates a more packed crystal structure for TiN. Unfortunately, detailed studies on TiN phase transformations and transformation from TiO_2 to TiN are scarce and need much more

research. The crack might be mitigated by optimizing the support microstructure to tolerate the resulting stress or adjusting the electrochemical reduction parameters.

5.4 Conclusions

In this study, the electrochemical reduction of titanium dioxide in the presence of ammonia to produce titanium nitride was pursued. Titanium nitride as an electrode offers several advantages compared to current materials, such as high corrosion resistance, high electrical conductivity, and thermal expansion compatibility with the YSZ electrolyte. The chemical incompatibility between titanium dioxide and YSZ shows that the formation of secondary phases destabilizes the YSZ cubic phase and delaminates the electrolyte, hence mandating a yttria-YSZ buffer layer. Titanium nitride was successfully obtained and was analyzed using SEM and EDS for phase characterization.

Chapter 6. Improving Infiltration of Thick Porous Media Using an Electric Field

6.1 Introduction

Due to their ceramic oxide electrolyte, solid oxide fuel cells (SOFCs) operate at higher working temperatures. SOFCs can generate both electricity and useful thermal energy through electrochemical reactions, which yield higher efficiency, fuel flexibility, low emissions and lack of expensive catalysts, making them a viable candidate compared to other types of fuel cells [70]. The inferior power output and inadequate longevity compared to other fuel cells, especially proton-exchange membrane fuel cells, make them less appealing [71]. The high working temperature leads to a higher degradation rate, mandating particular material that can withstand harsh reducing/oxidizing conditions and increasing overall cell price [143].

Many efforts focus on reducing the operating temperature, which lowers the degradation and extends the selection of materials to cheaper alternatives but results in much higher electrolyte resistance and dramatically reduces the performance [68]. Electrode-supported geometry is usually chosen for lower working temperature SOFCs which substantially reduces the electrolyte thickness and lowers the electrolyte resistance contribution; thus, the overall loss is dominated by polarization of the electrode reactions [72]. The structural and microstructural properties of the electrode material have a significant influence on the efficiency of

the electrochemical cell [144]. Hence optimizing the structure of electrodes becomes more crucial; with an enhanced microstructure, the rate of the oxygen reduction reaction (ORR) and hydrogen oxidation reaction (HOR) can increase dramatically. This increase in performance can result from a higher surface area and enhanced microstructure with the correct proportion of the electrode's ionic and electronic phases [67].

Impregnation can be an effective way to achieve this optimized microstructure. It is usually carried out to enhance the catalytic activity by preserving the higher surface area of the catalyst and avoiding the need for high-temperature sintering; infiltration is carried out mainly after sintering of the electrolyte and porous layer as the matrix for the infiltration [145]. Impregnation can be either in the form of salt precursors or a slurry of fine particles, which are then put into a porous scaffold and thermally treated to form well-dispersed nanoparticles through sequential deposition processes. The barebone scaffold is usually an ionic conductor as it needs a higher sintering temperature [74]; additional phase(s) also can be added to enhance the catalytic activity of the existing electrode [87].

Despite all of the advantages of infiltration, it still faces some significant challenges. First, it would be rather challenging to do the impregnation in a thick scaffold; usually, the outer surface of the barebone scaffold sees the most material deposited and blocks further penetration inside [145]. Another major disadvantage is the longevity, as they have a higher degradation rate than the non-infiltrated electrode. As a low quantity of active components is deposited during infiltration, they

aggregate more rapidly over time due to the large surface area at the working temperature and break the well-dispersed percolated catalyst [146]. Infiltration also produces lots of wasted materials, especially in the case of salt precursors; a portion of precursor material leaves the scaffold during heating and need further processing to be used again.

Finding a practical way to force the precursor or the catalyst material to enter the backbone is necessary to overcome many of the mentioned disadvantages. Several approaches have been applied to overcome this problem, such as using vacuum, additives such as surfactant, and a higher concentration of precursors[147, 148]. However, these techniques can be most effective for a smaller porous layer thickness; precipitation of deposited material prevents the infiltrated material from fully penetrating. Another challenge is during the post-heat-treatment of infiltration. As the solvent evaporates and decomposition of precursors and additives occurs, gas byproducts form as the catalyst deposits in the matrix and force the catalyst material outside the matrix, lowering the matrix's overall weight gain, which is crucial for long-term degradation[105]. One solution is to use a more rapid heat treatment in which the precursors decompose in-situ; microwave heating was used as an example elsewhere to overcome this problem [130].

Based on the authors' experience, these techniques require open pores in the range of 50 microns to succeed, which is challenging to obtain and requires more catalyst deposition, making infiltration less appealing.

Plating was used as an alternative solution to creating an electrode with a high surface area [149]. There are several reasons to conduct the electrodeposition, including lowering the coke deposit formation on the nickel-based anode with the help of another material that has lower activity toward breaking hydrocarbon bonds, such as copper.

As one end of the electrode is covered with the electrolyte and the substrate needs to be electron conductive, some adjustments are necessary with respect to conventional electrodeposition. To form the conductive backbone, in one study, copper was electroplated on the anode side of an electrolyte-supported cell; a reduced NiO-YSZ backbone with a 60 micron thickness was used [150]. It was shown that minimizing mass-transfer limitations within the pores and making a highly conducting electrolyte solution is essential for uniform deposition using a sulfate electrolyte and precursors. Park et. al. used the same approach to fabricate a Cu–Ni–YSZ anode for direct methane feeding. Although the results show much better tolerance, the cell eventually failed at 200 h due to coke deposition, indicating that some parts of nickel were in direct contact with the methane as copper is a very poor catalyst for methane cracking; hence the deposition was non-uniform. One major disadvantage of electroplating is it highly depends on the shape of the substrate material as it changes the electrical resistance between the working and counter electrode and leading to uneven current density, which results in uneven deposition [151].

One interesting method to enhance the electrodeposition was to use a temporary conductive layer to improve the deposition rate and uniformity. As the electrolyte is

non-permeative, the conventional method of backbone conductive layer deposition cannot be used. Pyrolysis of C_4H_{10} was used to form polyaromatics on the surface of the backbone before electrodeposition as the conductive layer [139]. This method was highly dependent on the gas flow, the geometry of the flow, and the pyrolysis temperature. Interestingly, after treatment of the deposited layer with steam at high temperatures to remove the graphite layer, ohmic resistance increases by almost 100%, and no specific reason was given to explain it.

Silver was used as the conductive layer in another study on top of GDC using the Tollens method[152]. In contrast to the carbon-based layer, which was removed using steam at high temperature, silver remains as part of the electrode.

Another approach is using an electric field as an external force to push the catalyst inside the scaffold. This approach is very similar to electroplating to deposit the catalyst onto the electrodes. The difference is that in electroosmosis, the external current forces the liquid precursor to penetrate inside electrode backbone channels, increasing the penetration depth. In electrodeposition, the electricity is used to decompose the precursor salt. The voltage in electroosmosis is much higher compared to electroplating [153].

When a surface is in contact with a polar medium, the surface develops some electrostatic charges. An electric double layer is created as a result of these surface charges [154].

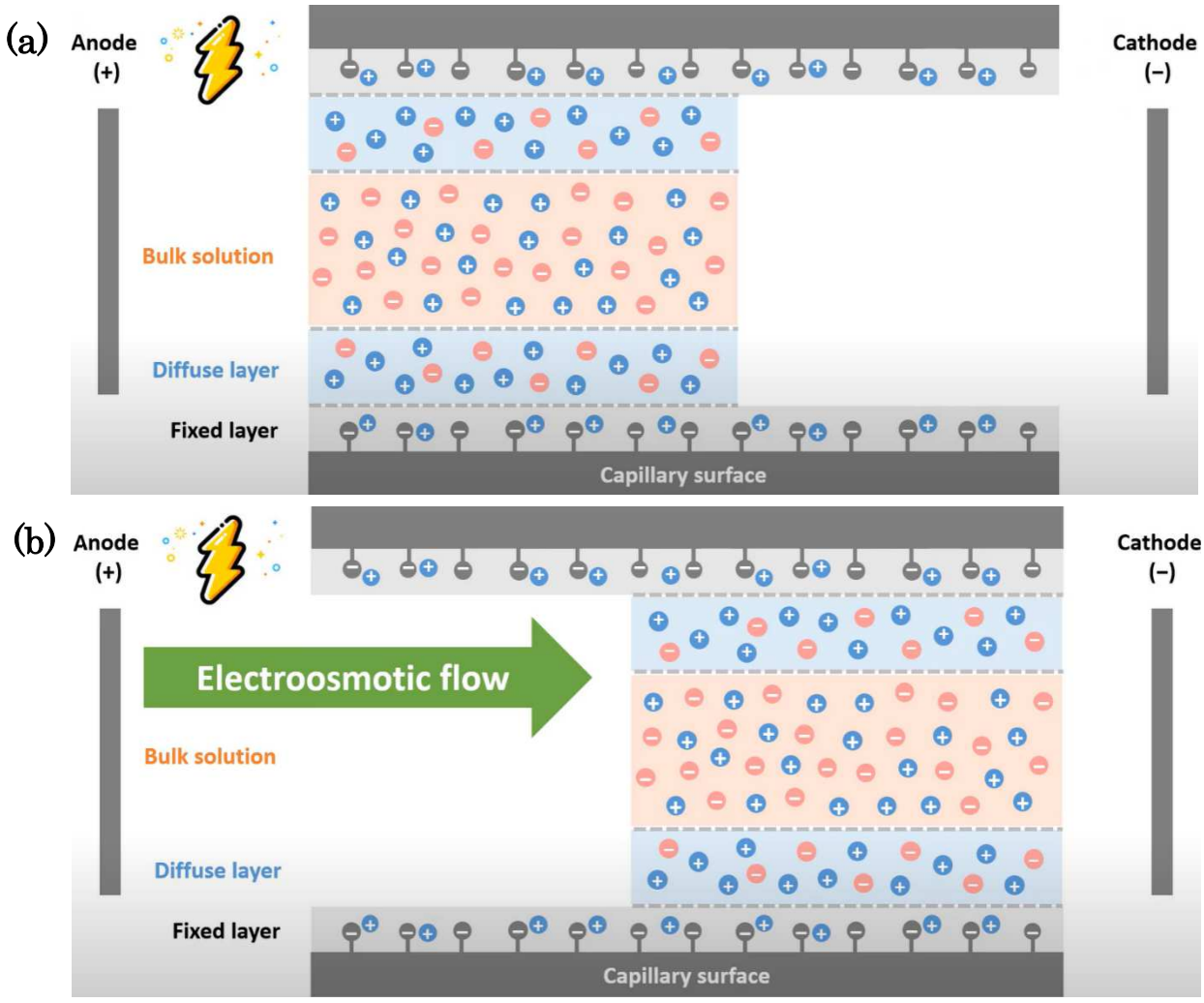

Figure 6-1 (a) Formation of fixed layer and diffuse layer (b) capillary movement due to external voltage

The presence of hydroxide groups on the surface of an oxide develops surface electrical charges in aqueous media. The formation of surface charge is the proton balance between the oxide surface and the suspension, and its equilibrium is determined by their acid-base properties. The nature and magnitude of surface charge depends upon the electrolyte concentration and pH [155]. Since the oxide surface and the suspension are in a constant proton balance, their acid-base properties control the

equilibrium, which leads to the formation of surface charge. The electrolyte concentration and pH have an impact on the type and size of surface charge [156]. The pH of point of zero charge for zirconia ranges from 4-8, depending on the specific surface properties of the solid [156].

An inner compact layer and an outer diffuse layer make up the electric double layer. A layer of immobile counter-ions that are strongly attracted to the surface makes up the inner layer, which is typically several Angstroms thick and located right next to the charged surface [157]. Ions in the diffuse layer, however, are mobile and are less impacted by the charged surface. Since counter ions predominate in the diffuse layer, the local net charge density is not zero. The ions in the diffuse layer would experience an electric force from an external electric field applied tangentially to the electric double layer field, which would cause a net migration of the ions in the EDL region. The moving ions create a bulk electroosmotic flow by dragging nearby liquid with them as can be seen in Figure 6-1 (a) [158].

At a sufficiently large electric field, non-conductive material forms a dipole. YSZ is an electrical insulator material, and it can form dipoles in the presence of a large electric field. The electroosmosis effect is caused by the Coulomb force induced by an electric field on a net mobile electric charge in a solution. As the chemical equilibrium between a solid surface and an electrolyte solution typically leads to the interface acquiring a net fixed electrical charge, a layer of mobile ions known as an electrical double layer forms near the interface. As the electric field is applied to the fluid, the net charge in the electrical double layer is induced to move by the resulting Coulomb

force as seen in Figure 6-1 (b) [159]. This concept is very similar to electrophoretic deposition where, instead of a solution, suspended particles interact with the field [160]. Several successful applications of electrophoresis have been reported [161-163]. Electroosmosis phenomena were also successfully modeled [163], but this is the first time it has been experimentally evaluated.

6.2 Experimental

6.2.1 Support fabrication

As-received YSZ (Tosoh TZ-8Y) was pre-calcinated at 1500 °C for 6 h and then mechanically ball-milled in a water medium (1:1 ratio) for 24 h. To create enough porosity, 50 vol. % graphite (Sigma Aldrich <325 mesh) was added to the mixture, followed by a final pH adjustment to 3 using HCl. Slip casting in a plaster mold was used to make the support. The supports were pre-sintered at 1100 °C with a heating ramp of 2 °C/min for 3 h. Then the outer surface was polished using a clean cloth to make the outer surface smooth and free of any significant imperfections.

6.2.2 YSZ electrolyte coating

The coating slurry consisting of a mixture of as-received 8YSZ (Tosoh TZ-8Y), ethanol, and binder (6 wt % ethyl cellulose in terpineol) was ball-milled for 24 h, followed by ultrasonication to obtain a homogeneous suspension. Three rounds of dip coating were performed at 15 min intervals before drying at room temperature in ambient air. Sintering was conducted at 1400°C for 3 h in air using an electric furnace to yield

a leak-free electrolyte. Methylene blue dye leakage tests were performed after sintering to ensure leak-free electrolytes.

6.2.3 Support infiltration

The infiltration solution was a dimethyl sulfoxide-based solution containing 190 $g.L^{-1}$ $NiSO_4$. $6H_2O$, 10 $g.L^{-1}$ $NiCl_2$. $6H_2O$, 8 $g.L^{-1}$ H_3PO_3, 16 $g.L^{-1}$,H_3BO_3, and 5 $mL.L^{-1}$ H_3PO_4 as explained elsewhere[164]. This precursor was poured inside the thick support matrix, and a graphite rod was used as the working electrode, centered inside the cell. A copper mesh was used as the counter electrode inside a 0.1 molar copper nitrate solution surrounding the YSZ. The entire setup was enclosed inside a custom-made 3D printed cap and a beaker to prevent water evaporation and contamination. Figure 6-2 shows the schematics of the electro-assisted infiltration and the 3D printed cap for this setup. The three holes in the middle were used for holding the sample and the graphite rod. Four outer holes were used for connecting and holding the counter electrode mesh. After infiltration, the cell was removed and sintering was conducted at 850°C in a tube furnace for 3 h under air flow to decompose any possible remaining precursor. The support was then reduced for 3 h under a flow of 20 vol. % hydrogen in nitrogen at the same temperature.

Keithley Model 2440 SourceMeter was used to provide the bias voltage for the electro-assisted infiltration. Compliance voltage was used to prevent the machine from applying excessive voltage.

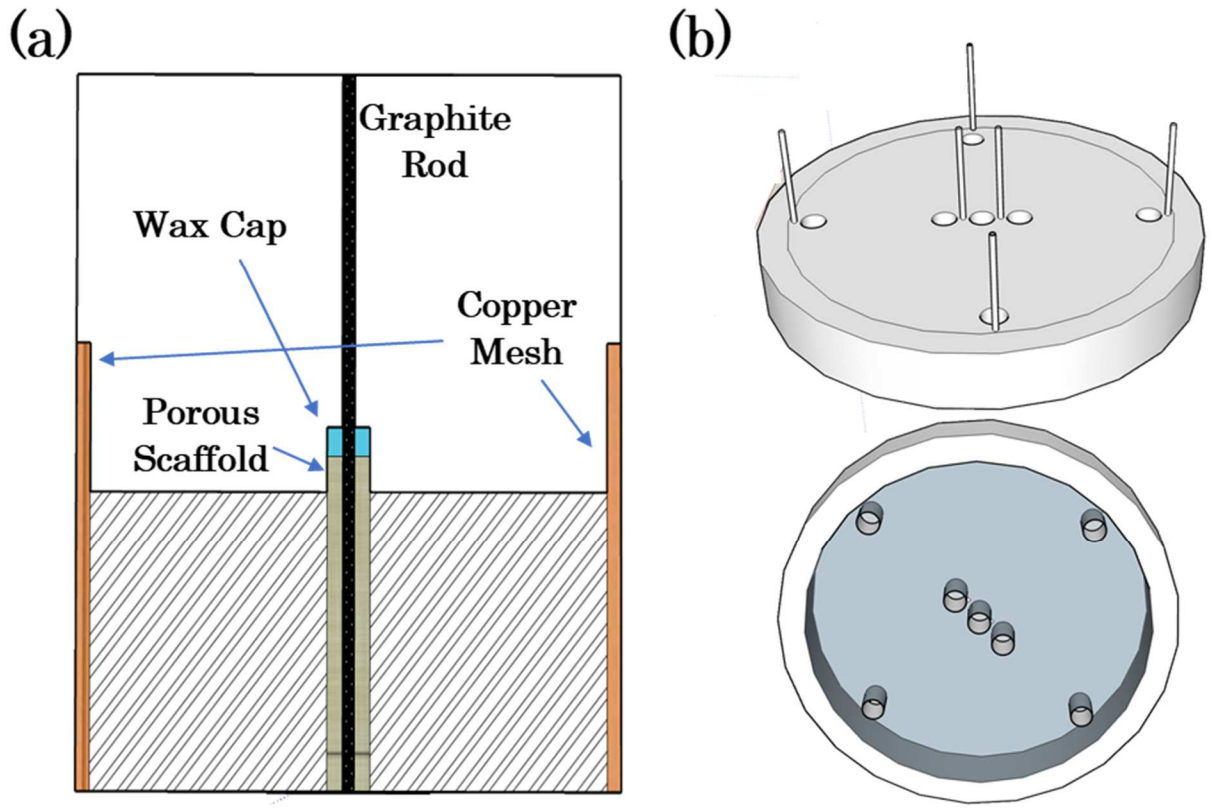

Figure 6-2 (a) cross-section of the electrodeposition setup (b) top and bottom view of 3D printed cap

For comparison, another sample was prepared using the same recipe, but a molten precursor and vacuum to infiltrate were used, as reported in more detail elsewhere [165]. Nickel nitrate, polymeric dispersant (Triton X-45, Union Carbide Chemicals and Plastics Co., Inc.), and water were mixed with a 5:1:0.3 weight ratio and heated at 100 °C. The porous support was heated to 120°C, and the infiltration solution was applied using a vacuum infiltration chamber. The tube was then dried for 15 minutes at 120°C and heat-treated for 15 minutes at 350°C. The infiltration procedure was repeated 15 times to deposit sufficient NiO particles into the YSZ matrix.

6.2.4 Full cell fabrication

A mixture of $La_{0.6}Sr_{0.4}Co_{0.2}Fe_{0.8}O_3$ (LSCF, Fuel Cell Materials), azeotrope solvent, binder (polyvinyl butyral), and Menhaden fish oil as the dispersant was used for the cathode ink. The resulting mixture was dip-coated on top of the electrolyte, then sintered at 1000 °C for 3 h. Gold paste and wires and copper mesh and wires were used for the cathode and anode lead connections, respectively.

6.2.5 Electrochemical characterization

An electronic load and scanner (Agilent model N3301 and E4970A) measured the current-voltage curves. A Solartron 1255 frequency response analyzer and Solartron 1287 electrochemical interface were used for electrochemical impedance spectroscopy (EIS) measurements. The frequency range was between 0.01Hz - 1MHz, with 12 points per decade under open-circuit conditions. The data were recorded with 50 °C intervals in a temperature range of 600 °C – 750 °C using H_2+3vol.% H_2O as fuel feed and air as the oxidant.

6.2.6 Microstructure characterization

The morphological features of fracture cross-section of cells were examined by scanning electron microscopy (Zeiss Sigma 300 field-emission scanning electron microscope). Bruker energy-dispersive X-ray spectroscopy (EDS) system with dual

silicon drift detectors, each with an area of 60 mm^2 and a resolution of 123 eV, was used for phase characterization.

6.3 Results and discussion

6.3.1 Adjusting the initial infiltration parameters

The amount of voltage is limited by the YSZ electrolyte breakdown voltage; exceeding this amount can permanently damage the electrolyte, and several cracks can occur throughout the electrolyte, as seen in Figure 6-3.

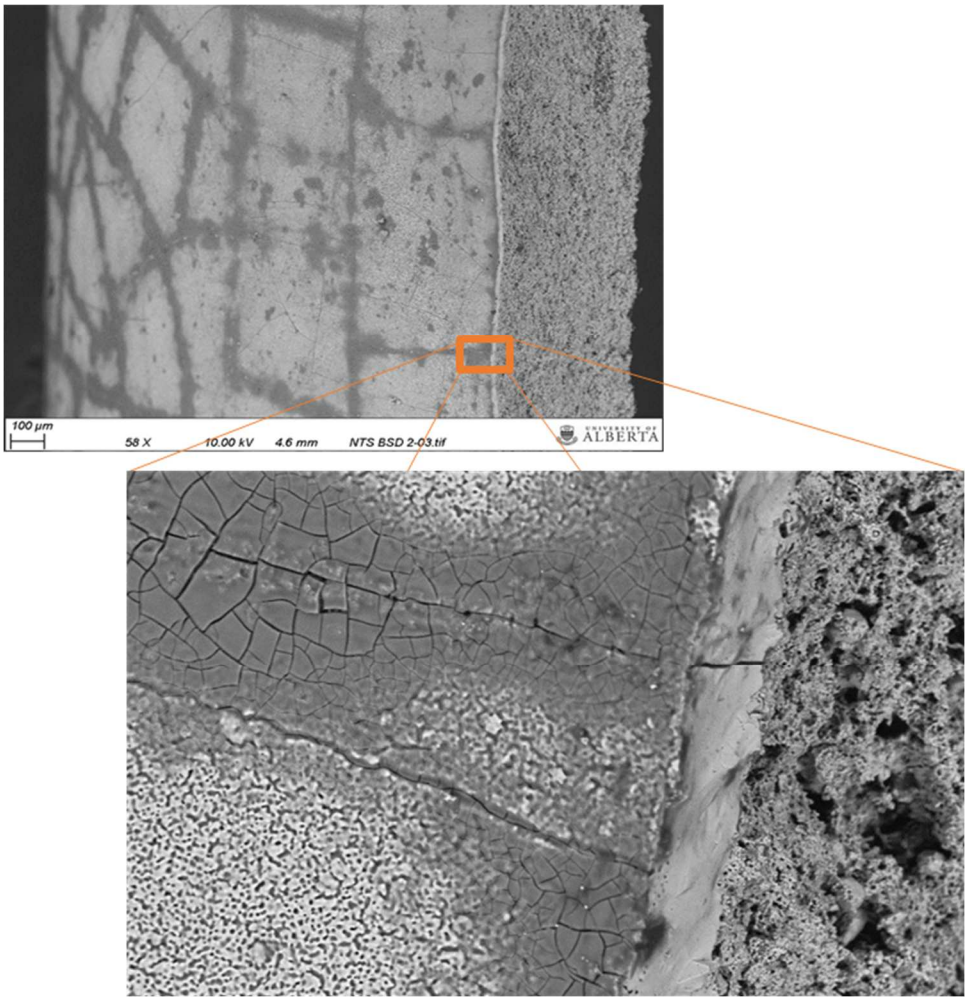

Figure 6-3 Permanent damage to the electrolyte due to exceeding breakout voltage

The darker color is nickel that is electrodeposited around the affected area, which will short circuit the cell under operational conditions. Damage was only limited to the electrolyte and not the entire support. It is possible to estimate the breakout voltage in our case; for fully dense cubic YSZ, the value is 1.6 to 1.7 MV/cm in bulk form sintered at 1400 °C [166]. Based on our experiments, this value is much smaller than anticipated and depends on the current passage duration as well. For 24 h duration, we estimated the breakage voltage to be around 100 V. This discrepancy might be due to imperfections in the electrolyte. We speculate that in thinner regions, especially those with structural defects, stress points can form, and micro-cracks can start to grow and cause significant cracks in the electrolyte, compromising cell integrity.

Thus, it is imperative to have a uniform electrolyte thickness and voltage distribution around the working and counter electrode to minimize any possible mechanical failure.

6.3.2 Infiltration process

The electro-assisted infiltration was conducted in galvanostatic mode set to 1 μA current and compliance voltage of 40 volts to prevent electrolyte damage during the process for 24 h. It is important to mention the current is intentionally kept at a very moderate level, and the deposition rate can be significantly enhanced for future work. The current and voltage were recorded over time, as seen in Figure 6-4.

Initially, the voltage was limited to 40 V due to compliance with the power supply as the current could not reach 1 µA. Then as the current goes to 1 µA, the voltage starts to decrease. We suspect at this stage the electroosmosis effect forces the infiltration suspension to penetrate through the pores of the scaffold and makes the whole scaffold conducting. Then the small inherent leakage of the electrolyte causes the electrodeposition of nickel onto the YSZ scaffold. Nickel oxide can be obtained from weak basic or neutral solutions of Ni^{2+} using the electro-oxidation technique as reported elsewhere [167].

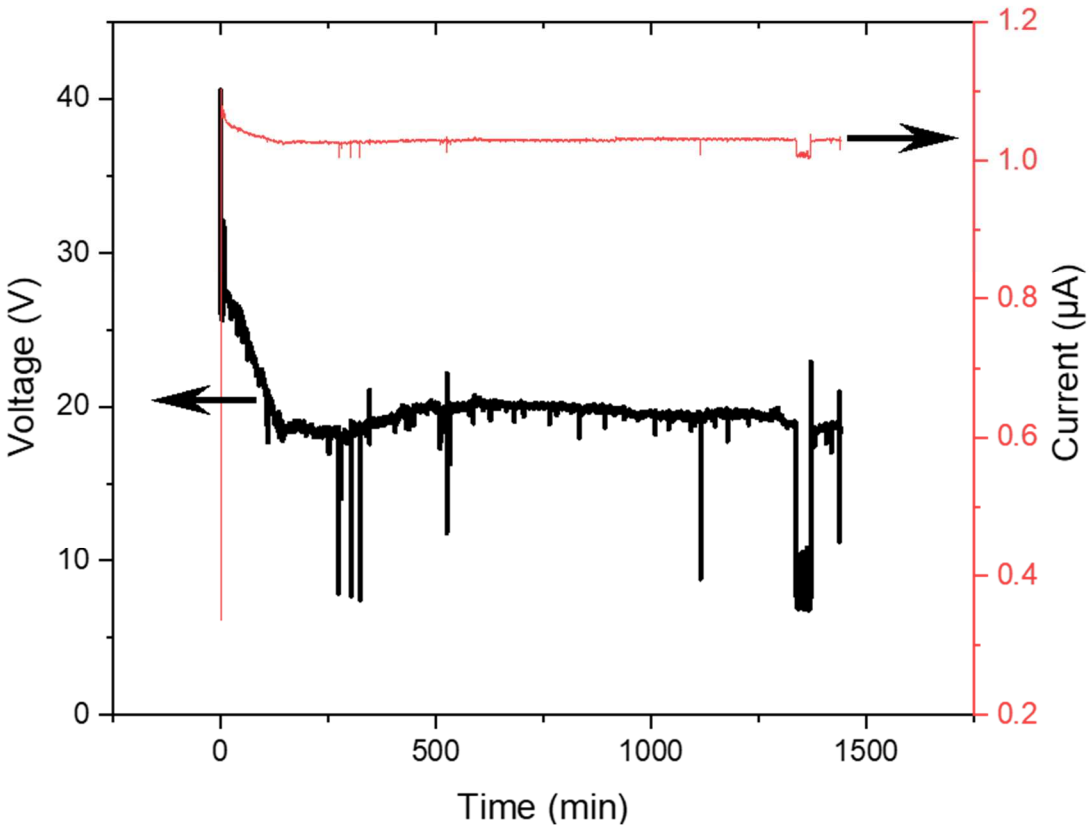

Figure 6-4 Voltage and current vs. time during infiltration

We assumed that a preferred path for particle deposition in the case of a non-metal deposit would be adjacent to the previous particle. By contrast, if suitable conditions

for nickel metal formation exist, they form on top of each other and give an overall filament shape as this has less electrical resistivity. The non-metal deposition ensures a homogenous deposit throughout the backbone, as shown in Figure 6-5 schematically.

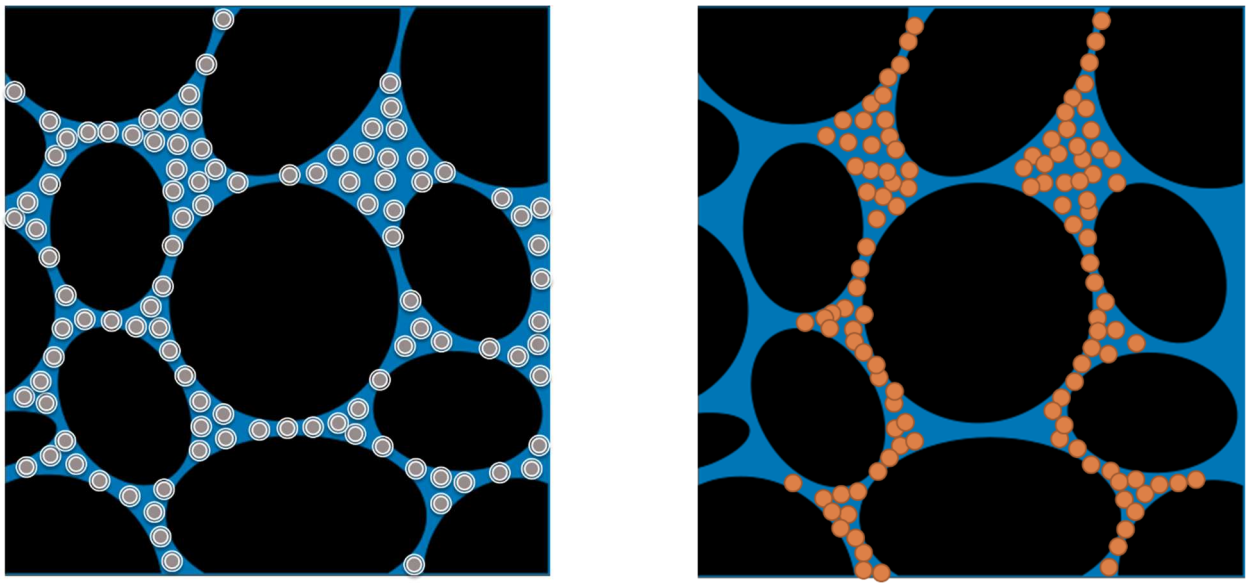

Figure 6-5 Particle prefered deposition in case of (a) nickel oxide (b) nickel metal

We anticipate as the non-metal deposition grows larger, the overall resistivity of the scaffold goes higher, which increases the voltage, as confirmed in Figure 6-5.

6.3.3 Electrochemical performance

Figure 6-6 shows the power and power density output curves of the electro-assisted infiltrated cell measured under air/H_2+3vol.% H_2O. The open current voltage is very close to theoretical values based on the Nernst equation, suggesting a dense electrolyte that prevents direct charge transfer or gas permeability and no damage to the electrolyte occurred during the infiltration process.

At low currents, the cell's behavior is primarily linear, which indicates that the ohmic resistance of the cell limits the performance. Only at 600 °C, a small activation polarization at low currents can be seen. At low current density, lowering the operation temperature leads to more significant activation polarization [168].

At higher currents, the end of the curves, which result from concentration polarization and fuel starvation, becomes more significant and deviates from the conventional cell's ohmic behavior, resulting in lower performance for the sample. We suspect this might be due to the not fully optimized support structure and insufficient cathode performance. As explained elsewhere[130], the latter can be further enhanced by infiltrating the cathode.

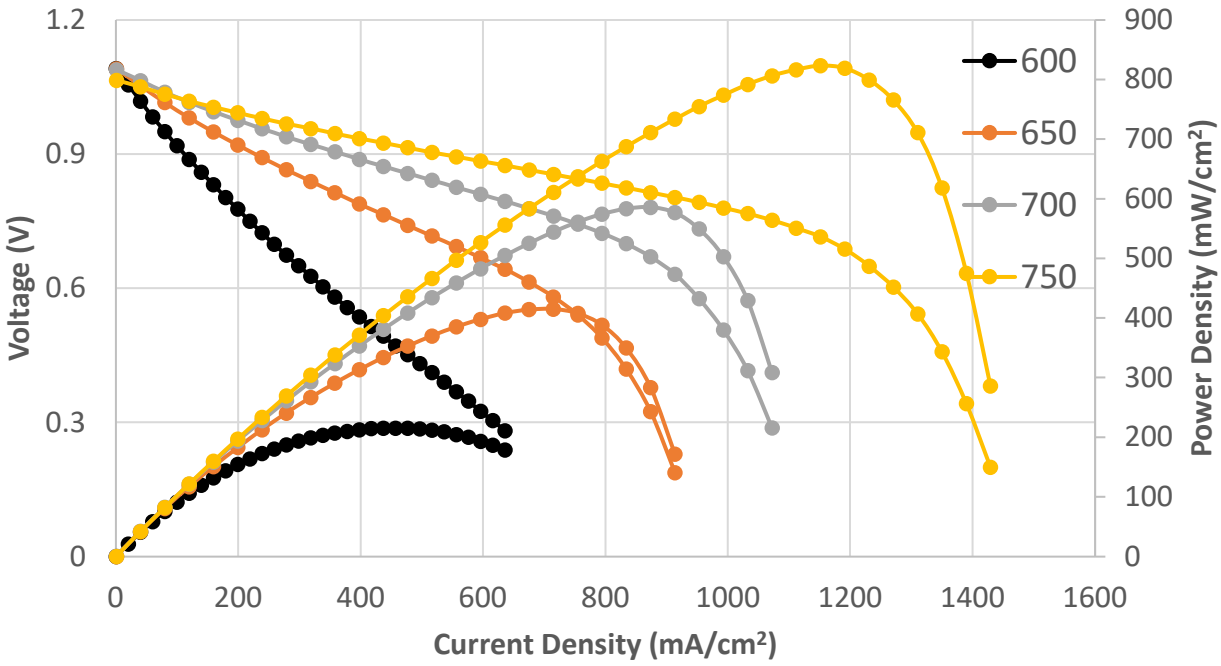

Figure 6-6 Electrochemical performance of the infiltrated cell

Figure 6-7 shows the EIS of the cell at different temperatures. The far-right polarization that is temperature independent belongs to mass transfer occurring at the electrodes arising both from the cathode contribution [58] and surface electrochemical reactions at the anode [49, 127]. This contribution is minimal compared to the conventional cell with a larger impedance value which shows enough porosity still exists in the support.

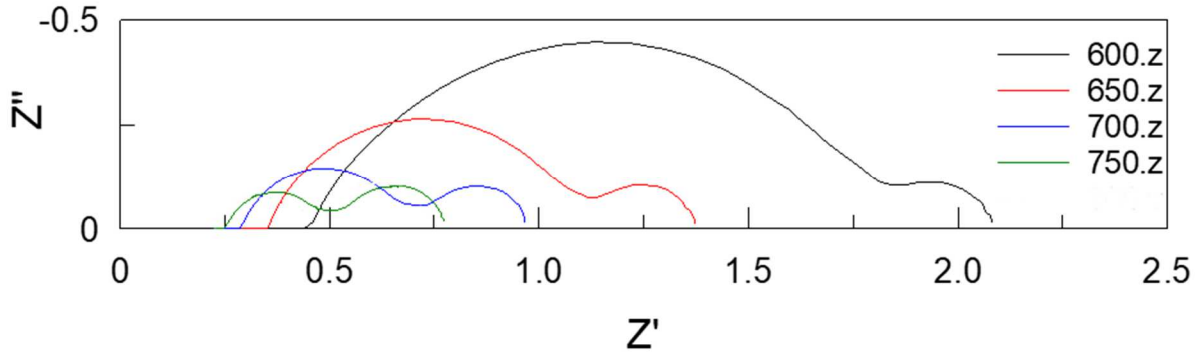

Figure 6-7 Nyquist plots of cell at different operating temperatures

The high-medium frequency semicircle contribution is related to charge transfer resistance corresponding to electron-ion transfer processes occurring at the interfaces and also non-charge transfer processes corresponding to surface reactions [86]. The ohmic part of the impedance correlates to the electrolyte and the connections. The value for the ohmic part is minimal and shows good electrical connection through the support of the cell. One reason might be due to the large enough weight gain during infiltration, which provides enough electrically conductive pathways.

6.3.4 Cell microstructure

Figure 6-8 shows the fractured scaffold at three different stages, before infiltration, after 6 h, and after infiltration. The total thickness of the support was 400 microns. The pre-infiltration microstructure is distinctive, as each grain has many small holes inside. We speculate the low heating ramp caused the coarsening to be more prevalent and forms this microstructure; coarsening mechanisms usually prevail over densification mechanisms at lower temperatures. Thus, slower heating to higher temperatures can be beneficial to achieving low density[169].

As can be seen, the deposition starts adjacent to the electrolyte (left side), then progresses through the outer side of the scaffold, where the nickel precursor and graphite rod are located. During the deposition, it can be seen that the nickel was starting to fill the voids inside the YSZ scaffold. Yet, it was homogeneous deposition rather than being heterogeneous. The average deposited particle size was estimated to be 250 nm. The scaffold's porosity measured by Archimedes' method using water as the suspending fluid was estimated to be 52%.

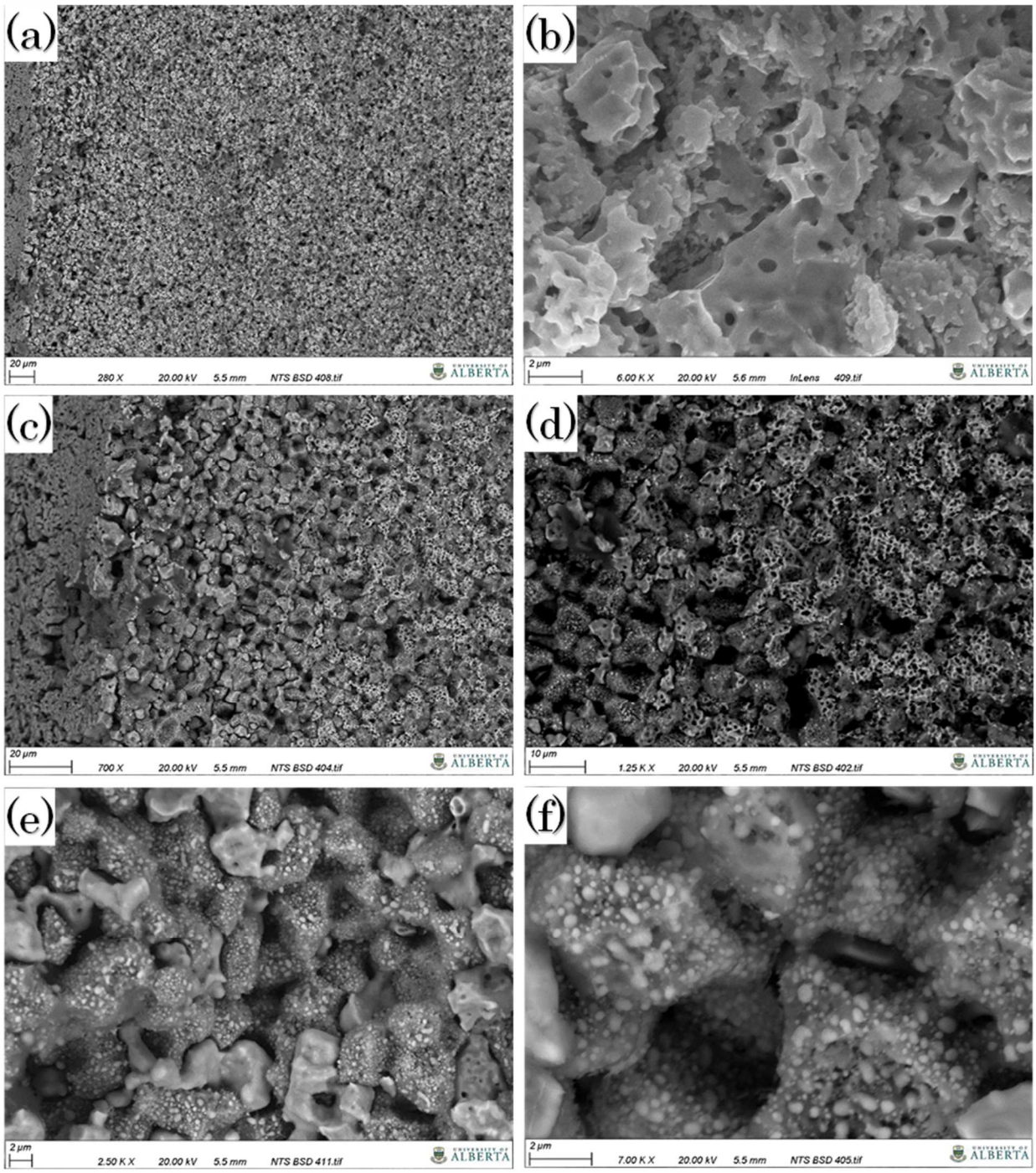

Figure 6-8 (a), (b) scaffold before infiltration, (c), (d) scaffold after 6 h of infiltration (e), (f) scaffold after infiltration

Figure 6-9 shows the amount of weight gained through the scaffold. The graph shows that the infiltration depth is much higher and more uniform, especially near the electrode. Compared to the conventional method, electric assisted infiltration showed lower weight gain at the outer part of the cell where infiltration started. During the removal of the cell, we observed some of the particles came off the cell. We suspect that these particles, as they do not have sufficient attachment to the backbone, can come off very easily; hence the weight gain for the electric assisted cell in that region would be lower. In the case of conventional, since we do not conduct the infiltration in an aqueous medium, we see much higher weight gain. This lower weight gain can be compensated by adding nickel and then sintering.

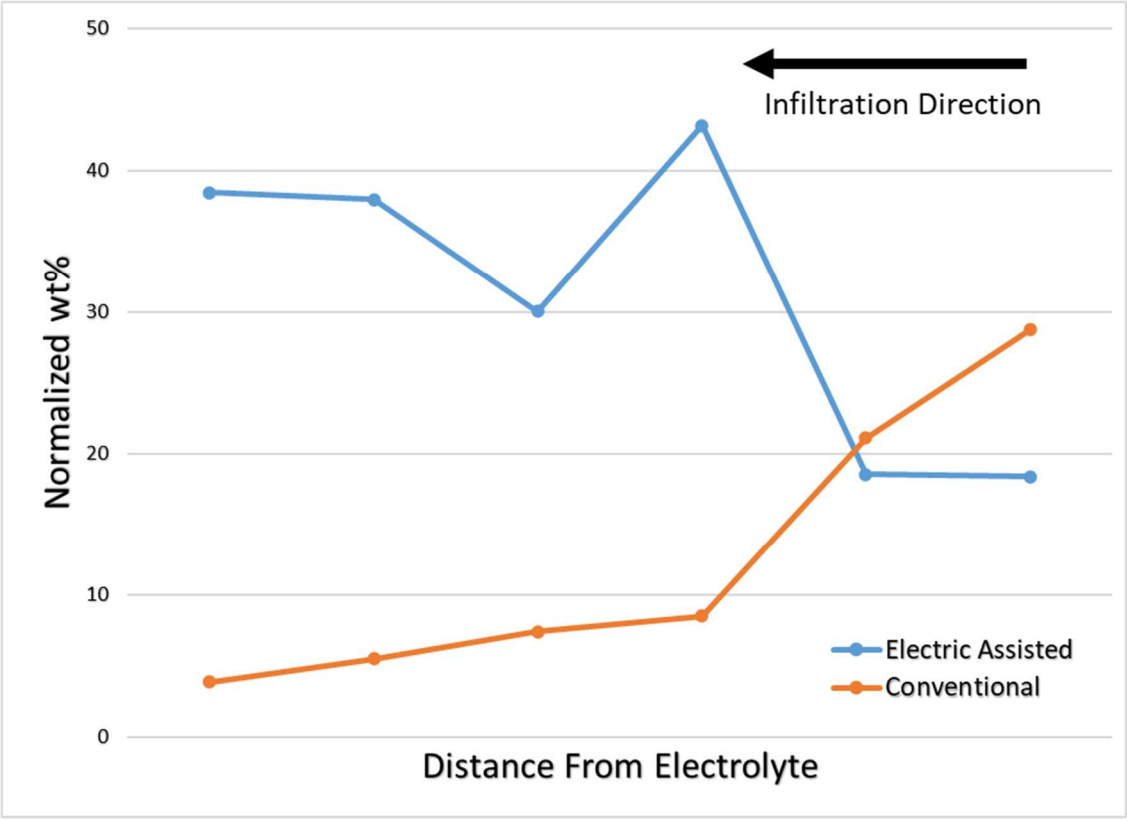

Figure 6-9 Weight measurement of deposited nickel

Figure 6-10 shows the EDX map of an infiltrated region after the fuel cell test. Nickel particles underwent some agglomeration compared to before the fuel cell test but mostly retain their nano-sized structure with their web still intact due to the sufficient presence of nickel as observed previously in weight gain measurements. The nickel particles' tendency to minimize their surface energy by forming a circular shape over time can be seen here as reported elsewhere [170].

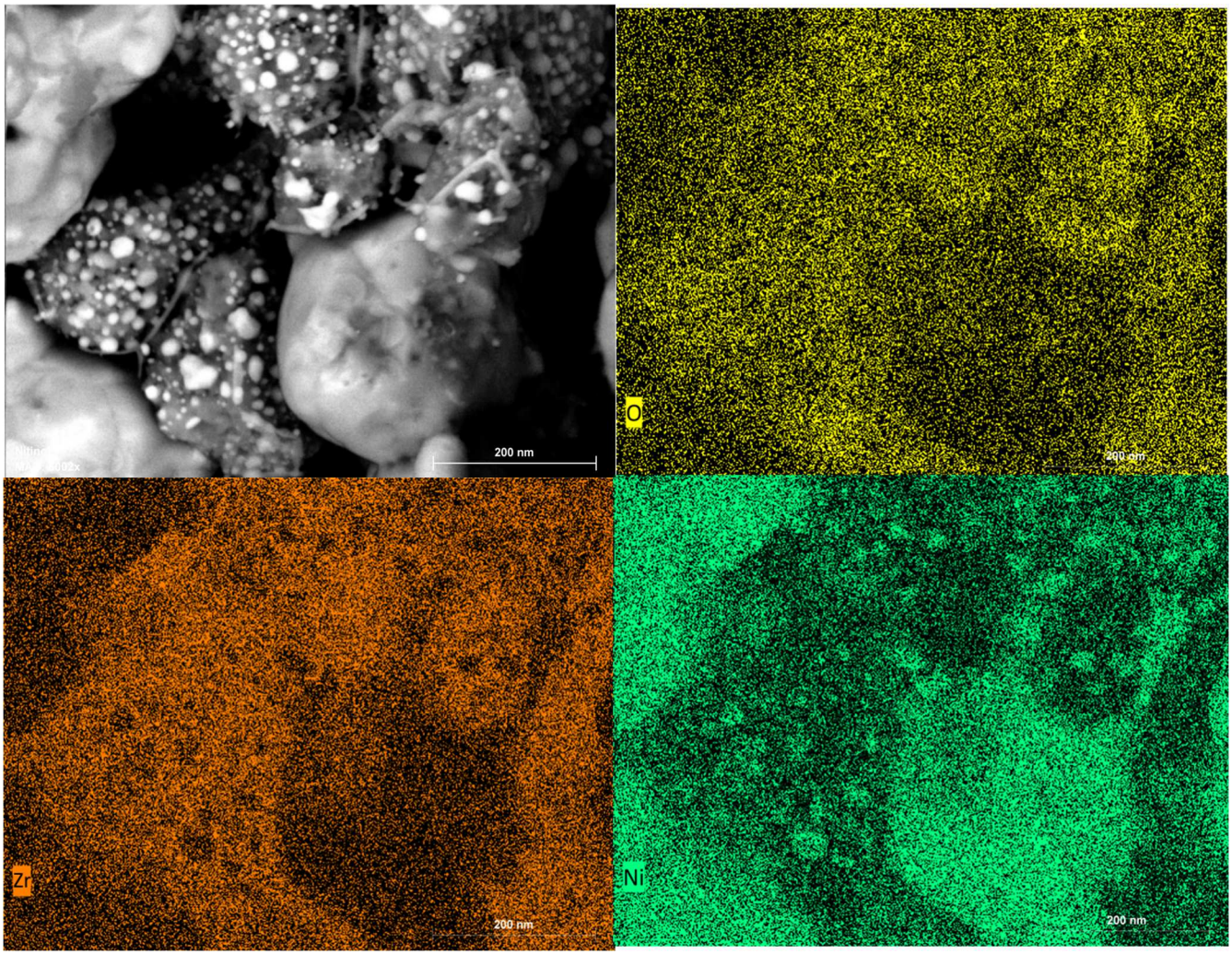

Figure 6-10 EDX map of infiltrated nickel inside the YSZ scaffold

By contrast, in conventional infiltration, a large portion of the infiltration material is deposited near the point of the entry of the infiltration slurry, effectively blocking any further infiltration into a thick matrix.

6.4 Conclusions

This study incorporated an enhanced infiltration technique using an electric field. A 400-micron thick support confined with the electrolyte on one side was used. Nickel precursor for the infiltration and a basic pH were used to obtain a uniform infiltration. Compared to conventional infiltration methods, which suffer extensively from penetration depth, the new method offers higher weight gain. Several adjustments were necessary to prevent catastrophic damage to the cell during the infiltration process. The electrochemical performance shows excellent results with minimum overall resistance of the cell. SEM and EDS were used for phase characterization and to study the microstructure. Results show that this method is an effective way to enhance infiltration and improve the performance of the electrochemical devices.

Chapter 7. Conclusions

7.1 Concluding remarks

Although SOFCs have numerous advantages compared to other types of fuel cells, including higher efficiencies, fuel diversity, and lack of need for expensive catalysts, the lower performance and lack of durability in the long term are still a severe challenge for their practical usage. Lowering the operating temperature is the key to increasing the system's longevity. Maintaining the necessary performance requires either the development of new msaterials for cell components or improving the structural and functional characteristics of electrodes. The most significant contribution of this work to SOFC scientific literature is the persuasion of these two approaches, which increased the cell's performance and lowered manufacturing costs. A new proton conductor electrolyte $Ba_{0.5}Sr_{0.5}Ce_{0.6}Zr_{0.2}Gd_{0.1}Y_{0.1}O_{3-\delta}$ (BSCZGY) has been used in a hydrogen conductor SOFC. This electrolyte has excellent chemical compatibility in the presence of moisture and carbon dioxide, which hinders cerate-based proton conductors. Its remarkable power output combined with excellent chemical compatibility in the presence of moisture and carbon dioxide, which inhibits the wide use of cerate-based proton conductors, makes this material an ideal choice for industrial applications.

Utilizing microwave irradiation can significantly enhance performance and speed up the sintering processing time with significant cost savings.

Infiltrating a thin porous scaffold on top of an electrolyte forms a high surface area catalyst that is finely distributed over a conductive matrix and could dramatically increase the performance. The combination of microwave irradiation in conjunction with salt infiltration was used for rapid catalyst synthesis inside the porous YSZ layer. This approach resulted in an increase in the performance of the cell compared to the traditional electric resistance furnace. With the use of the DRT technique to deconvolute the impedance data combined with microstructural analysis, it was concluded the enhancement of this technique came from the enhanced morphology of the resulting particles.

Using a direct way to incorporate it using a reduced support can open up new ways; it can simplify the usage of microwave sintering due to lack of any susceptor and being able to sinter poorly microwaved coupled materials, which would be extremely difficult and expensive to sinter using traditional methods. This study shows the successful integration of this method for YSZ.

Titanium nitride has excellent properties such as excellent electrical conductivity, corrosion resistance up to 800 °C, and thermal expansion very close to YSZ. Unfortunately, the sintering of TiN is extremely difficult and becomes the biggest challenge. We successfully used a very similar setup to our existing solid oxide fuel cells to convert titanium dioxide support to titanium nitride electrochemically. This method offers several advantages, including a much cheaper and viable sintering process, and most importantly, the same cell can be used as a fuel cell or electrolyzer.

TiN might address several key disadvantages of fuel cells, such as using direct hydrocarbon fuels and long-term electrode grain growth.

It was shown that by applying an electric field, the infiltration process could be enhanced. The new method fixed two major conventional infiltration drawbacks, penetration depth, and low weight gain. The infiltration parameters and necessary steps to prevent damaging the cell during the infiltration process were discussed. The electrochemical performance shows excellent results with minimum overall resistance of the cell. SEM and EDS were used for phase characterization and to study the microstructure. Results indicated using an electric field could be an effective way to enhance infiltration and improve the performance of the electrochemical devices.

7.2 Recommendations for future studies

The following can be the subjects of further investigations:

1. The long-term stability of $Ba_{0.5}Sr_{0.5}Ce_{0.6}Zr_{0.2}Gd_{0.1}Y_{0.1}O_{3-\delta}$ needs further research, especially the phase stability under operating conditions. It would be helpful to test the new electrolyte in the presence of CO and CO_2. If successful, this electrolyte can then separate hydrogen and CO, which would be extremely useful as a dry-reformer electrolyte to produce carbon monoxide.
2. The parameters of microwave-assisted infiltration can be further enhanced. Additives such as surfactants can further improve the performance of the deposited catalyst. The sequence of infiltration steps can be optimized as well.

3. The addition of automation for the microwave sintering process. A feedback loop system with direct temperature control of heating using thermometers and power regulation software of microwave output enables a more precise sintering temperature, more uniform heating, and lowers the chance of thermal runaways.
4. Using a custom microwave chamber for microwave heating. Although a modified household microwave oven was used for this study as proof of concept, it was not optimized for high-temperature sintering; the non-uniform distribution of microwave irradiation, temperature, and insulation was not perfect. Using a custom-made chamber enables better insulation, temperature measurement, and uniform heating.
5. Using extrusion to prepare a more consistent support for microwave sintering. Extruded support can prohibit thermal runaways due to the uniform heating of the support. Reducing the support would no longer be necessary using a metal precursor, and one-step microwave sintering can be used to sinter the support and the electrolyte.
6. Using direct microwave sintering to sinter poor sintering electrolytes such as barium zirconate. The poor sintering behavior can be overcome using this technique.
7. Several optimizations are still necessary for the electrochemical conversion of titanium dioxide to titanium nitride. This includes optimizing the microstructure and the electrochemical process. Most importantly, TiN must

be tested in actual fuel cell and electrolyzer conditions to assess its catalytic activity, performance and long-term stability.

8. Using the new infiltration technique with copper or other material to assess the cell's performance under hydrocarbons. Several parameters such as scaffold microstructure, pH, voltage, duration and geometry of the setup need to be optimized to conduct the new method in a shorter period of time.

References

1. Edwards, P.P., et al., *Hydrogen and fuel cells: towards a sustainable energy future.* Energy policy, 2008. **36**(12): p. 4356-4362.
2. Braun, R.J., *Optimal design and operation of solid oxide fuel cell systems for small-scale stationary applications*. 2002: The University of Wisconsin-Madison.
3. Wang, K., et al., *A Review on solid oxide fuel cell models.* International Journal of Hydrogen Energy, 2011. **36**(12): p. 7212-7228.
4. Lashtabeg, A. and S.J. Skinner, *Solid oxide fuel cells—a challenge for materials chemists?* Journal of Materials Chemistry, 2006. **16**(31): p. 3161-3170.
5. Institute, B.M., *Manufacturing cost analysis of 100 and 250 kW fuel cell systems for primary power and combined heat and power applications*. 2016, United States Department of Energy Golden.
6. Chen, Y., et al., *Advances in cathode materials for solid oxide fuel cells: complex oxides without alkaline earth metal elements.* Advanced Energy Materials, 2015. **5**(18): p. 1500537.
7. Stambouli, A.B. and E. Traversa, *Solid oxide fuel cells (SOFCs): a review of an environmentally clean and efficient source of energy.* Renewable and Sustainable Energy Reviews, 2002. **6**(5): p. 433-455.

8. Mamak, M., et al., *Lanthanum strontium manganite/yttria-stabilized zirconia nanocomposites derived from a surfactant assisted, co-assembled mesoporous phase.* Journal of the American Chemical Society, 2003. **125**(17): p. 5161-5175.

9. Ormerod, R.M., *Solid oxide fuel cells.* Chemical Society Reviews, 2003. **32**(1): p. 17-28.

10. Tietz, F., H.P. Buchkremer, and D. Stöver, *Components manufacturing for solid oxide fuel cells.* Solid State Ionics, 2002. **152-153**: p. 373-381.

11. Hossain, S., et al., *A review on proton conducting electrolytes for clean energy and intermediate temperature-solid oxide fuel cells.* Renewable and Sustainable Energy Reviews, 2017. **79**: p. 750-764.

12. Hempelmann, R., *Hydrogen diffusion mechanism in proton conducting oxides.* Physica B: Condensed Matter, 1996. **226**(1-3): p. 72-77.

13. Fergus, J.W., *Electrolytes for solid oxide fuel cells.* Journal of Power Sources, 2006. **162**(1): p. 30-40.

14. Fabbri, E., D. Pergolesi, and E. Traversa, *Materials challenges toward proton-conducting oxide fuel cells: a critical review.* Chemical Society Reviews, 2010. **39**(11): p. 4355-4369.

15. Guo, Y., et al., *Zirconium doping effect on the performance of proton-conducting BaZryCe0.8−yY0.2O3−δ (0.0≤y≤0.8) for fuel cell applications.* Journal of Power Sources, 2009. **193**(2): p. 400-407.

16. Iwahara, H., *High temperature proton conducting oxides and their applications to solid electrolyte fuel cells and steam electrolyzer for hydrogen production.* Solid State Ionics, 1988. **28**: p. 573-578.

17. Babilo, P., T. Uda, and S.M. Haile, *Processing of yttrium-doped barium zirconate for high proton conductivity.* Journal of Materials Research, 2007. **22**(5): p. 1322-1330.

18. Iwahara, H., et al., *Proton conduction in sintered oxides based on BaCeO3.* Journal of the Electrochemical Society, 1988. **135**(2): p. 529-533.

19. Iwahara, H., et al., *Proton conduction in sintered oxides and its application to steam electrolysis for hydrogen production.* Solid State Ionics, 1981. **3**: p. 359-363.

20. Ryu, K.H. and S.M. Haile, *Chemical stability and proton conductivity of doped BaCeO 3–BaZrO 3 solid solutions.* Solid State Ionics, 1999. **125**(1): p. 355-367.

21. Hanifi, A.R., et al., *Fabrication and characterization of a tubular ceramic fuel cell based on BaZr 0.1 Ce 0.7 Y 0.1 Yb 0.1 O 3-δ proton conducting electrolyte.* Journal of Power Sources, 2017. **341**: p. 264-269.

22. Ito, N., et al., *New intermediate temperature fuel cell with ultra-thin proton conductor electrolyte.* Journal of Power Sources, 2005. **152**: p. 200-203.

23. Kreuer, K., *On the development of proton conducting materials for technological applications.* Solid state ionics, 1997. **97**(1-4): p. 1-15.

24. Norby, T., *Solid-state protonic conductors: principles, properties, progress and prospects.* Solid State Ionics, 1999. **125**(1-4): p. 1-11.

25. Haile, S., G. Staneff, and K. Ryu, *Non-stoichiometry, grain boundary transport and chemical stability of proton conducting perovskites.* Journal of Materials Science, 2001. **36**(5): p. 1149-1160.

26. Wienströer, S. and H.-D. Wiemhöfer, *Investigation of the influence of zirconium substitution on the properties of neodymium-doped barium cerates.* Solid State Ionics, 1997. **101**: p. 1113-1117.

27. Bove, R. and S. Ubertini, *Modeling solid oxide fuel cell operation: Approaches, techniques and results.* Journal of Power Sources, 2006. **159**(1): p. 543-559.

28. Singhal, S.C., *Solid oxide fuel cells for power generation.* Wiley Interdisciplinary Reviews: Energy and Environment, 2014. **3**(2): p. 179-194.

29. Vincent, A.L., et al., *Preparation and characterization of an solid oxide fuel cell tubular cell for direct use with sour gas.* Journal of Power Sources, 2013. **240**: p. 411-416.

30. Rosa, R., P. Veronesi, and C. Leonelli, *A review on combustion synthesis intensification by means of microwave energy.* Chemical Engineering and Processing: Process Intensification, 2013. **71**: p. 2-18.

31. Katz, J.D., *Microwave sintering of ceramics.* Annual Review of Materials Science, 1992. **22**(1): p. 153-170.

32. Purcell, E.M. and D.J. Morin, *Electricity and magnetism*. 2013: Cambridge University Press.

33. Veronesi, P., et al., *Microwave Assisted Combustion Synthesis of Non-equilibrium Intermetallic Compounds.* Journal of Microwave Power and Electromagnetic Energy, 2010. **44**(1): p. 45-56.

34. Gupta, M. and E.W.W. Leong, *Microwaves and Metals*. 2008: John Wiley & Sons.

35. Kasap, S.O., *Principles of electronic materials and devices*. 2006: McGraw-Hill.

36. GavináWhittaker, A. and D. Michael P áMingos, *Microwave-assisted solid-state reactions involving metal powders.* Journal of the Chemical Society, Dalton Transactions, 1995(12): p. 2073-2079.

37. Council, N.R., *Microwave processing of materials*. Vol. 473. 1994: National Academies Press.

38. Rybakov, K., et al., *Microwave heating of conductive powder materials.* Journal of Applied Physics, 2006. **99**(2): p. 023506.

39. Amini, A., M. Latifi, and J. Chaouki, *Electrification of materials processing via microwave irradiation: A review of mechanism and applications.* Applied Thermal Engineering, 2021. **193**: p. 117003.

40. Mishra, R.R. and A.K. Sharma, *Microwave–material interaction phenomena: Heating mechanisms, challenges and opportunities in material processing.* Composites Part A: Applied Science and Manufacturing, 2016. **81**: p. 78-97.

41. El Khaled, D., et al., *Microwave dielectric heating: Applications on metals processing*. Renewable and Sustainable Energy Reviews, 2018. **82**: p. 2880-2892.

42. Sun, J., W. Wang, and Q. Yue, *Review on microwave-matter interaction fundamentals and efficient microwave-associated heating strategies.* Materials, 2016. **9**(4): p. 231.

43. Bhattacharyya, D. and R. Rengaswamy, *A Review of Solid Oxide Fuel Cell (SOFC) Dynamic Models.* Industrial & Engineering Chemistry Research, 2009. **48**(13): p. 6068-6086.

44. Kannan, R., et al., *Chemically stable proton conducting doped BaCeO3-no more fear to SOFC wastes.* Scientific Reports, 2013. **3**: p. 2138.

45. Singhal, S.C., *Solid oxide fuel cells for stationary, mobile, and military applications.* Solid State Ionics, 2002. **152-153**: p. 405-410.

46. Bai, Y., et al., *Anode Current Collecting Efficiency of Tubular Anode-supported Solid Oxide Fuel Cells.* Fuel Cells, 2011. **11**(3): p. 465-468.

47. Zhang, X., et al., *An anode-supported micro-tubular solid oxide fuel cell with redox stable composite cathode.* International Journal of Hydrogen Energy, 2010. **35**(16): p. 8654-8662.

48. Duan, N.-Q., et al., *High performance anode-supported tubular solid oxide fuel cells fabricated by a novel slurry-casting method.* Scientific reports, 2015. **5**: p. 8174.

49. Singh, K., A.K. Baral, and V. Thangadurai, *Ni-Ba0. 5Sr0. 5Ce0. 6Zr0. 2Gd0. 1Y0. 1O3-delta anode composites for proton conducting solid oxide fuel cells (H-SOFCs).* Journal of Materials Science Research, 2016. **5**(4): p. 34.

50. Park, K.-Y., et al., *Electrical and physical properties of composite BaZr0.85Y0.15O3−d-Nd0.1Ce0.9O2−δ electrolytes for intermediate temperature-solid oxide fuel cells.* Journal of Power Sources, 2016. **336**: p. 437-446.

51. Hanifi, A.R., et al., *Development of a novel proton conducting fuel cell based on a Ni-YSZ support.* Journal of the American Ceramic Society, 2017.

52. Bae, K., et al., *High-performance thin-film protonic ceramic fuel cells fabricated on anode supports with a non-proton-conducting ceramic matrix.* Journal of Materials Chemistry A, 2016. **4**(17): p. 6395-6403.

53. Singh, K., R. Kannan, and V. Thangadurai, *Synthesis and characterisation of ceramic proton conducting perovskite-type multi-element-doped Ba0.5Sr0.5Ce1−x−y−zZrxGdyYzO3−δ (0 < x < 0.5; y = 0, 0.1, 0.15; z = 0.1, 0.2).* International Journal of Hydrogen Energy, 2016. **41**(30): p. 13227-13237.

54. Izuki, M., et al., *Interfacial stability and cation diffusion across the LSCF/GDC interface.* Journal of Power Sources, 2011. **196**(17): p. 7232-7236.

55. Kindermann, L., et al., *Chemical compatibility of the LaFeO3 base perovskites (La0.6Sr0.4)zFe0.8M 0.2O3-δ (z = 1, 0.9; M = Cr, Mn, Co, Ni) with yttria stabilized zirconia.* Solid State Ionics, 1996. **89**(3-4): p. 215-220.

56. Dahl, P.I., et al., *Microstructural characterization and electrical properties of spray pyrolyzed conventionally sintered or hot-pressed BaZrO3 and BaZr0. 9Y0. 1O3− δ.* Solid State Ionics, 2011. **182**(1): p. 32-40.

57. Bohn, H.G. and T. Schober, *Electrical conductivity of the high-temperature proton conductor BaZr0. 9Y0. 1O2. 95.* Journal of the American Ceramic Society, 2000. **83**(4): p. 768-772.

58. Shao, Z. and S.M. Haile, *A high-performance cathode for the next generation of solid-oxide fuel cells.* Nature, 2004. **431**: p. 170.

59. Braun, A. and Q. Chen, *Experimental neutron scattering evidence for proton polaron in hydrated metal oxide proton conductors.* Nature Communications, 2017. **8**: p. 15830.

60. da Conceição, L., et al., *Combustion synthesis of La0.7Sr0.3Co0.5Fe0.5O3 (LSCF) porous materials for application as cathode in IT-SOFC.* Materials Research Bulletin, 2011. **46**(2): p. 308-314.

61. Kilner, J., *Fast oxygen transport in acceptor doped oxides.* Solid State Ionics, 2000. **129**(1): p. 13-23.

62. Minh, N.Q., *Ceramic fuel cells.* Journal of the American Ceramic Society, 1993. **76**(3): p. 563-588.

63. Zhang, J., et al., *High-temperature proton conductor Sr(Ce0.6Zr0.4)0.9Y0.1O3−δ: Preparation, sintering and electrical properties.* Ceramics International, 2008. **34**(5): p. 1273-1278.

64. Münch, W., et al., *A quantum molecular dynamics study of proton diffusion in SrTiO3 and CaTiO3.* Solid State Ionics, 1999. **125**(1): p. 39-45.

65. Laguna-Bercero, M.A., et al., *High performance of microtubular solid oxide fuel cells using Nd 2 NiO 4+ δ-based composite cathodes.* Journal of Materials Chemistry A, 2014. **2**(25): p. 9764-9770.

66. Mai, A., et al., *Time-dependent performance of mixed-conducting SOFC cathodes.* Solid State Ionics, 2006. **177**(19-25): p. 1965-1968.

67. Yokokawa, H., et al., *Fundamental mechanisms limiting solid oxide fuel cell durability.* Journal of Power Sources, 2008. **182**(2): p. 400-412.

68. Wachsman, E.D. and K.T. Lee, *Lowering the temperature of solid oxide fuel cells.* Science, 2011. **334**(6058): p. 935-939.

69. Khan, M.S., et al., *Fundamental mechanisms involved in the degradation of nickel–yttria stabilized zirconia (Ni–YSZ) anode during solid oxide fuel cells operation: A review.* Ceramics International, 2016. **42**(1, Part A): p. 35-48.

70. Singhal, S.C., *Advances in solid oxide fuel cell technology.* Solid state ionics, 2000. **135**(1-4): p. 305-313.

71. Shaikh, S.P., A. Muchtar, and M.R. Somalu, *A review on the selection of anode materials for solid-oxide fuel cells.* Renewable and Sustainable Energy Reviews, 2015. **51**: p. 1-8.

72. Jiang, S.P., *A review of wet impregnation—an alternative method for the fabrication of high performance and nano-structured electrodes of solid oxide fuel cells.* Materials Science and Engineering: A, 2006. **418**(1-2): p. 199-210.

73. Howe, K.S., et al., *Performance of microtubular SOFCs with infiltrated electrodes under thermal cycling.* International Journal of Hydrogen Energy, 2013. **38**(2): p. 1058-1067.

74. Fan, H., Y. Zhang, and M. Han, *Infiltration of La0· 6Sr0· 4FeO3-δ nanoparticles into YSZ scaffold for solid oxide fuel cell and solid oxide electrolysis cell.* Journal of Alloys and Compounds, 2017. **723**: p. 620-626.

75. Torabi, A. and T.H. Etsell, *Ni modified WC-based anode materials for direct methane solid oxide fuel cells.* Journal of The Electrochemical Society, 2012. **159**(6): p. B714-B722.

76. Hallopeau, L., et al., *Microwave-assisted reactive sintering and lithium ion conductivity of Li1. 3Al0. 3Ti1. 7 (PO4) 3 solid electrolyte.* Journal of Power Sources, 2018. **378**: p. 48-52.

77. Subasri, R., et al., *Microwave processing of sodium beta alumina.* Solid State Ionics, 2003. **158**(1-2): p. 199-204.

78. Pillai, R.C., et al., *Solid-state synthesis of calcium carbide by using 2.45 GHz microwave reactor.* Industrial & Engineering Chemistry Research, 2015. **54**(44): p. 11001-11010.

79. Oghbaei, M. and O. Mirzaee, *Microwave versus conventional sintering: a review of fundamentals, advantages and applications.* Journal of Alloys and Compounds, 2010. **494**(1-2): p. 175-189.

80. Mohebbi, H., T. Ebadzadeh, and F. Hesari, *Synthesis of nano-crystalline (Ni/NiO)–YSZ by microwave-assisted combustion synthesis method: the*

influence of pH of precursor solution. Journal of Power Sources, 2008. **178**(1): p. 64-68.

81. Mahato, N., et al., *Progress in material selection for solid oxide fuel cell technology: A review.* Progress in Materials Science, 2015. **72**: p. 141-337.

82. Luo, Y. and Q. Wang, *Zein-based micro-and nano-particles for drug and nutrient delivery: A review.* Journal of Applied Polymer Science, 2014. **131**(16).

83. Ortiz-Vitoriano, N., et al., *Optimization of La0. 6Ca0. 4Fe0. 8Ni0. 2O3–Ce0. 8Sm0. 2O2 composite cathodes for intermediate-temperature solid oxide fuel cells.* Journal of Power Sources, 2011. **196**(9): p. 4332-4336.

84. Howe, K., et al., *Performance of microtubular SOFCs with infiltrated electrodes under thermal cycling.* international journal of hydrogen energy, 2013. **38**(2): p. 1058-1067.

85. Amiri, T., et al., *High performance tubular solid oxide fuel cell based on $Ba_{0.5}Sr_{0.5}Ce_{0.6}Zr_{0.2}Gd_{0.1}Y_{0.1}O_{3-\delta}$ proton conducting electrolyte.* Journal of The Electrochemical Society, 2018. **165**(10): p. F764-F769.

86. Sandhu, N.K., et al., *Electrochemical performance of a short tubular solid oxide fuel cell stack at intermediate temperatures.* Applied energy, 2016. **183**: p. 358-368.

87. Ding, D., et al., *Enhancing SOFC cathode performance by surface modification through infiltration.* Energy & Environmental Science, 2014. **7**(2): p. 552-575.

88. Wan, T.H., et al., *Influence of the discretization methods on the distribution of relaxation times deconvolution: implementing radial basis functions with DRTtools.* Electrochimica Acta, 2015. **184**: p. 483-499.

89. West, A.R., et al., *Novel high capacitance materials:- BaTiO3:La and CaCu3Ti4O12.* Journal of the European Ceramic Society, 2004. **24**(6): p. 1439-1448.

90. Ortiz-Vitoriano, N., et al., *Synthesis and electrochemical performance of La0. 6Ca0. 4Fe1− xNixO3 (x= 0.1, 0.2, 0.3) material for solid oxide fuel cell cathode.* Journal of Power Sources, 2009. **192**(1): p. 63-69.

91. Mahajan, S., et al., *Study of Structural and Electrical Properties of Conventional Furnace and Microwave-Sintered BaZr0. 10Ti0. 90O3 Ceramics.* Journal of the American Ceramic Society, 2009. **92**(2): p. 416-423.

92. Leonide, A., et al., *Impedance study of alternative (La, Sr) FeO3− δ and (La, Sr)(Co, Fe) O3− δ MIEC cathode compositions.* Journal of The Electrochemical Society, 2010. **157**(2): p. B234-B239.

93. Leonide, A., et al., *Evaluation and modeling of the cell resistance in anode-supported solid oxide fuel cells.* Journal of The Electrochemical Society, 2008. **155**(1): p. B36-B41.

94. Schichlein, H., et al., *Deconvolution of electrochemical impedance spectra for the identification of electrode reaction mechanisms in solid oxide fuel cells.* Journal of Applied Electrochemistry, 2002. **32**(8): p. 875-882.

95. Yin, Y., et al., *Visualizing Gas Diffusion Behaviors in Three-Dimensional Nanoporous Media.* Energy & Fuels, 2021. **35**(3): p. 2075-2086.

96. Madi, H., et al., *Solid oxide fuel cell anode degradation by the effect of hydrogen chloride in stack and single cell environments.* Journal of Power Sources, 2016. **326**: p. 349-356.

97. Fleig, J., *Solid oxide fuel cell cathodes: Polarization mechanisms and modeling of the electrochemical performance.* Annual Review of Materials Research, 2003. **33**(1): p. 361-382.

98. Nuernberg, R. and M. Morelli, *Synthesis of BSCF perovskites using a microwave-assisted combustion method.* Ceramics International, 2016. **42**(3): p. 4204-4211.

99. Weifan, C., et al., *One-step synthesis of nanocrytalline perovskite LaMnO3 powders via microwave-induced solution combustion route.* Journal of Rare Earths, 2006. **24**(6): p. 782-787.

100. Gangurde, L.S., et al., *Synthesis, characterization, and application of ruthenium-doped SrTiO3 perovskite catalysts for microwave-assisted methane dry reforming.* Chemical Engineering and Processing-Process Intensification, 2018. **127**: p. 178-190.

101. Ortiz-Vitoriano, N., et al., *Electrochemical characterization of La0. 6Ca0. 4Fe0. 8Ni0. 2O3− δ perovskite cathode for IT-SOFC.* Journal of Power Sources, 2013. **239**: p. 196-200.

102. Shah, M., P.W. Voorhees, and S.A. Barnett, *Time-dependent performance changes in LSCF-infiltrated SOFC cathodes: The role of nano-particle coarsening.* Solid State Ionics, 2011. **187**(1): p. 64-67.

103. Chick, L.A., et al., *Glycine-nitrate combustion synthesis of oxide ceramic powders.* Materials letters, 1990. **10**(1-2): p. 6-12.

104. Vincent, A.L., et al., *Porous YSZ impregnated with La0. 4Sr0. 5Ba0. 1TiO3 as a possible composite anode for SOFCs fueled with sour feeds.* Journal of Power Sources, 2012. **215**: p. 301-306.

105. Park, Y.M., et al., *Effect of anode thickness on impedance response of anode-supported solid oxide fuel cells.* International Journal of Hydrogen Energy, 2012. **37**(5): p. 4394-4400.

106. Wu, J., et al., *In-situ synthesis of a cordierite-andalusite composite for solar thermal storage.* Solar Energy Materials and Solar Cells, 2013. **108**: p. 9-16.

107. Suzuki, T., et al., *Impact of anode microstructure on solid oxide fuel cells.* Science, 2009. **325**(5942): p. 852-855.

108. Endo, A., et al., *Low overvoltage mechanism of high ionic conducting cathode for solid oxide fuel cell.* Journal of the Electrochemical Society, 1998. **145**(3): p. L35-L37.

109. Huang, Z., M. Gotoh, and Y. Hirose, *Improving sinterability of ceramics using hybrid microwave heating.* Journal of Materials Processing Technology, 2009. **209**(5): p. 2446-2452.

110. Karayannis, V.G. *Microwave sintering of ceramic materials*. in *IOP Conference Series: Materials Science and Engineering*. 2016. IOP Publishing.

111. Colomban, P. and J. Badot, *Frequency dependent conductivity and microwave relaxations in protonic conductors.* Solid state ionics, 1993. **61**(1-3): p. 55-62.

112. Leonelli, C., et al., *Microwave assisted sintering of green metal parts.* Journal of Materials Processing Technology, 2008. **205**(1-3): p. 489-496.

113. Manivannan, S., et al., *Effect of microwave and conventional sintering on densification, microstructure and dielectric properties of BZT–xCr2O3 ceramics.* Ceramics International, 2015. **41**(9): p. 10923-10933.

114. Berteaud, A. and J. Badot, *High temperature microwave heating in refractory materials.* Journal of Microwave Power, 1976. **11**(4): p. 315-2320.

115. Wang, B., L. Bi, and X.S. Zhao, *Fabrication of one-step co-fired proton-conducting solid oxide fuel cells with the assistance of microwave sintering.* Journal of the European Ceramic Society, 2018. **38**(16): p. 5620-5624.

116. Jiao, Z., N. Shikazono, and N. Kasagi, *Comparison of ultra-fast microwave sintering and conventional thermal sintering in manufacturing of anode support solid oxide fuel cell.* Journal of Power Sources, 2010. **195**(24): p. 8019-8027.

117. Molero-Sánchez, B., E. Morán, and V. Birss, *Rapid and Low-Energy Fabrication of Symmetrical Solid Oxide Cells by Microwave Methods.* ACS Omega, 2017. **2**(7): p. 3716-3723.

118. Agrawal, D., *Microwave sintering of ceramics, composites and metallic materials, and melting of glasses.* Transactions of the Indian Ceramic Society, 2006. **65**(3): p. 129-144.

119. Blake, R.D. and T.T. Meek, *Microwave processed composite materials.* Journal of materials science letters, 1986. **5**(11): p. 1097-1098.

120. Roy, R., et al., *Full sintering of powdered-metal bodies in a microwave field.* Nature, 1999. **399**(6737): p. 668-670.

121. Zhong, G., et al., *Synthesis of metal oxide nanoparticles by rapid, high-temperature 3D microwave heating.* Advanced Functional Materials, 2019. **29**(48): p. 1904282.

122. Janney, M.A., C.L. Calhoun, and H.D. Kimrey, *Microwave sintering of Solid oxide fuel cell materials: I, zirconia-8 mol% yttria.* Journal of the American Ceramic Society, 1992. **75**(2): p. 341-346.

123. Singh, S., et al., *Microwave processing of materials and applications in manufacturing industries: a review.* Materials and Manufacturing Processes, 2015. **30**(1): p. 1-29.

124. Haugsrud, R., *On the high-temperature oxidation of nickel.* Corrosion Science, 2003. **45**(1): p. 211-235.

125. Matsuda, M., K. Nakamoto, and M. Miyake, *Temperature profile and sinterability of self-heating porous NiO-(Ce, Sm) O2 composite during microwave irradiation.* Journal of the Ceramic Society of Japan, 2006. **114**(1325): p. 106-109.

126. Goldstein, A., et al., *Direct microwave sintering of yttria-stabilized zirconia at 2· 45 GHz.* Journal of the European Ceramic Society, 1999. **19**(12): p. 2067-2072.

127. Campana, R., et al., *Fabrication, electrochemical characterization and thermal cycling of anode supported microtubular solid oxide fuel cells.* Journal of Power Sources, 2009. **192**(1): p. 120-125.

128. Li, Y.C., et al., *In situ investigation on the mixed-interaction mechanisms in the metal–ceramic system's microwave sintering.* Acta Materialia, 2014. **66**: p. 293-301.

129. Demirskyi, D., D. Agrawal, and A. Ragulya, *Neck growth kinetics during microwave sintering of nickel powder.* Journal of Alloys and Compounds, 2011. **509**(5): p. 1790-1795.

130. Amiri, T., T.H. Etsell, and P. Sarkar, *Using Microwave Irradiation for In-situ Infiltration of Electrodes in Solid Oxide Fuel Cells.* Materials Technology, 2022: p. 1-10.

131. Takeda, O., T. Ouchi, and T.H. Okabe, *Recent progress in titanium extraction and recycling.* Metallurgical and Materials Transactions B, 2020. **51**(4): p. 1315-1328.

132. Suput, M., et al., *Solid oxide membrane technology for environmentally sound production of titanium.* Mineral Processing and Extractive Metallurgy, 2008. **117**(2): p. 118-122.

133. Pal, U.B. and A.C. Powell, *The use of solid-oxide-membrane technology for electrometallurgy.* Jom, 2007. **59**(5): p. 44-49.

134. Prokudina, V.K., *Titanium Nitride*, in *Concise Encyclopedia of Self-Propagating High-Temperature Synthesis*, I.P. Borovinskaya, et al., Editors. 2017, Elsevier: Amsterdam. p. 398-401.

135. Kuwahara, H., et al., *Mechanical properties of bulk sintered titanium nitride ceramics.* Materials Science and Engineering: A, 2001. **319-321**: p. 687-691.

136. Akinribide, O.J., et al., *Sintering of binderless TiN and TiCN-based cermet for toughness applications: Processing techniques and mechanical properties: A review.* Ceramics International, 2019. **45**(17, Part A): p. 21077-21090.

137. Delbari, S.A., et al., *Spark plasma sintering of TiN ceramics codoped with SiC and CNT.* Ceramics International, 2019. **45**(3): p. 3207-3216.

138. Zarabi Golkhatmi, S., M.I. Asghar, and P.D. Lund, *A review on solid oxide fuel cell durability: Latest progress, mechanisms, and study tools.* Renewable and Sustainable Energy Reviews, 2022. **161**: p. 112339.

139. McIntosh, S. and R.J. Gorte, *Direct hydrocarbon solid oxide fuel cells.* Chemical reviews, 2004. **104**(10): p. 4845-4866.

140. Zhang, J., et al., *Development of the applications of titanium nitride in fuel cells.* Materials Today Chemistry, 2019. **11**: p. 42-59.

141. Tan, K., H. Rahman, and H. Taib, *Coating layer and influence of transition metal for ferritic stainless steel interconnector solid oxide fuel cell: A review.* International Journal of Hydrogen Energy, 2019. **44**(58): p. 30591-30605.

142. Ananthapadmanabhan, P., et al., *Destabilization of calcia stabilized zirconia.* Journal of materials science, 1989. **24**(12): p. 4432-4436.

143. Pappacena, A., L. Bardini, and M. Boaro, *Catalysts and processes in solid oxide fuel cells*, in *Advances in Medium and High Temperature Solid Oxide Fuel Cell Technology*. 2017, Springer. p. 155-221.

144. Qiao, J., et al., *Ni/YSZ and Ni–CeO2/YSZ anodes prepared by impregnation for solid oxide fuel cells.* Journal of Power Sources, 2007. **169**(2): p. 253-258.

145. Connor, P.A., et al., *Tailoring SOFC electrode microstructures for improved performance.* Advanced Energy Materials, 2018. **8**(23): p. 1800120.

146. Jo, S., et al., *Materials and nano-structural processes for use in solid oxide fuel cells: A review.* Journal of the Korean Ceramic Society, 2020. **57**(2): p. 135-151.

147. Lu, C., et al., *LSM-YSZ cathodes with reaction-infiltrated nanoparticles.* Journal of the Electrochemical Society, 2006. **153**(6): p. A1115.

148. Hanifi, A.R., et al., *Development of redox resistant fully infiltrated tubular SOFCs.* Journal of The Electrochemical Society, 2014. **161**(4): p. F391-F397.

149. Kalinina, E. and E. Pikalova, *Opportunities, challenges and prospects for electrodeposition of thin-film functional layers in solid oxide fuel cell technology.* Materials, 2021. **14**(19): p. 5584.

150. Jung, S., et al., *Electrodeposition of Cu into a highly porous Ni∕YSZ cermet.* Journal of the Electrochemical Society, 2006. **153**(8): p. A1539.

151. Ojo, A.A. and I.M. Dharmadasa, *Electroplating of semiconductor materials for applications in large area electronics: A review.* Coatings, 2018. **8**(8): p. 262.

152. Jamil, Z., et al., *Anode fabrication for solid oxide fuel cells: Electroless and electrodeposition of nickel and silver into doped ceria scaffolds.* international journal of hydrogen energy, 2016. **41**(22): p. 9627-9637.

153. Zhang, L., et al., *Analysis of electroplating baths by capillary electrophoresis with high voltage contactless conductivity detection.* Measurement Science and Technology, 2006. **17**(12): p. 3317.

154. Hunter, R.J., *Zeta potential in colloid science: principles and applications*. Vol. 2. 2013: Academic press.

155. Kosmulski, M., *A literature survey of the differences between the reported isoelectric points and their discussion.* Colloids and Surfaces A: Physicochemical and Engineering Aspects, 2003. **222**(1-3): p. 113-118.

156. Ardizzone, S. and C. Bianchi, *Electrochemical features of zirconia polymorphs. The interplay between structure and surface OH species.* Journal of Electroanalytical Chemistry, 1999. **465**(2): p. 136-141.

157. Rose, M.F., et al., *Limiting factors for carbon-based chemical double-layer capacitors.* Journal of Power Sources, 1994. **47**(3): p. 303-312.

158. Kang, Y., C. Yang, and X. Huang, *Dynamic aspects of electroosmotic flow in a cylindrical microcapillary.* International Journal of Engineering Science, 2002. **40**(20): p. 2203-2221.

159. Gaikwad, H.S., D.N. Basu, and P.K. Mondal, *Slip driven micro-pumping of binary system with a layer of non-conducting fluid under electrical double layer*

phenomenon. Colloids and Surfaces A: Physicochemical and Engineering Aspects, 2017. **518**: p. 166-172.

160. Sarkar, P. and P.S. Nicholson, *Electrophoretic deposition (EPD): mechanisms, kinetics, and application to ceramics.* Journal of the American Ceramic Society, 1996. **79**(8): p. 1987-2002.

161. Amiri, S., R.E. Hayes, and P. Sarkar, *Transient simulation of a tubular micro-solid oxide fuel cell.* Journal of Power Sources, 2018. **407**: p. 63-69.

162. Matsuda, M., et al., *Fabrication of bilayered YSZ/SDC electrolyte film by electrophoretic deposition for reduced-temperature operating anode-supported SOFC.* Journal of Power Sources, 2007. **165**(1): p. 102-107.

163. Kobayashi, K., et al., *Supported Zr (Sc) O2 SOFCs for reduced temperature prepared by electrophoretic deposition.* Solid State Ionics, 2002. **152**: p. 591-596.

164. Bahramian, A., et al., *Single-step electrodeposition of superhydrophobic black NiO thin films.* Journal of Applied Electrochemistry, 2019. **49**(6): p. 621-629.

165. Hanifi, A.R., et al., *Development of redox resistant fully infiltrated tubular SOFCs.* Journal of The Electrochemical Society, 2014. **161**(4): p. F391.

166. Jongprateep, O., V. Petrovsky, and F. Dogan, *Yttria Stabilized Zirconia as a Candidate for High Energy Density Capacitor.* Agriculture and Natural Resources, 2008. **42**(5): p. 373-377.

167. Srinivasan, V. and J.W. Weidner, *An electrochemical route for making porous nickel oxide electrochemical capacitors.* Journal of the Electrochemical Society, 1997. **144**(8): p. L210.

168. Li, P.-W. and K. Suzuki, *Numerical modeling and performance study of a tubular SOFC.* Journal of the Electrochemical Society, 2004. **151**(4): p. A548.

169. Hotza, D., D.E. García, and R.H. Castro, *Obtaining highly dense YSZ nanoceramics by pressureless, unassisted sintering.* International Materials Reviews, 2015. **60**(7): p. 353-375.

170. Simwonis, D., F. Tietz, and D. Stöver, *Nickel coarsening in annealed Ni/8YSZ anode substrates for solid oxide fuel cells.* Solid State Ionics, 2000. **132**(3-4): p. 241-251.